UNIVERSITY OF NAPLES FEDERICO II

Doctoral School of Earth Sciences

Doctoral thesis in Structural and Applied Geology
(XXVIII)

3D structural characterization of outcrops by means of close-range multi-view stereo-photogrammetry

Supervisor

Dr. Stefano Tavani

Ph.D. Student

Amerigo Corradetti

Ph.D. Coordinator

Prof. Maria Boni

Academic Year 2015/2016

Table of Contents

ABSTRACT

Image-based 3D modelling is increasingly used as a fast and cheap alternative to laser-scanning for the 3D digital representation of geological outcrops. This rapidly improving technique is progressively opening the way to the widespread use of virtual outcrop models in geology, as the technique allows nearly everybody to construct a detailed digital model of geological exposures simply using a few handy and cheap devices.

In this dissertation, the photogrammetry method has been used to demonstrate and evaluate the potential of virtual outcrops in structural geology. In particular, through the analysis of different outcrops at different scales, I showed that virtual outcrop models enable a switch from a mere descriptive/qualitative analysis of the outcrops to a quantitative one. In fact, by mean of virtual reality it is possible to overcome almost all technical limitations that are generally encountered during field work at different scales including prospective distortion, inaccessibility and the lack of instruments for quantitative acquisition of data, among others.

1. INTRODUCTION

Geological bodies (e.g. sedimentary strata, deformation structures, etc.) present three-dimensional complex geometries and architectures resulting by the combination of the depositional/formational stacking patterns with the deformation history. Understanding their actual three-dimensional geometry (e.g. shape and distribution) has a considerable economic and social significance in terms of geofluids provision (e.g. hydrocarbon and drinkable water), ore deposits and civil engineering, among many others.

It is for this reason that, during relatively recent years, industries first, and at a later stage the academic community, have adopted as standard the construction of 3D geological models. Those models are obtained from primarily subsurface seismic datasets or outcrops.

Offshore seismic data, such as seismic profiles or 3Dimensional cubes, provide two dimensional or complete three-dimensional clues to enable identification of geological elements, and in particular km-scale geometries that are impossible to observe from wells or outcrops. However, seismic methods suffer from non-unique interpretations that need semi-quantitative validation, such as large-scale outcropping analogues. This is obvious considering the amount of heterogeneities in any geological setting and the finite resolution of the method, which is typically from several meters to tens of meters; it is essentially at this scale that the fluid-flow behaviour within rock masses (e.g. reservoirs) is controlled (Vaughan et al., 2004).

In areas where geological and geophysical data are typically sparse due to the complexity of the structures and accessibility problems, such as in onshore fold-and-thrust provinces, the construction of three-dimensional models is even more intricate (e.g. Fernández et al., 2004, 2009).

On the other hand, outcrops, which represent surface analogues of the buried geological systems, are able to provide primary information about meters to decametres-scale heterogeneities that are not resolvable through indirect methods. By solving these scales, it is possible to gather important clues, for example, to populate reservoir models bridging the resolution gap between seismic and well data within petroleum systems. Conventional outcrop studies, however, has long lacked fully reconstructed outcrop models, which could be realistically and quantitatively compared to their subsurface analogues (Verwer, 2008). This issue mainly results from the difficulty of capturing both the two-dimensional and the three-dimensional geometry of geological bodies and surfaces in a consistent and accurate way.

With the advent of the digital age, however, the development of digital field acquisition methods (e.g. real time kinematic global positioning systems, RTK GPS, and light detection and ranging, LiDAR), have made possible the actualization of fully three-dimensional spatial analysis (e.g. McCaffrey et al., 2005). At their early stages, those methods were not very versatile, expensive and inaccurate as were software applications available to process and analyse these digital datasets.

During recent years, however, techniques aimed at the acquisition of three-dimensional information of outcrops, have experienced a fast development with their widespread applicability to various scientific fields, including architecture, cultural heritage, archeology, topography, forensic sciences, and geology among others. In particular, three-dimensional representations in geology are known as virtual outcrop models (VOMs) (Xu et al., 1999, 2000; Pringle et al., 2001; Bellian et al., 2005; Clegg et al., 2005; McCaffrey et al., 2005; Trinks et al., 2005; Buckley et al., 2008, 2010; Jones et al., 2008), but are also referred as digital (Bellian et al., 2005; García-Sellés et

al., 2011) or photorealistic outcrop models (Xu et al., 2000; Buckley et al., 2008; Minisini et al., 2014).

1.1 VIRTUAL OUTCROP MODELS

A VOM is essentially defined as a digital 3D representation of the outcrop topography. This is generally represented in the form of a XYZ point cloud, which is a set of coordinate points, in an arbitrary or georeferenced coordinate system. The information is commonly stored as a plain text file (ASCII file) that can also enclose the RGB (Red Green Blue) information of each point (i.e. coloured point cloud). When an enough dense cloud of an outcrop is available, the user at the computer screen is able to already distinguish many geological features (e.g. bed-forms, fractures, and faults), and several kinds of measurements may be obtained. In several cases, the quality of the dataset can be improved by meshing the point cloud. Through this process, the point cloud is converted to a three-dimensional triangulated or gridded surface, made of irregular polygons (generally triangles), that is commonly referred as a mesh. When the photographic information is available (such as with photogrammetry or a laser scanner with an integrated camera) the mesh may also be textured (i.e. an image is draped onto the mesh). More in detail, during the texturing of the mesh, two coordinates (U and V) are assigned to each vertex of each triangle of the mesh. At the same time, a texture map is generated; this is basically a two-dimensional (U and V) image consisting of a puzzle of triangular images that will be applied to the mesh. The visual experience with a well-textured mesh of an outcrop can be very close to reality.

VOMs can be substantially generated by two competitive surveying methods: LiDAR and digital stereo-photogrammetry (here simply referred as photogrammetry). The first is by far the most accomplished method employed in the production of virtual outcrops. In particular, it has certainly been the most acknowledged method within the geological community (Hodgetts, 2013), albeit limited to a certain elite of people due to budget limitations.

Among many companies that are actually producing scanners, the best known are Leica, Riegle, Trimble and Optec. Although different kinds and models of scanner exist, the basic principle is that a light pulse (preferably green, since an infra-red wavelength would be affected by absorption of the water eventually present on the outcrop surface) is emitted from the laser head and the time, from emission to return of the reflected beam, measured. Of course, knowing light velocity (and some correction factors), the distance of each point hit by the light beam is computed. The entire outcrop is scanned this way by rotating the laser head at constant angular velocity.

Photogrammetry is instead an estimative technique whereby metric data for an object (i.e. the shape, position and size) is obtained through the analysis of two or more images of the same scene taken from different points of view (Figure 1). In particular, metric data for the objects are obtained by estimating the spatial coordinates of each point in the photos. Since only two-dimensional coordinates can be obtained from a single image, two or more photos are needed to estimate the three-dimensional coordinates of points.

The algorithms involved in the automated reconstruction of 3D models from 2D unconstrained photographs are termed Structure from Motion (SfM; Ullman 1979). These algorithms have seen a dramatic development over the last two decades, in particular, recent advances have been made with respect to the image matching techniques (e.g. Gruen 2012), which are methods developed with the aim of establishing the relationship between images, and hence to study how a feature observed in one image may be recognized in other images taken in different conditions (e.g. different point of view, focal distance, lighting condition, etc.). The turning point has probably occurred when the detection of features among multi-view imageries has become possible, for example with the Scale Invariant Feature Transform algorithm

(SIFT; Lowe 2004), which transforms image data into scale-invariant coordinates relative to local features.

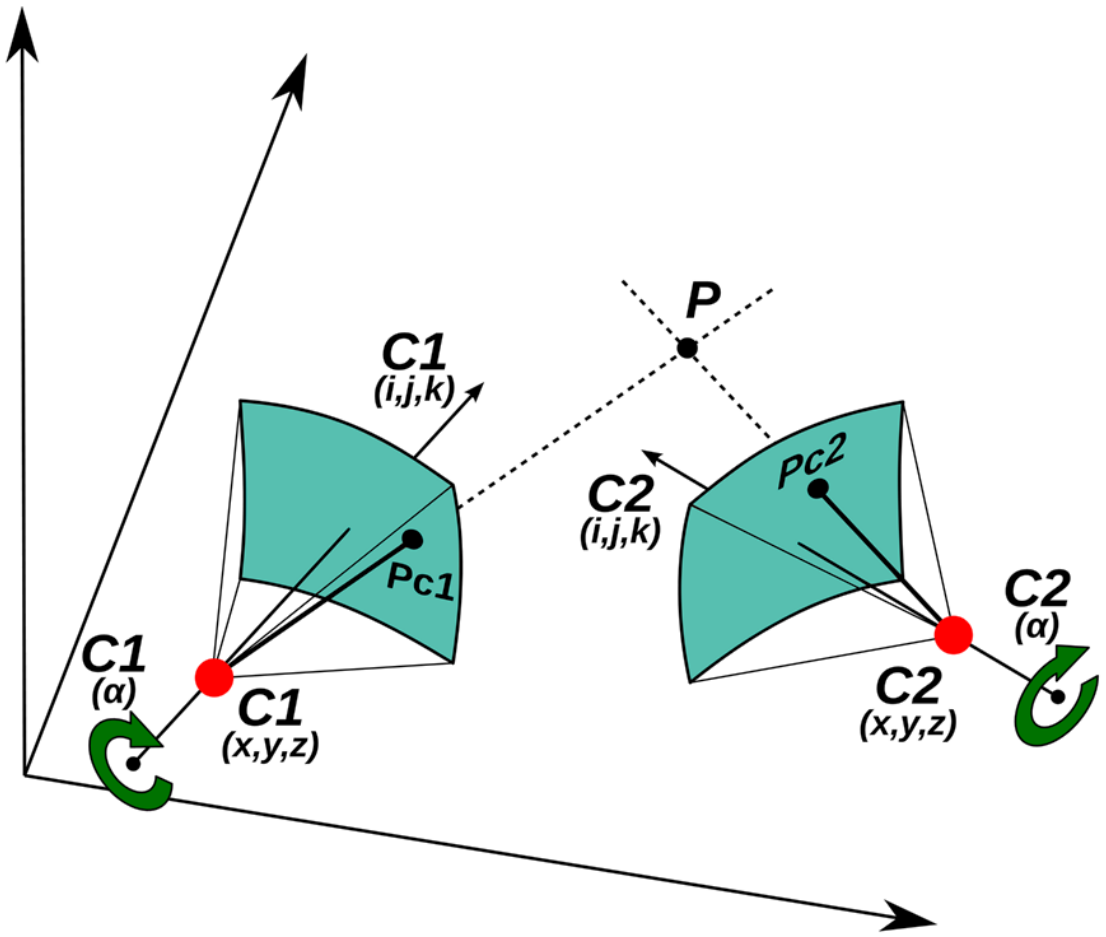

Figure 1. This scheme shows the parameters involved in stereoscopic view. When a point P is photographed from two cameras C1 and C2, the position of P in the two photos (Pc1 and Pc2) depends on the position of the two cameras, on their focal length, and on their orientation, which is defined by 4 parameters (the ijk versor and the angle α defining the amount of rotation about the ijk axis). From Tavani, Granado, et al., 2014

More particularly, SfM algorithms, given a set of partly overlapping photographs pointing at the same scene, detect suites of points or point clusters in the different photographs. The knowledge of these point coordinates in the different photographs makes possible the computation of the parameters that relate the XYZ position of a point in the space to its X_nY_n position in the n^{th} photograph (i.e. set by camera position, orientation, and focal length), and the subsequent transformation of pixels seen in different photographs into points

placed in an arbitrarily 3D space (Figure 1). In essence, this process leads to the construction of a sparse point cloud.

A denser point cloud is then generally built through pair-wise depth map computation (i.e. an image that contains information relating to the distance of the surfaces of scene objects from a viewpoint) or Multi-View Stereo (MVS) matching methods (i.e. specific algorithms designed to operate ultra-high resolution images by decomposition of the initial images to efficiently compute dense 3D point clouds).

To date, SfM algorithms are implemented in many freeware and commercial software (Snavely et al., 2008). Commercial software has several advantages including the availability of all in one solution designed in a user friendly manner. Among these, PhotoModeler and PhotoScan are certainly leading the academic market. Totally free solutions are instead available combining SfM-MVS algorithms (James and Robson, 2012) such as Bundler (SfM) and PMVS2 (Furukawa and Ponce, 2010) or CSVM (Furukawa et al., 2010) (MVS), among other solutions (Bemis et al., 2014).

Also thanks to recent hardware and software developments, photogrammetry has experienced a so rapid growth that it is now possible to produce VOMs through the use of any digital cameras (including camera phone and compact cameras).

1.2 LiDAR vs Photogrammetry

Numerous controversial papers exist in favour of the accuracy of the two methods, nevertheless, while accuracy and error of a certain model of laser scanner are clearly stated in the vendor specifications (albeit with minor case by case variability), the same properties cannot be determined in advance for the photogrammetry case. It is therefore not possible to determine a priori which method will be, at the end, more accurate. Before studying a specific outcrop or geological structure, the choice of the method should, hence, be based on different considerations, keeping in mind that LiDAR certainly has a better constrained workflow that is less subjected to case by case variability.

LiDAR, however, has a variety of disadvantages that goes beyond the mere, nevertheless important, economic factor. For instance, even if recent models of laser scanners are now much lighter than in the past, they still remain quite bulky and heavy devices, so that remote areas are still challenges (Hodgetts, 2013). On the other hand, the most evident advantage of photogrammetry is, in fact, its versatility in the most disparate conditions; it has dramatically faster acquisition time and much lower apparatus weight (i.e. the weight of a digital camera), so that even remote areas are easily accessible. LiDAR, instead, has the advantage of a minor or a completely unnecessary post-acquisition processing.

Despite these most obvious advantages for each technology and without considering topics like accuracy and precision of the differently derived point clouds (this is anyway a fundamental issue that has to be considered case by case), there is a less intuitive, although simple, crucial consideration. Although both technologies are able to generate an accurate georeferenced point cloud that can be later triangulated in order to generate a polygonal mesh, the process

of texturing (i.e. applying an image to the mesh), which is easy and straightforward with photogrammetry (James and Robson, 2012; Tavani et al., 2014), is often complex in LiDAR datasets from multiple scan positions (Hodgetts, 2013). This is an obvious consequence of the nature of the two methodologies, one that begins from the same information that has to be textured (i.e. a photoset), and one that has to consider hybrid solution to solve the problem of texturing (i.e. LiDAR plus photos).

2. METHODS

For all those reasons discussed in the previous chapter, and in particular the versatility of the photogrammetric method together with the ease with which point clouds can be meshed and textured, I used this method to build the 3D models for the case studies presented. In particular, the models were built using the commercial software Agisoft PhotoScan; this software has been chosen among many alternatives because of its user-friendly nature and the availability of an academic license.

Different cameras and set-up were used for the different case studies presented. These will be discussed in their relative sub-chapters, while here, only general methods are presented.

2.1 GENERAL ADVICE ON PHOTO CAPTURE

In this paragraph I will not enter into the merits of how photographs have been taken during fieldworks, since this topic will be discussed later for each case study. Nevertheless, general rules exist in order to obtain good quality VOMs. These rules are thought to optimize SfM algorithms. In essence, photos should be taken from multiple points of view and with a substantial overlap. It is worthwhile to use the same camera to minimize errors coming from the use of different lenses and camera sensors, while keeping the focal length fixed is not compulsory but it is strongly recommended (Tavani et al., 2014). Furthermore, in the case of not diffuse light (e.g. sunny days), it is recommended to take photos consecutively to avoid the coupling of shadows of different shapes within different images (e.g. Arbués et al., 2012).

Photographs should not be taken too obliquely to facilitate features matching between images, but this is a debatable argument since oblique photos would, at the same time, enhance the model accuracy (Moreels and Perona, 2006; Bemis et al., 2014; James and Robson, 2014). Nevertheless any attempt to quantify an optimal angle between images and the outcrop should be case by case dependent and rely on specific SfM algorithms. A fast rule is that it is always convenient to take many more photographs than necessary, and, eventually, delete some of them later from the PC.

2.2 BUILDING A VOM WITH PHOTOSCAN

After all selected photographs of an outcrop are imported into PhotoScan (Verhoeven, 2011), a photo-mask (Figure 2a) can be applied to each photo in order to exclude "problematic" areas from further analysis and matching. These areas are, for example, unwanted or unnecessary features like vegetation or the sky and in particular images in the background (e.g. clouds, birds, trees, etc.), that in addition to being time-consuming may produce errors or overload the model with non-interesting scenes. Even though photo-masking can be very time consuming for the users, it can improve later computations.

After those areas are masked, the first subsequent mandatory step is photo-alignment. This command attempts to recognize every point in common between each overlapping photograph, allowing to compute position and orientation of each photo and, in turn, the creation of a sparse point-cloud representing the surfaces of the objects within the target scene (e. g. Gruen et al., 2004; Verhoeven, 2011; Favalli et al., 2012).

This is a time-consuming and iterative process which can be improved by manually indicating matching points among photographs (Figure 2c). Wrong alignments, which can be recognized by the presence of unrealistic geometries within the point cloud (Figure 2b), are generally solved by indicating further matching points or, eventually, removing those photos that cannot be aligned. Photos with large overlap are generally aligned without problems regardless of the camera parameters.

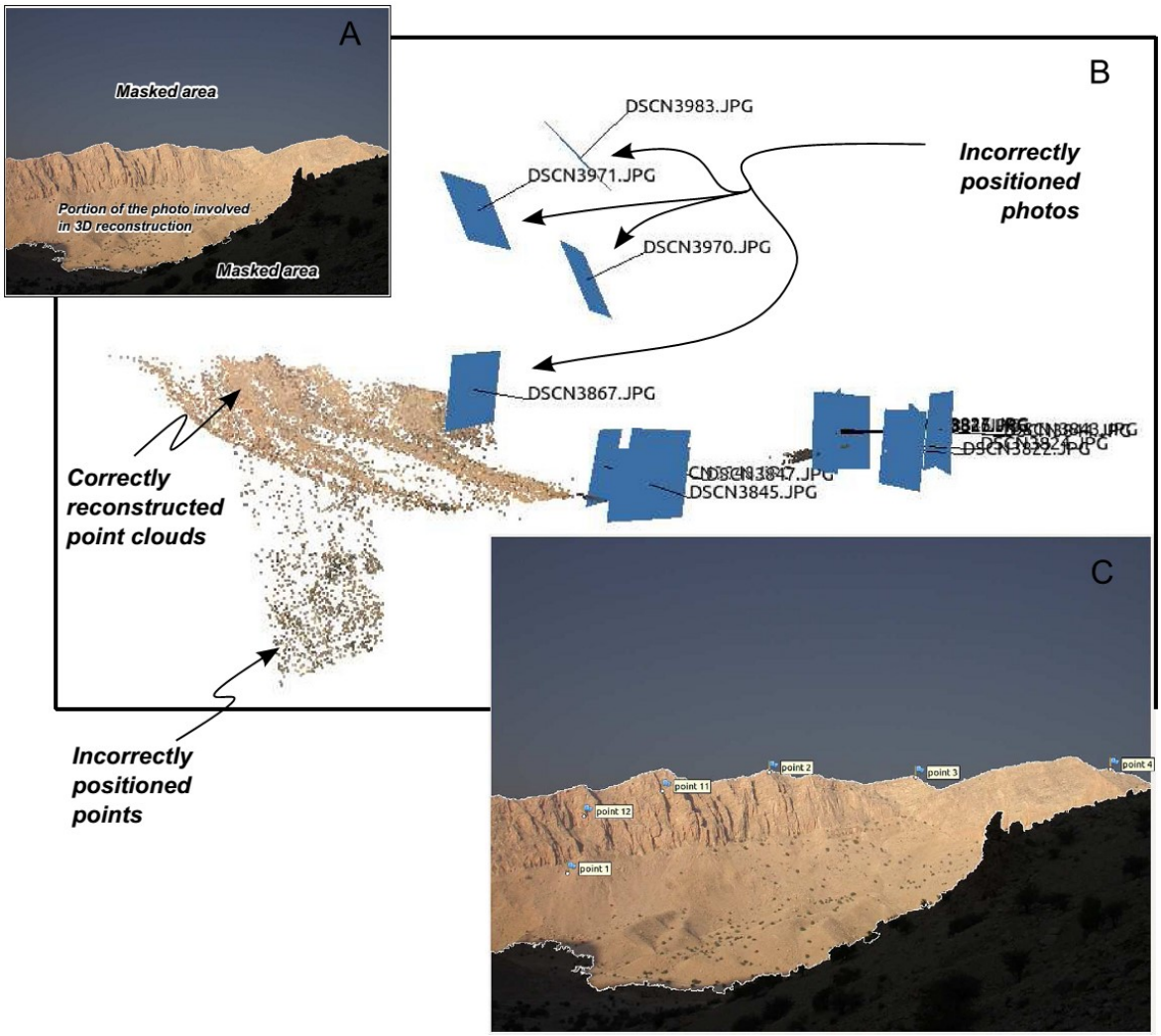

Figure 2. Steps involved in the photo-alignment. (A) Masking of photos allows one to remove unwanted areas from the reconstructed model. (B) Photo-alignment of unoriented photos providing as output both the reconstructed point-cloud and the position of photos. At this stage, large errors can be easily recognized, being evidenced by unrealistic photo-positioning (in the example, some photos are located more than 500 m above the ground) and by the presence of incorrectly positioned points. (C) Providing the position of known objects (markers) in the different photos can greatly help the alignment of photos. From Tavani, Granado, et al., 2014.

Once photos are aligned and the sparse point cloud generated (Figure 3a), depth maps (i.e. estimated distance of each pixel from the camera position) are reconstructed for each photograph by interpolating data from the recognized points. Depth maps allow the software to run a second round of point-detection, which eventually results in the creation of a second and denser point-cloud (Figure 3b).

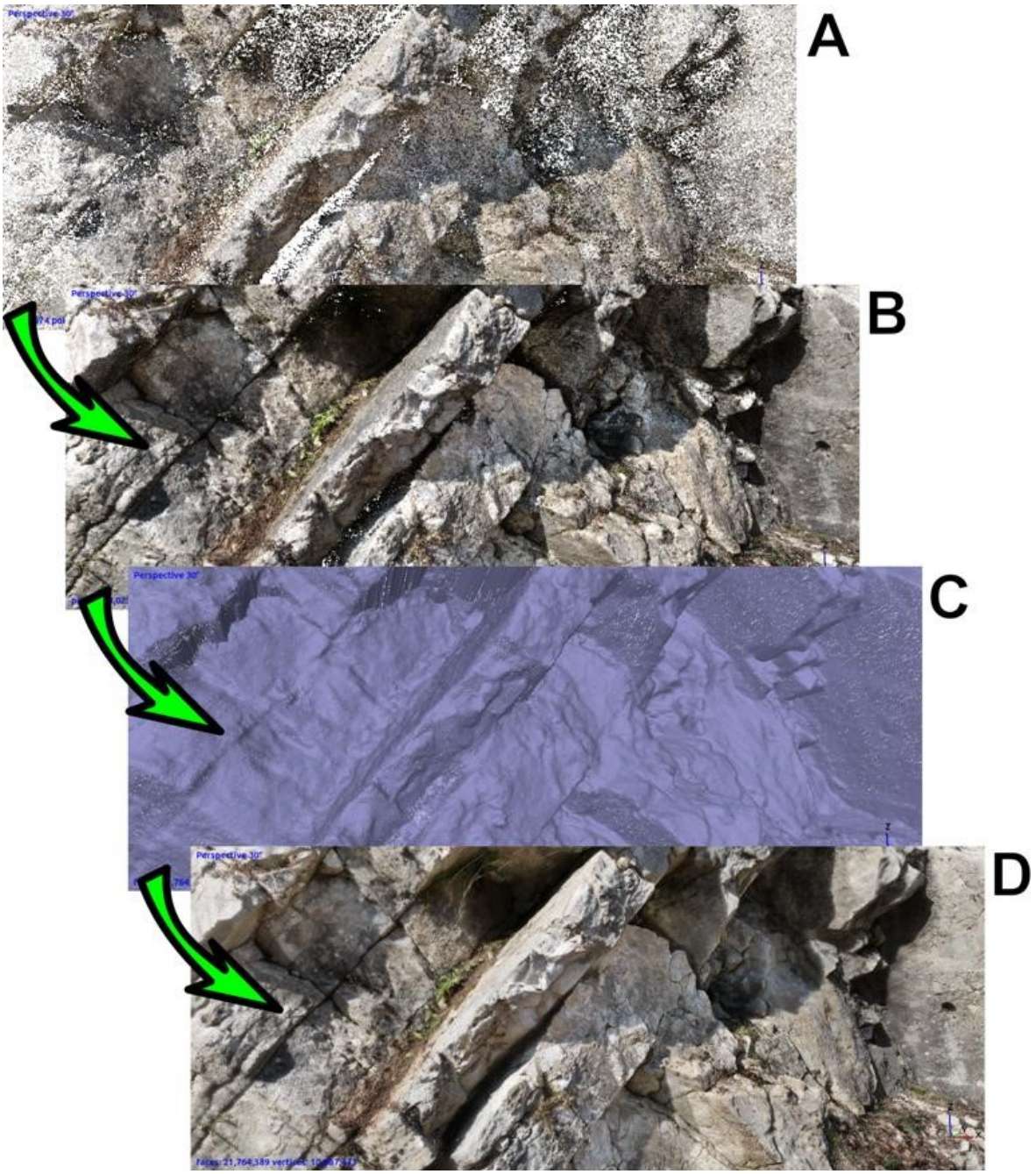

Figure 3. Steps involved in the VOM reconstruction via PhotoScan. (A) Colored (RGB) point-cloud is reconstructed after photo-alignment. (B) Dense point-cloud, after depth maps reconstruction. (C) Triangular mesh derived from the dense point cloud, seen in wireframe mode, is built through the "built texture" command. (D) Textured mesh. Refer to text for further details. These examples are taken from the Frontone VOM.

The succeeding step (i.e. "building geometry") triangulates the point-cloud and returns a mesh made of irregular triangles (Figure 3c). In reality, the term triangulation is here improperly used to indicate that the point cloud is discretized by a gridded surface made of irregular triangles where each triangle

can be imagined as a best-fit plane of a local point cluster, and not by a real triangulation (e.g. Delaunay triangulation). Then, through the "building texture" command, a texture map can be rapidly generated and draped onto the triangular mesh (Figure 3d). In detail, two coordinates (U and V) are assigned to each vertex of each triangle of the mesh, representing a point in the texture map. The U and V coordinates of vertexes enable a triangle in the texture map to be cropped, and then paste onto the corresponding triangle of the mesh (Figure 4). The higher the number of triangles in the mesh is, the higher the resolution of the texture map should be.

The last step in the realization of the model is the re-orientation and rescaling of the 3D model and, eventually, its georeferencing to a known coordinate system. This can be achieved when the real position of at least 3 points within the model is known.

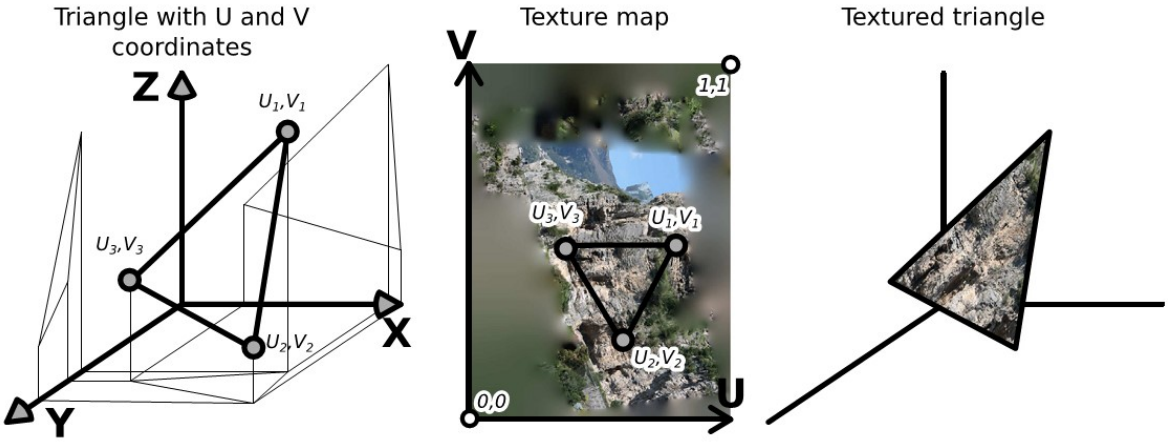

Figure 4. Procedure for texturing of a triangular mesh. From Tavani, Granado, et al., 2014.

2.3 MODEL MANAGING AND DATA EXTRACTION WITH OPENPLOT

The models where later imported into the OpenPlot free software (Tavani et al., 2011, 2014), where I extracted a series of geological data directly from the textured meshes, including, for instance, bedding, fractures, and faults attitudes. Although it was not used in all of the case studies, the use of the OpenPlot software has been fundamental to most of the analysis. The main tools of the software are hence described in this sub-chapter.

OpenPlot is a multiplatform (Linux, Mac OS and Windows) and open source software for geostructural data analysis. The software has a 3D environment which allows visualizing and manipulating both point clouds and textured meshes. For technical information the reader can refer to Tavani, Granado, et al., (2014) or go to http://www.openplot.altervista.org/ for updated material and tutorial.

In order to be imported into OpenPlot, the textured mesh has to be exported from PhotoScan as a wavefront file and the "export texture" option must be enabled during exporting. The wavefront OBJ format includes three files: (i) an *.obj file which contains the geometric information of the mesh, (ii) a *.mtl file with material definition (not used by OpenPlot), and (iii) a *.jpg (or *.png) file which represents the texture map. When dealing with large projects it is also possible to separate the model into parts and export them separately, to ease the rendering speed into the next steps.

Within the 3D environment of OpenPlot, one of the drawing tools is "draw-polyline" (Figure 5). This tool allows the user to digitize a polyline by clicking point-by-point along the intersection between a geological target surface (such as bedding, fractures, faults, etc.) and the outcrop topography

(Hodgetts et al., 2004; Trinks et al., 2005). A best fit plane of this polyline is then computed and stored (see Tavani, Granado, et al., 2014) together with its strike and dip. The success of the computation of each plane is strictly related to the quality and three-dimensionality of the mesh since a plane is best calculated from co-planar but non-collinear points (Fernández et al., 2009). The created planar polygons are georeferenced structural objects, hence, they can be filtered, analysed, plotted and so on. Polylines can be digitized over either point clouds or meshes, but the use of a mesh strongly increases the chance of catch a geological surface that may be hidden between points if the resolution of the point cloud is not large enough.

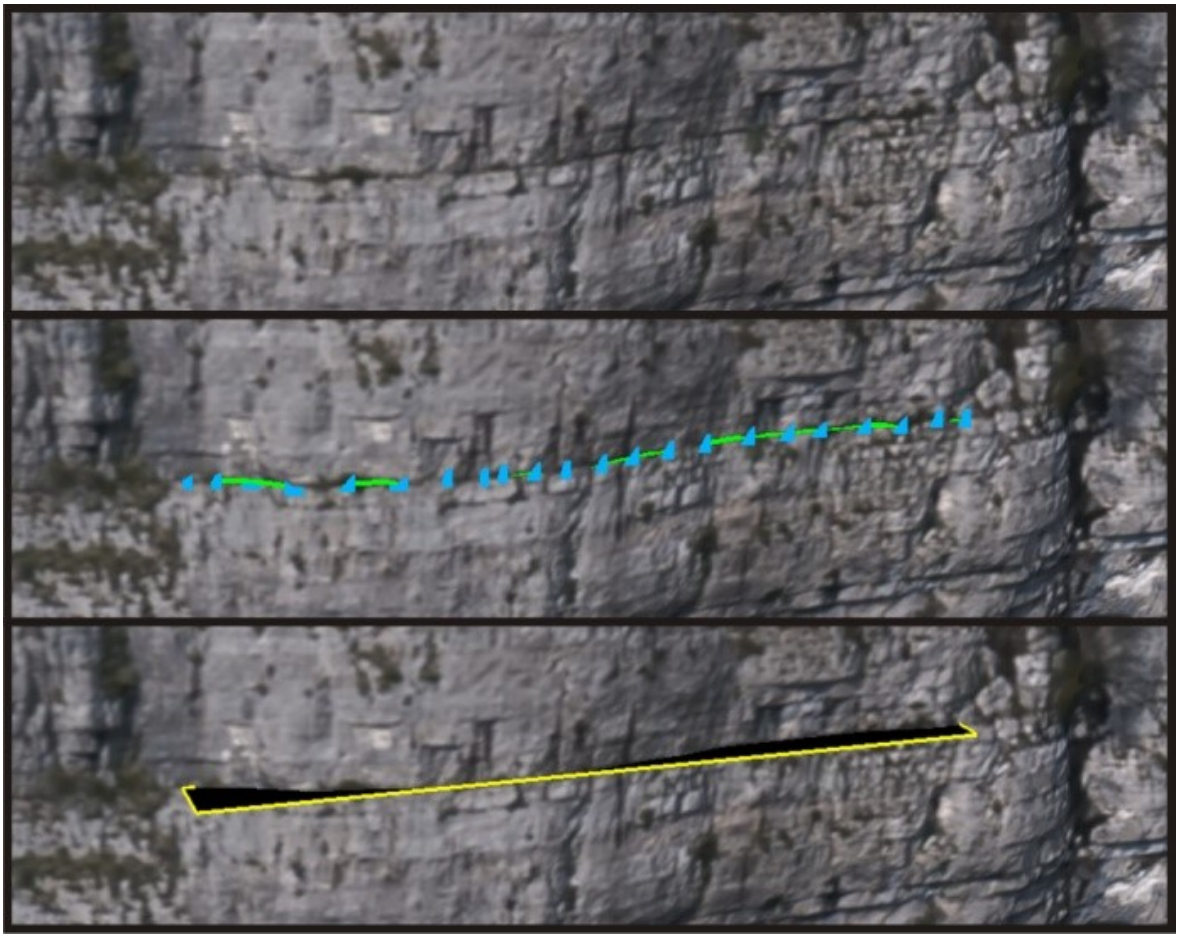

Figure 5. Point-by-point digitization of a geological surface. In this case an almost horizontal bed belonging to the Conocchia cliff outcrop.

A complementary procedure aimed at measuring virtual geological surface attitudes also exists. This can be applied when surfaces of interest, or at least part of them, are exposed (Figure 6a). In this case, the triangular polygons composing the mesh are in fact parallel to the surface of interest. In OpenPlot it is possible to plot the orientation of selected triangles from the 3D environment to a contour plot (Figure 6b), where the occurrence of clusters in the triangles orientation are recognized. Directly from the contour plot, a colour can be assign to these clusters (i.e. each triangle in the cluster is coloured with the assigned colour (Figure 6c), thus enhancing the recognition of areas that include parallel triangles (Figure 6d). From Figure 6c and Figure 6d it is evident that one of the clusters, corresponding to triangles dipping toward the north that have been here coloured in green, is related to vegetation and can then be disregard from geological consideration. The cluster coloured in yellow, dipping at high angle toward E-NE, is parallel to bedding. Eventually, from the 3D environment of OpenPlot, the user can select cluster of triangles belonging to bedding (Figure 6e), where the triangle vertexes are used to extract a best-fit plane (Figure 6f). The quality of the extracted best-fit plane can be evaluated by comparing the average triangle orientation and the orientation of the best-fit plane (Figure 6g).

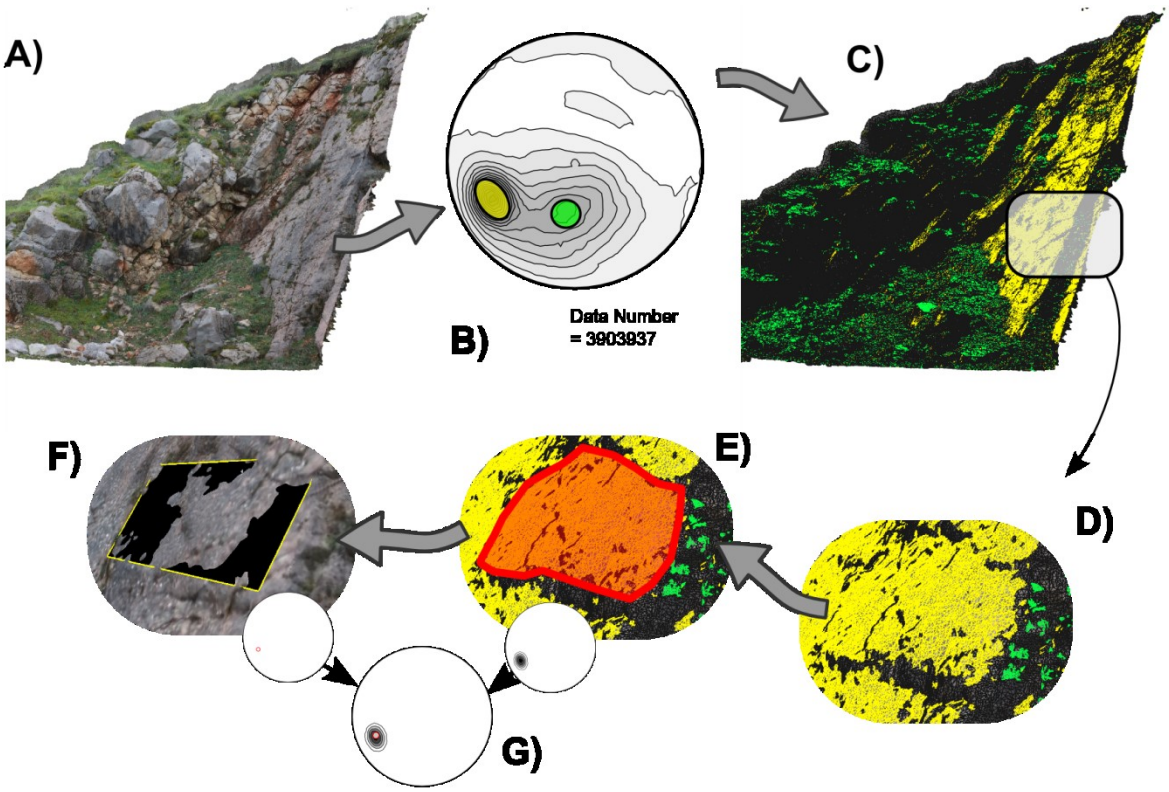

Figure 6. Data extraction through orientation analysis of the mesh. Given an area of interest (A), the orientation of triangles of this area is plotted (B). In the stereoplot, a color filter can be applied. (C) The 3D mesh is then re-loaded in color mode, so that the user can detect areas where triangles orientation is rather constant and parallel to the orientations of interest. (D) At this stage, smaller areas are selected and, in order to individuate near-planar features, sub-areas with near-parallel triangles are selected. (E) Vertexes of triangles within the selected area are used to extract a best fit plane (F). (G) Comparison between the average orientation of triangles of the selected area and the orientation of the best-fit plane allows the user to evaluate the quality of the fit. This example is taken from the Rocca di Cave VOM.

3. CASE STUDIES

For convenience of presentation, case studies have been grouped into four sections, which, on a first approximation, reflect the scale of the outcrops. This distinction was necessary because the scale, in turn, involves different approaches and methods, and eventually, different goals.

The first section discusses about partly-accessible outcrops at the meso-scale and, in particular, it illustrates the workflow for producing properly oriented sections of the VOMs by presenting three different examples. In addition, an innovative and low-cost approach to scale and re-orient a model, and to evaluate, on first approximation, the error generated within the model is presented in this section. This intuitive workflow gives its best benefits for all those outcrops where the use of highly precise and expensive instruments is not repaid in terms of accuracy needs.

Within the second section, the photogrammetric method is used to acquire very detailed profiles (which it is not synonymous with accuracy) of rough surfaces such as faults. The method accuracy is hence investigated in two ways: (1) making 3D models of rough objects of known size, and (2) testing self-affinity of fault surfaces following already described procedures (e.g. Candela et al., 2009, 2012; Bistacchi et al., 2011; Renard et al., 2013) that these authors applied to 3D or 2D data produced by means of laser scanners, laser profilometers and eventually by white light interferometers. A Matlab© code has been here developed and it is presented into the Appendices.

Within the third section, the workflow followed during the structural study of an inaccessible, reservoir scale, analogue within the Sorrento Peninsula (Italy), is presented. The outcrop, chosen for his potential as analogue, is inaccessible to standard studies due to its position and size.

Photographic acquisition of this outcrop required the use of an unmanned aerial veichol (UAV), here referred as drone, equipped with a digital camera.

The last session describes how old photos of outcrops, initially made without taking into account their 3D development, can be used to produce 3D models. This task may prove useful in several applications in structural geology, such as teaching, revaluation and arrangement of new and old projects, and sharing of results.

3.1 SCALING, RE-ORIENTATION AND ORTHORECTIFICATION OF MESO-SCALE OUTCROPS

To this category belong outcrops of several meters up to few tens of meters that are generally, at least partly, accessible. Among the several applications that an image-based VOM holds for geological research (e.g. extended area coverage, large number of measurements, and as a teaching tool), perhaps one of the most interesting and, at the same time, basic needs is to be able to look at a virtual outcrop in orthographic view mode from any geologically-relevant point of view (e.g. fold axis, fault slip-normal, fracture-bedding intersection). This application allows the user to virtually orthorectify the outcrop (Figure 7), so that true measurements of geological features can be done directly on the computer monitor.

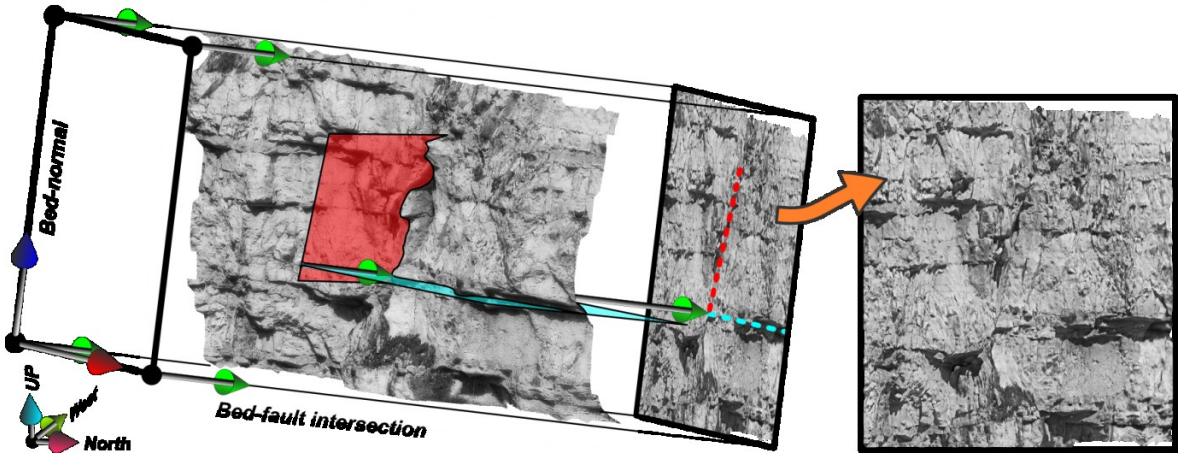

Figure 7. Orthorectification of a Virtual Outcrop Model (VOM) in PhotoScan. The orthorectification essentially consists in the projection of the model onto a plane oriented perpendicularly to a direction of interest, for instance, the bedding-fault intersection direction in the shown example. This example is taken from the San Severino VOM.

In this sub-chapter, I show geologically relevant application of this basic application to VOMs. In particular, the workflow for producing "orthorectified" virtual outcrops is here illustrated using three different examples from the central-northern Apennines (Italy). The orthorectification of these outcrops has the aim of studying, without geologically-significant

distortion and through geologically-representing points of view: (1) the displacement of strata along an incipient normal fault in the San Severino locality; (2) the wedge geometry of tilted carbonate strata in the Rocca di Cave locality; (3) the deformation processes involved in the formation of a kink fold in the Frontone locality.

Regardless of the resolution of a VOM, errors and distortions in the obtained models cannot be determined without knowing the position of points included in the outcrop. Accurate positioning of points can be obtained, for example, by means of a total station, which is an expensive and, above all, heavy device. Nevertheless, extremely accurate positioning of points may be unnecessary for a number of applications in structural geology.

In this work, I have addressed the error issue by using some portable and cheap tools that focus on the internal relative scales and positions of objects: a compact laser distance meter, a compass, a laser level mounted on a tripod with a graduated rotary table, and some coded targets (Figure 8a).

In the field (Figure 8b), the compass served to orient the rotary table, which represents the origin of a local reference system, towards the north. The laser level is then used to position a first suite of coded targets (hereafter named “coordinate targets”) at a constant elevation (that of the level). The position of these targets with respect to the origin (i.e. the laser level) is annotated as angular coordinates obtained by the graduated rotary and as distances obtained by the laser distance meter. Additional targets (hereafter named “random targets”) are randomly distributed on the outcrop surface and only their distance from the origin is measured.

The outcrop is then extensively photographed from different positions providing a good overlap between each successive image. It is also important to acquire a set of photographs of the outcrop along with the laser level, since the latter will serve as origin for a local coordinate system.

After importing all photographs into PhotoScan, the targets are manually identified in each photo. This identification process has the fringe benefit of greatly improve the correct positioning of photographs. The VOM is then generated in PhotoScan through the photo alignment, densification of the point cloud, building of the geometry and building of the texture processes.

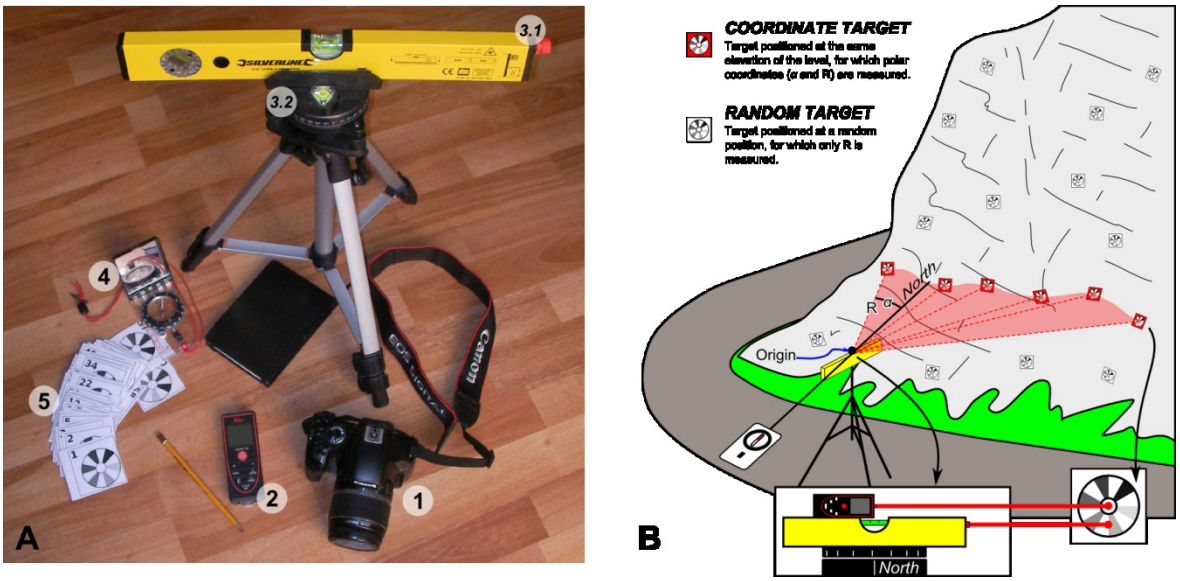

Figure 8. (A) Field devices used in this work: (1) Canon EOS 450D camera. Photograph resolution is set to 4272X2848 pixel. (2) Leica DISTO D2 distance meter (0.05 to 60 m measuring range, accuracy = ± 1.5 mm). (3) Silverline equipment including (3.1) a 40 cm long level (error on the horizontal determination is ± 0.29 °) with a laser pointer and (3.2) a tripod with a graduated rotary table. (4) Silva compass. (5) Coded targets. (B) Scheme showing the field use of compass, distance menter, laser level, and rotary table, to place a first suite of targets in the outcrop and to get their polar coordinates (coordinate targets: red targets in the figure). Additional targets (random targets: white targets in the figure) are arbitrarily placed and only their distance from the origin is measured.

In the 3D digital model, the positions of the coordinate targets are used to scale and re-orient the model in PhotoScan. This operation is achieved by simple trigonometry by assigning a XYZ value to each coordinate target where

the level is at the origin (0 0 0) (Figure 9). For instance, the XYZ coordinates are calculated as illustrated in Figure 9.

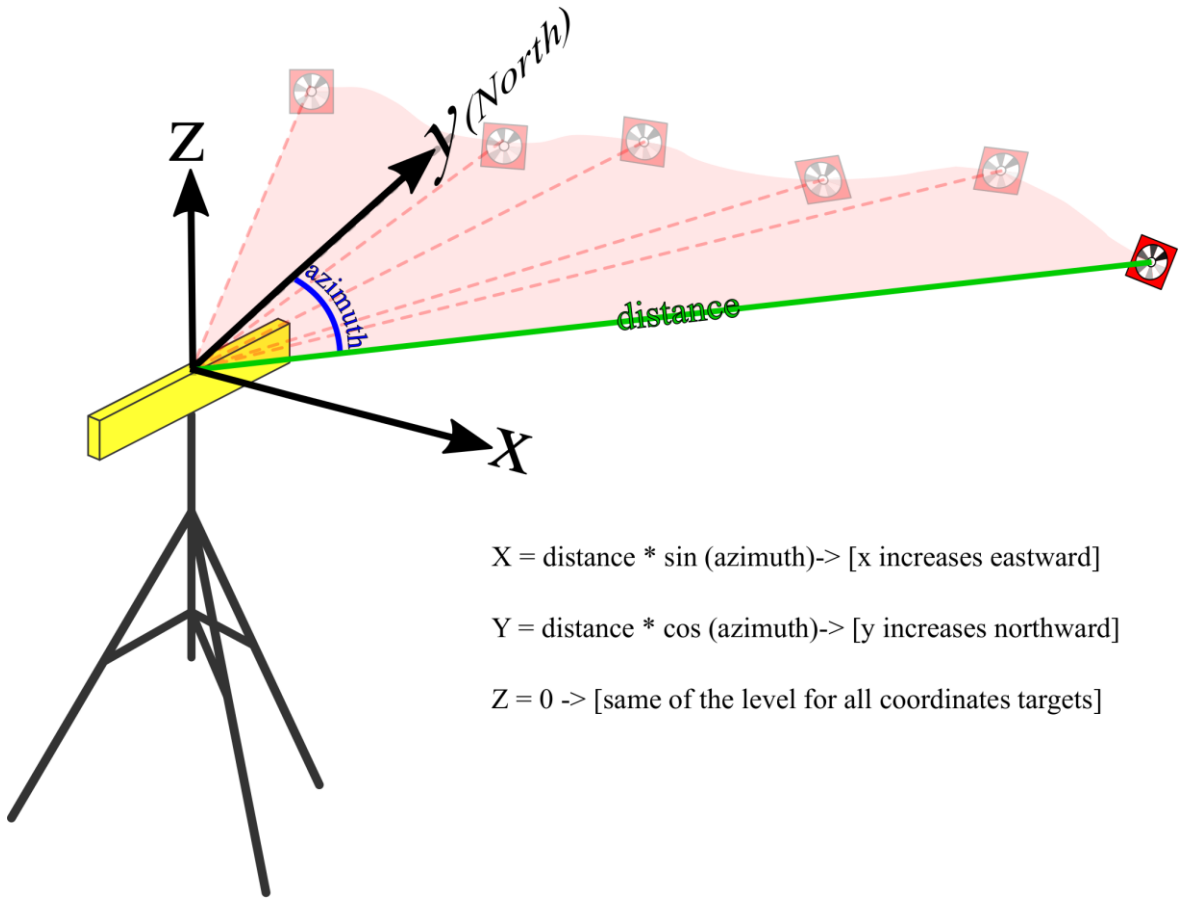

Figure 9. This scheme shows the orientation of the coordinate system that result from the proposed trigonometric calculations. See text for details.

The positions of all targets in the scaled 3D digital model are then computed, to compare the distances between the targets and the origin as measured in the real world and in the digital environment. This easy procedure allowed estimating discrepancies (i.e. errors) between measurements in reality and the corresponding points in the digital model.

The subsequent step is the extraction of the geological data, such as bedding and fracture attitudes. This procedure is done on the textured mesh after importing it into OpenPlot. As shown later, through different analyses of

the resulting attitudes, it is possible to calculate the direction of interest to orthorectify the 3D model.

Once the direction for orthorectification is known, the XYZ positions of the coordinate targets are re-calculated in a rotated reference system with the Y axis oriented as the direction of interest.

In particular, the new coordinates can be easily calculated through elementary transformation matrices. For instance, given a direction of projection of 300/20 (azimuth/dip), two rigid rotations around the origin are necessary (Figure 10): one is around the Z axis amounting to the azimuth angle and the subsequent is around the rotated X (i.e. X') amounting to the dip angle.

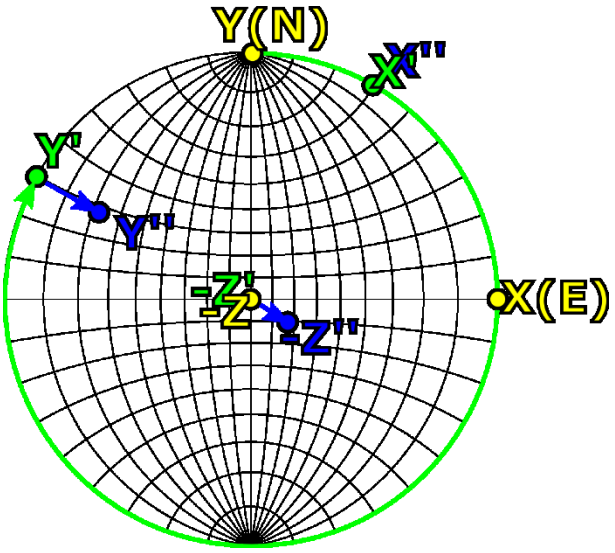

Figure 10. Equal area stereo-net showing the coordinate system (in yellow) obtained from the rotary level and the laser distance meter. In order to re-orient the Y axis toward the computed point of view two rotations must be made. A first rotation, amounting to the azimuth angle, is carried out around the Z axis, while a second rotation, amounting to the dip angle, is carried out around the X' axis. Z axes are negative because they are elevations depicted in the lower hemisphere.

The resulting elementary transformation matrixes are given by:

$$R_z(azimuth[\alpha]) = \begin{bmatrix} \cos(\alpha) & -\sin(\alpha) & 0 \\ \sin(\alpha) & \cos(\alpha) & 0 \\ 0 & 0 & 1 \end{bmatrix}$$

to rotate of an angle α around the Z axis, and by:

$$R_x(dip[\delta]) = \begin{bmatrix} 1 & 0 & 0 \\ 0 & \cos(\delta) & -\sin(\delta) \\ 0 & \sin(\delta) & \cos(\delta) \end{bmatrix}$$

to rotate of an angle δ around the X axis.

Therefore, the XYZ positions of the coordinate targets in the new coordinate system are given by:

$$\begin{bmatrix} x'' \\ y'' \\ z'' \end{bmatrix} = R_x(\delta)R_z(\alpha)\begin{bmatrix} x \\ y \\ z \end{bmatrix} = \begin{bmatrix} \cos(\alpha) & -\sin(\alpha) & 0 \\ \sin(\alpha)\cos(\delta) & \cos(\alpha)\cos(\delta) & -\sin(\delta) \\ \sin(\alpha)\sin(\delta) & \cos(\alpha)\sin(\delta) & \cos(\delta) \end{bmatrix}\begin{bmatrix} x \\ y \\ z \end{bmatrix}$$

In linear algebra, this rotation is equivalent to a change of base (i.e. the transition from a fixed reference system to a rotated one).

When these new coordinates are updated into PhotoScan, the VOM is automatically rotated to the new point of view and can be then exported in orthographic mode.

3.1.1 The Rocca di Cave outcrop

The Rocca di Cave outcrop is an E-W-oriented, 20 m wide, and 4 m high exposure located near Rome within the Miocene-Pleistocene Apennine fold-thrust belt at the following coordinates: latitude 41°50'48"N and longitude 12°57'2"E. The geological framework of the area is detailed in Tavani et al. (2015). A NNW-SSE-striking near vertical normal fault affects the rocks consisting of sub-horizontal Cretaceous and steeply dipping to near vertical Miocene carbonate strata in the fault footwall and hanging wall, respectively (Figure 11).

Figure 11. Photograph of the Rocca di Cave study outcrop showing a steeply dipping normal fault characterized by Cretaceous limestones in the footwall and Miocene calcarenites in the hanging wall. Coded targets on the outcrop are indicated with triangles. Yellow-filled triangles, in particular, indicate target placed at the same elevation of the laser level.

The laser level was positioned at about 10 m from the outcrop and, following the previously-illustrated procedure, the level was used to place seven coordinate targets (at the same elevation of the laser level) along with ten random target placed at various elevations (Figure 11).

110 photographs (12.1Mpixel each) were taken at distances of about 2 and 4 meters from the outcrop (Figure 12). As seen in Figure 12, photographs were taken almost perpendicularly to the photographed portion of the outcrop. The photographed areas range between 5x3.3 m and 2x1.3 m (width times height), so that the resolution of photographs (i.e. pixels/photographed area) ranges between about 2 to 0.7 pixel/mm^2. Different elevations and distances from the outcrop during photograph acquisition ensured that each portion of the outcrop is seen in at least four photographs.

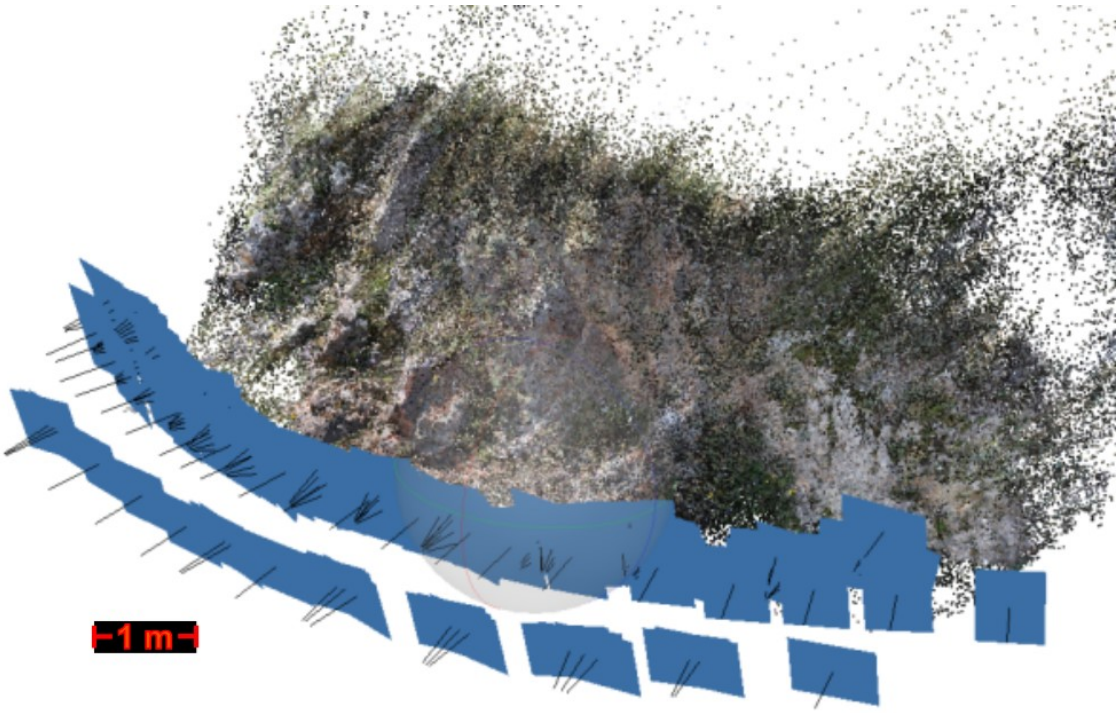

Figure 12. RGB coloured point cloud of the Rocca di Cave outcrop with spatial distribution of photographs used to build the cloud, as seen in Agisoft PhotoScan.

Ten more photographs were acquired displaying both the study outcrop and the laser level in its working position. These latter photographs are mandatory to include also the origin of the system (i.e. the laser level) in the 3D model. As the laser level was placed about 10 m away from the outcrop, these latter photographs are oblique to the outcrop and have different

resolutions for the laser level (about 1 pixel/mm^2) and for the outcrop (less than 0.4 pixel/cm^2).

In PhotoScan, a first point-cloud (Figure 13a) consisting of about $5x10^4$ points for the area of the laser level and $1.2x10^6$ points for the outcrop surface was generated. The surface of the outcrop is about 300 m^2, hence the density of this first point cloud was 0.4 points/cm^2. A second and denser point-cloud of $24x10^6$ points (only for the outcrop) was built from the depth maps (resolution of about 8 points/cm^2; Figure 13b). Next, from this dense point cloud a triangular mesh made of $30x10^6$ irregular triangles with an average area of 0.1 cm^2 (Figure 13c) was built. As the mesh vertexes hold photographic RGB colour attributes, displaying the mesh in solid-coloured mode allows one to recognise real objects and features much better than in the point cloud (Figure 13d). The rendering performance of the mesh can be further improved by texturing. Texture maps resolution has, however, serious hardware limitations. Generally, the size of the texture map is limited to 4096x4096 or 8192x8192 pixels; these high values frequently implying the pixellation of the mesh, i.e. individual pixels are recognisable (Figure 13e). Such a problem can be solved by dividing the mesh into smaller sub-meshes and applying different texture maps to each sub-mesh (Figure 13f). It is highly recommended to scale and re-orient the mesh, using the coordinate targets, before it is split, so that the sub-meshes are scaled and re-oriented too.

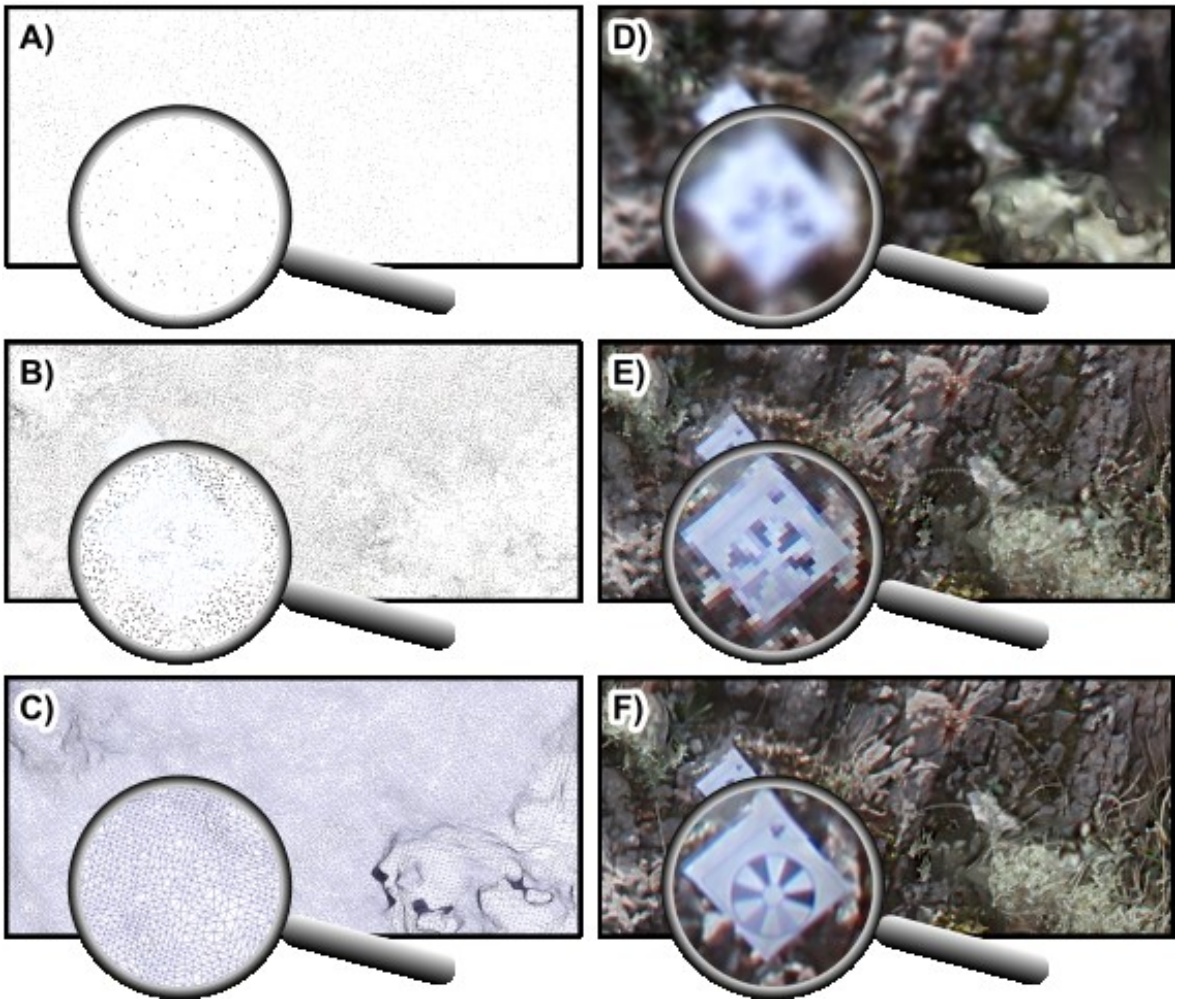

Figure 13. Different versions of the Rocca di Cave Virtual Outcrop Model, with detail showing a coded target. (A) Coloured (RGB) point-cloud. (B) Dense point-cloud built after depth maps reconstruction. (C) Triangular mesh derived from the dense point cloud, seen in wireframe mode. (D) Triangular mesh seen in coloured mode. Photographic colour (RGB) information exists for the three triangle vertexes, and colour inside the triangle is derived from this information. (E) Textured mesh, where an image (i.e. the texture) is draped onto the mesh (so that the rendering within triangles is improved). (F) Increasing the resolution of the texture increase the quality of rendering.

The distance between all targets and the origin (Rv) in the digital model was computed after scaling and re-orientation, and compared with that measured in the field (Rf). In the case of the Rocca di Cave outcrop, differences between Rf and Rv are less than 4 cm (Figure 14a) with an average value of 2 cm. These differences are insensitive to the X, Y, and Z coordinates (Figure 14b). This result points out the absence of a remarkable distortion along the three axes. Differences are higher than 2 cm only for those coded targets that we could not fully adhere to the outcrop surface. As a consequence,

the software averaged the decoupled target and outcrop surfaces as it did not recognise the small empty space between the outcrop surface and the target (Figure 15), thus producing an higher Rf vs. Rv mismatch. It is therefore recommended to fully adhere the targets to the outcrop surface to avoid miscalculated Rf vs. Rv values.

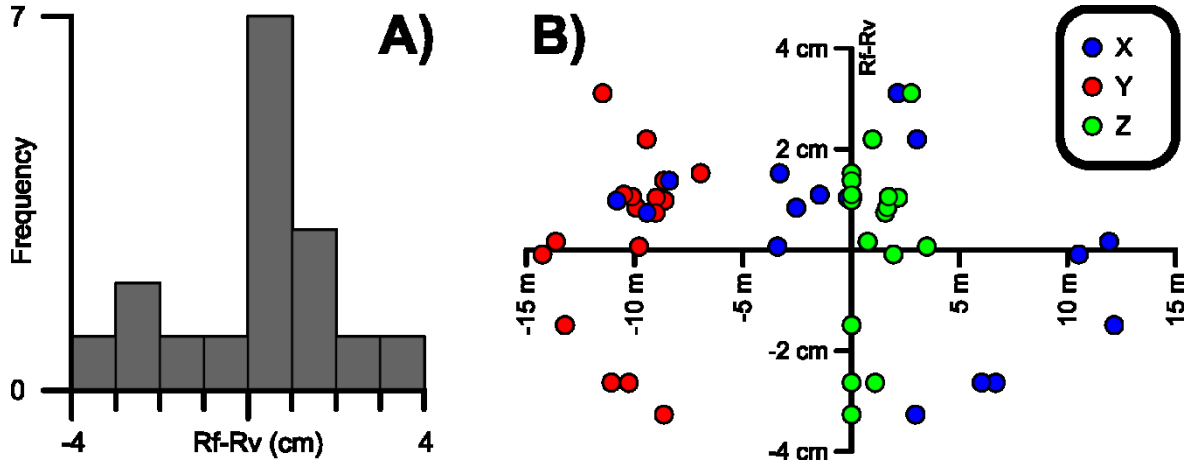

Figure 14. Difference between measured (Rf) and digitally computed (Rv) distances of targets from the origin in the Rocca di Cave outcrop. (A) Frequency distribution of Rf-Rv. (B) Scatterplot with Rf-Rv values along the Y-axis and X, Y, and Z coordinates of the target along the X-axis of the plot.

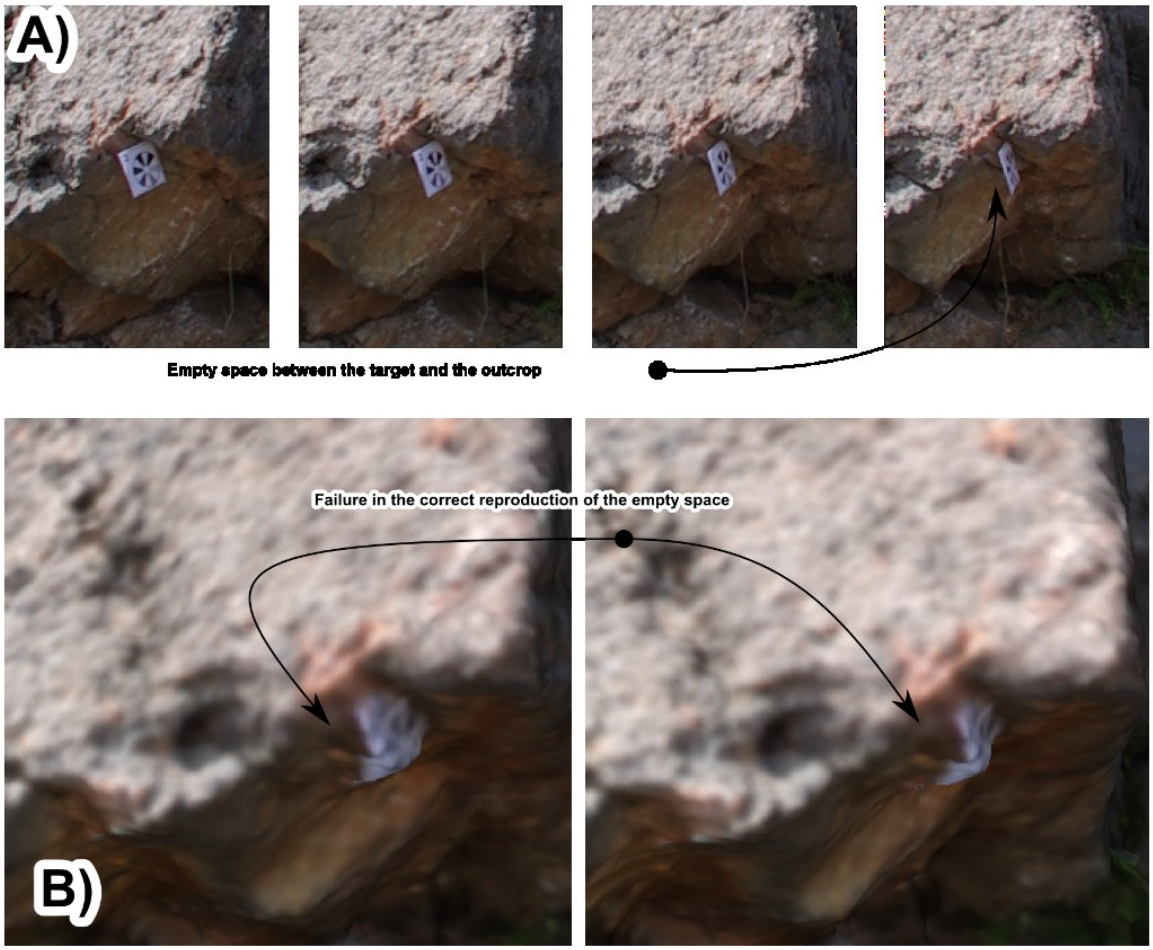

Figure 15. Example of second order distortion during reconstruction of a coded target not pasted onto the outcrop's surface. (A) Photographic dataset. (B) Digital model, where the empty space between the outcrop and the coded target was not successfully reproduced. Instead, the target was deformed and an error occurred.

The textured sub-meshes were imported into the OpenPlot software, where bedding attitudes were extracted directly from the textured sub-meshes using both of the previously-described procedures.

Despite the high resolution of both the second point cloud and the triangular mesh, the resolution of the first mesh was 0.4 points/cm^2 and the maximum error of the VOM was about 4 cm. In order to avoid errors, it was chosen to digitized only planar features having an exposed area of at least 100 cm^2 (Figure 6) through the orientation analysis of the mesh.

A total of 138 bedding surfaces of the Miocene calcarenites were digitized (Figure 16).

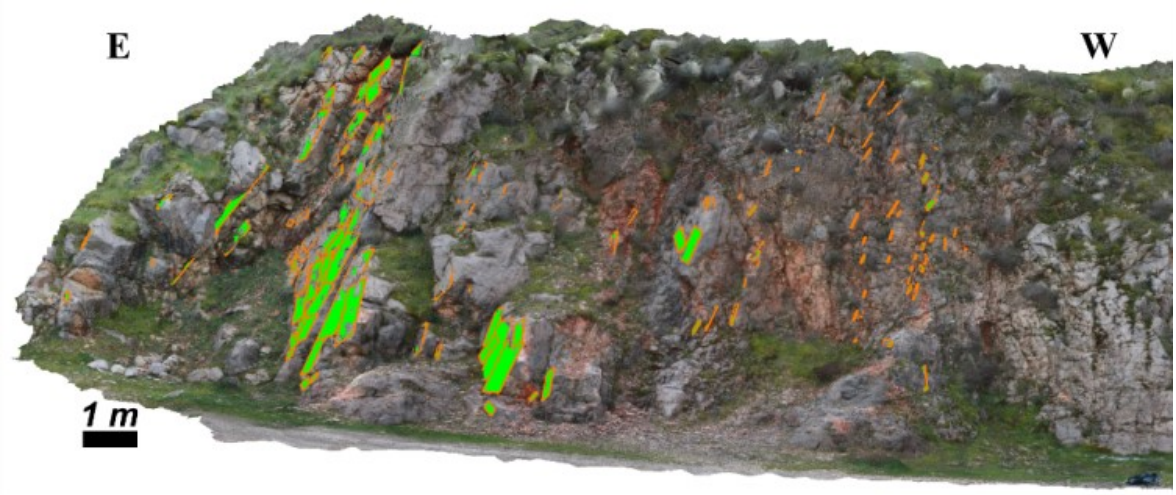

Figure 16. View of the Rocca di Cave outcrop model in OpenPlot, with digitalized bedding surfaces (green polygons).

Beds strike about NNW-SSE and dip 60-70° toward ENE (Figure 17). The tensor analysis of poles to beds (e.g. Whitaker and Engelder, 2005) provides three eigenvalues and associated eigenvectors that represent the direction of maximum (K1), minimum (K3), and intermediate (K2) pole concentrations.

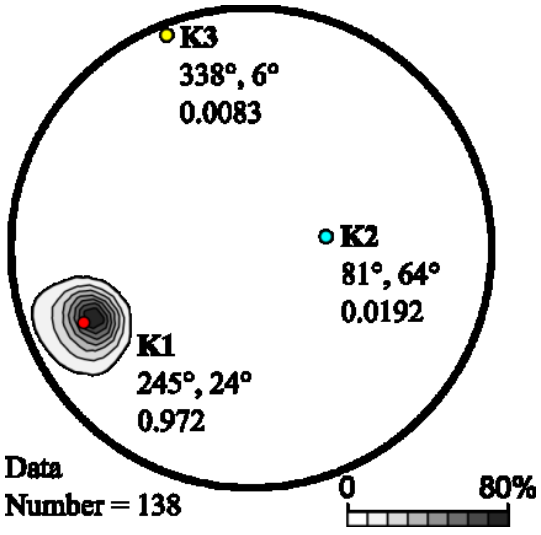

Figure 17. Frequency contour in stereographic equal-area projection of poles to digitalized bedding surfaces together with results of the tensor analysis (i.e. eigenvalues and associated eigenvectors).

The observation that K3 is about half K2 indicates that poles to bedding are well clustered along a plane oriented perpendicularly to K3. In other words, K3 coincides with the beta axis (i.e. the direction of intersection between the bedding planes).

The K3 was then used to reorient the VOM in PhotoScan so to obtain a coplanar-to-bedding orthorectified view of the outcrop. An about 4-pixel/cm^2 orthorectified image was hence exported using this view (Figure 18a). Subsequently, this image was imported in Inkscape (a vector graphic drawing software) where beds were traced (Figure 18b) as it is usually done when picking horizons on a seismic reflection profile. From this line drawing, a properly oriented (i.e. orthorectified and oriented perpendicularly to beta axis) scheme was produced and rotated in order to restore the uppermost Miocene beds to its original horizontal attitude (Figure 18c). This simple rotation procedure revealed that Miocene beds (i.e. their formation) are at least partially sin-kinematic, as they form a growth wedge (Tavani, Vignaroli, et al., 2015).

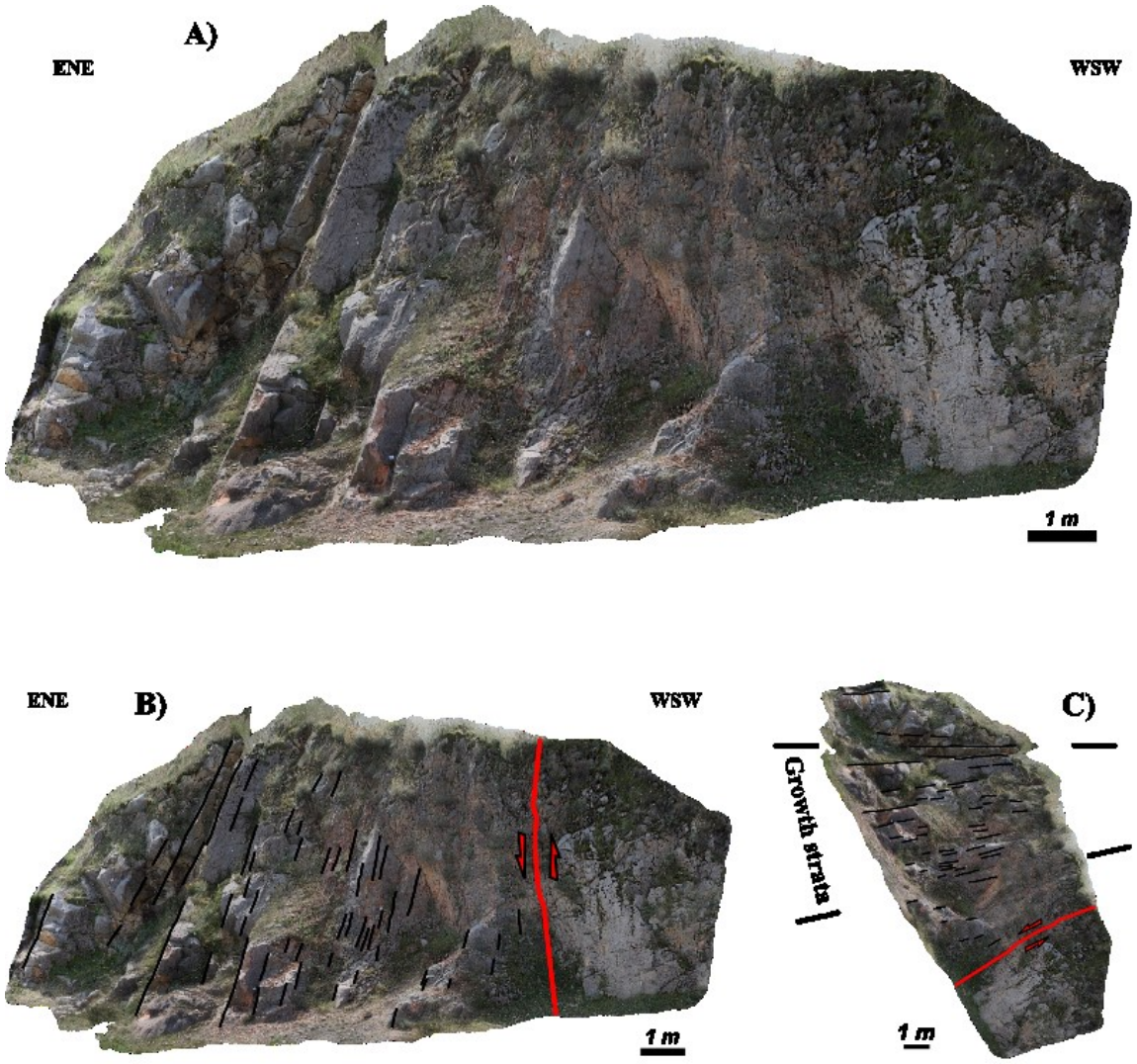

Figure 18. (A) 4 pixel/cm^2 orthorectified photograph of the outcrop produced in PhotoScan by using K3 as point of view. (B) Line-drawing of layers shown in the previous photograph. (C) Rotation of the orthorectified and interpreted model, showing the fan geometry and syntectonic origin of the Miocene Calcarenites.

3.1.2 The San Severino outcrop

The San Severino outcrop is a barely accessible steep cliff located in the eastern (outer) sector of the Apennines fold-thrust belt at the following coordinates: latitude 43°13'28"N and longitude 13°07'5"E. The outcrop is E-W-oriented and consists of a 10 m wide and 10 m high exposure of shallow dipping Mesozoic carbonate layers of the Maiolica formation affected by an embryonic normal fault (Figure 19a) (Tavani et al., 2012).

Only the lower part of the outcrop is accessible and the cliff can be photographed only from ground level. Accordingly, in order to cover the upper part of the outcrop with at least three sets of photographs, we took photographs at different distances from the outcrop (5 to 15 m) and with different focal lengths, which resulted in a resolution ranging from 1 to 0.2 pixel/mm^2. Moreover, as it was not possible to position the coded targets in the upper portion of the cliff, only for this portion of the outcrop, random targets were set using a long-distance highly visible green light laser pointer and contextually measured with the distance meter and photographed (Figure 19b).

In total, including photographs of these "flying targets", 156 photographs were used to build the VOM. The first point cloud was made of 1.8x10^6 points with a resolution of about 0.2 points cm^2 (Figure 19c), while the dense point cloud was 9x10^6 points. The latter was cut to remove the uppermost portion of the cliff, which was not affected by faulting, and vegetated areas, for a remaining surface of about 220 m^2 (that is 4 points/cm^2) (Figure 19d).

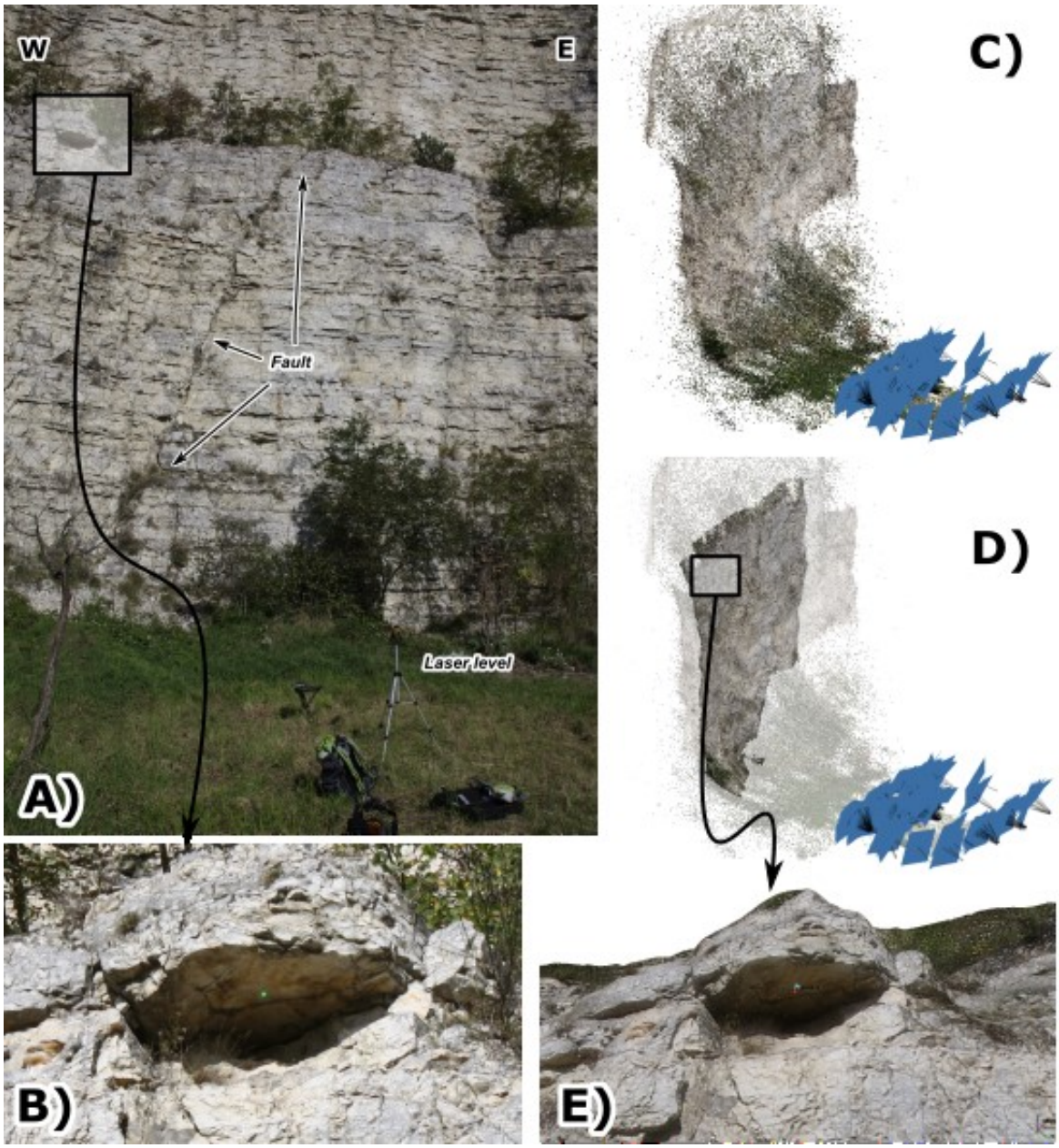

Figure 19. (A) Photograph of the San Severino outcrop showing the near vertical cliff and the embryonic normal fault along with the laser level. (B) Example of a "flying target" made with a green laser light. (C) RGB coloured point cloud of the outcrop, with position of photographs indicated. (D) Dense point-cloud. (E) View, in the 3D digital model, of the target in B.

The subsequent 3D triangulation of points enabled a triangular mesh made of $1x10^7$ irregular triangles (having an average area of about 0.2 cm^2) to be obtained. The model was then scaled and re-oriented using all targets including the "flying targets" (Figure 19e).

The VOM error (Rf vs. Rv) was found to range between about -4 and 6 cm (Figure 20a). Similarly to the Rocca di Cave outcrop, also in this outcrop errors are insensitive to the X, Y, and Z coordinates (Fig. 11b). One target is affected by a greater error (i.e. 20 cm). We disregarded this latter value, as it is probably associated with a measurement error. Removing this anomalous value, we obtained that the average value of the absolute errors is 2.8 cm.

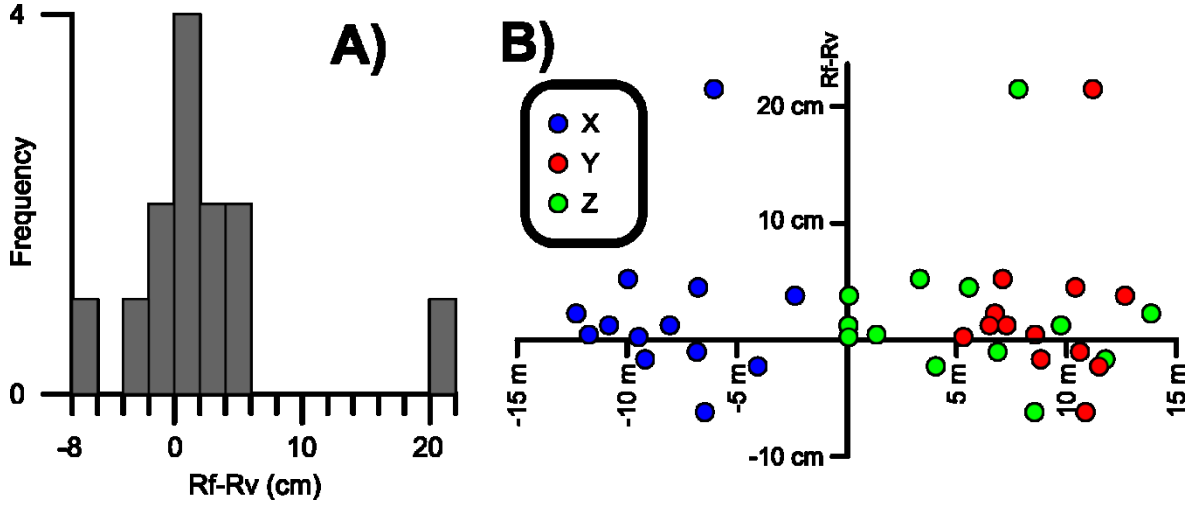

Figure 20. Difference between measured (Rf) and digitally computed (Rv) distance of targets from the origin in the San Severino outcrop. (A) Frequency distribution of Rf-Rv. (B) Scatterplot with Rf-Rv values along the Y-axis and X, Y, and Z coordinate of the target along the X-axis of the plot.

After the above described operations (i.e. triangulation, scaling, and re-orientation of the model), the mesh was split into four sub-meshes, thus deriving four 4096x4096 pixels texture images, which were draped over the sub-meshes.

In OpenPlot, 248 attitudes of meso-structures were measured: 58 bedding surfaces, 140 joints, and 50 segments of the study fault (Figure 21a).

Bedding surfaces identify a single maximum corresponding to a N302°-striking and NE3°-dipping plane (Figure 21b). Joints mostly consist of high-angle-to-bedding surfaces striking E-W and N-S (Figure 21b). The digitized

segments of the fault are clustered around a single maximum corresponding to a N191°-striking and NW74°-dipping plane (Figure 21b).

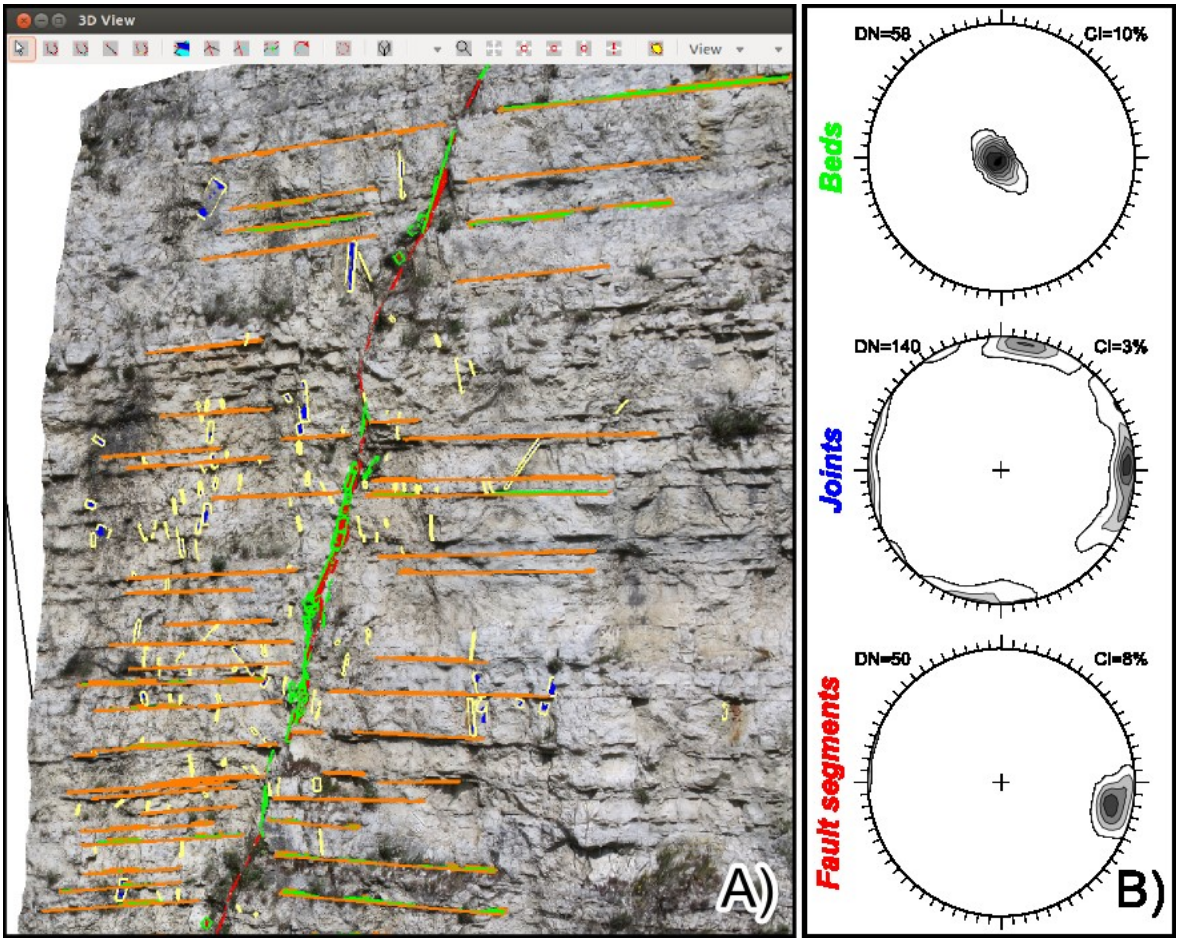

Figure 21. (A) View of the San Severino VOM in OpenPlot, with digitalized bedding surfaces (green polygons with orange outline), fault segments (red polygons with green outline), and joints (blue polygons with yellow outline). (B) Frequency contour in stereographic equal-area projection of poles to digitalized bedding surfaces, joints, and fault segments. DN and CI refer to data number and contouring interval, respectively.

From tensor analysis of these data, three mutually orthogonal versors were derived: the bedding-fault intersection versor, the bedding-normal versor and the one orthogonal to both. The VOM was hence rotated in PhotoScan to obtain, in orthographic view, a frontal view of the plane oriented perpendicularly to both bedding and the fault.

A 4-pixels/cm orthorectified photograph was exported from PhotoScan and subsequently imported in Inkscape, where beds and fault segments were traced (Figure 22a).

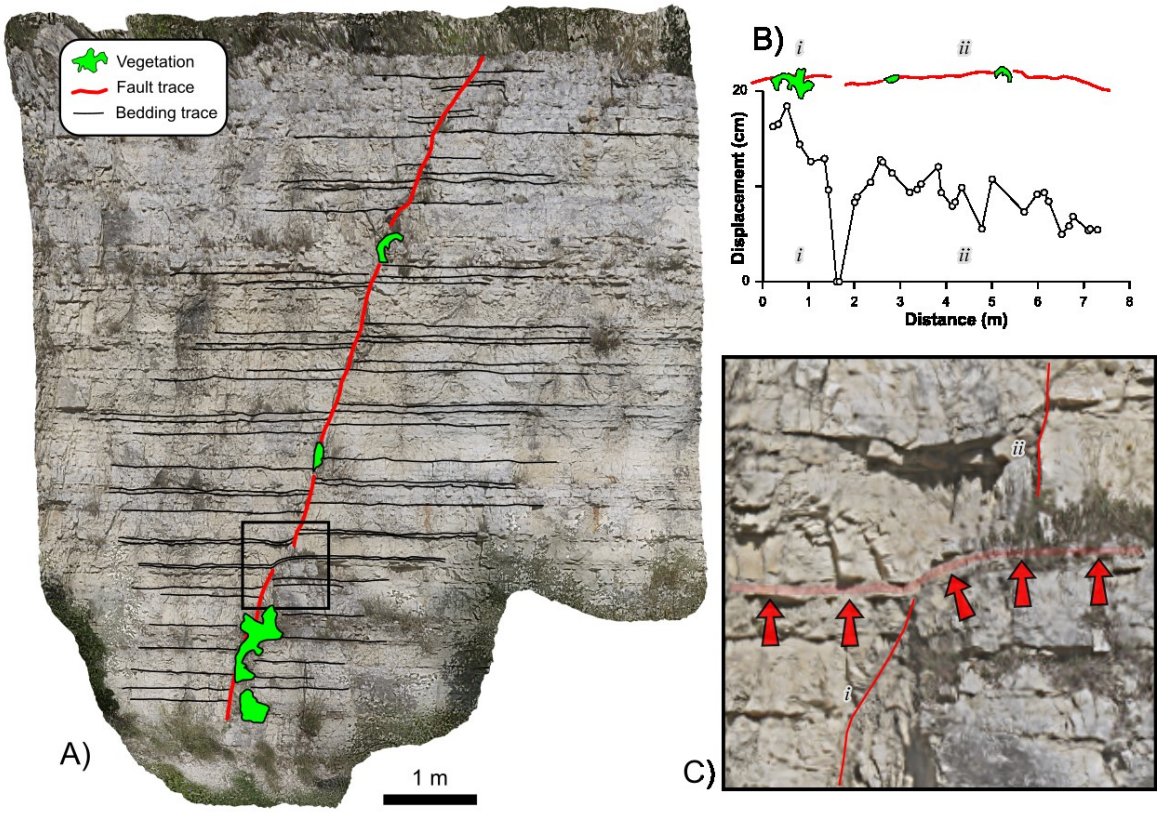

Figure 22. (A) Orthorectified photo with line-drawing of layers and fault segments in the San Severino Outcrop. (B) Fault stratigraphic separation diagram. (C) Close-up of the folded area indicated in A.

From this line drawing, the resulting properly oriented (i.e. orthorectified and oriented perpendicularly to both bedding and fault) scheme, was used to get measurements of true thicknesses and stratigraphic displacements. Using this scheme, it was possible to correlate cutoff points of hanging wall and foot-wall strata and hence to construct a stratigraphic separation diagram (Figure 22b). In particular, it was possible to observe a folded area along the fault (Figure 22c), between segments i and ii, where layers are folded and bent toward the fault (Figure 22b).

3.1.3 The Frontone outcrop

The Frontone outcrop is located in the outer sector of the Northern Apennine, and in particular in the frontal sector (NE) of the Mt. Catria anticline (e.g. Alvarez et al., 1978; Marshak et al., 1982; Geiser, 1988; Barchi et al., 1991; Chilovi et al., 2002; Massoli et al., 2006), which is a structure involved in the Apennines' Thrust Wedge during the Messinian (Elter et al., 1975; Bigi et al., 1989).

Along the outcrop, a plunging meso-fold, with straight limbs (e.g. kink folds), was studied (Figure 23). This fold affects strata belonging to the Maiolica formation, characterized by thinly to medium bedded whitish micritic limestones that show typical conchoidal fracturing, and grey or blackish cherty nodules and layers.

Figure 23. Photograph of the Frontone study outcrop showing folded strata belonging to the Maiolica formation. The fold has an outcropping amplitude of at least 4 meters and an half-wave length of 2.5 meters. Laser level is 40 cm long.

The fold in question is characterized by both bedding-parallel and bedding-perpendicular pressure solution surfaces (PPS), fractures and veins.

These latter are evident within the outer arc of the hinge zone, where the thickness of the strata clearly increases.

Although a series of geological sizes could be estimated in the field, there are a series of observations that require specific points of view for calculations and classifications. In this case study, this is the direction of the fold axis, since folds should be observed on a section that is orthogonal to it.

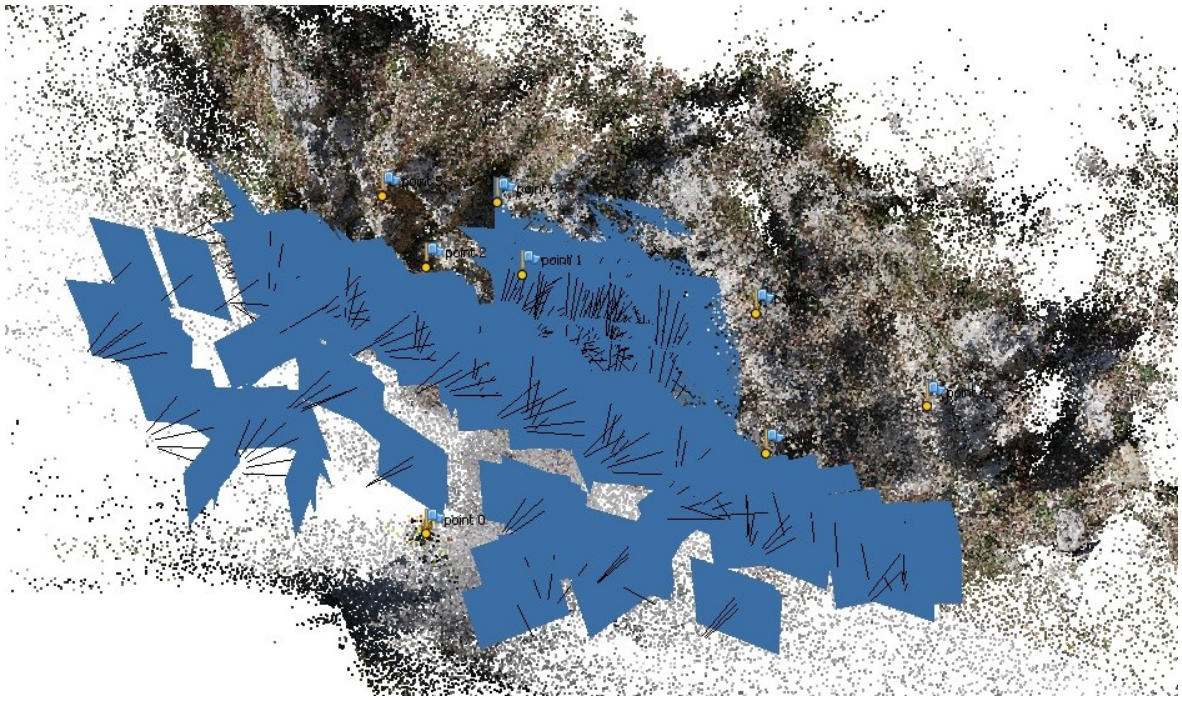

Figure 24. RGB coloured point cloud of the Frontone outcrop with spatial distribution of photographs used to build the cloud, as seen in Agisoft PhotoScan. The outcrop was over-abundantly photographed from both distance and very close to the fold, to gather an extremely high dense point cloud.

The outcrop was photographed with two cameras, a Canon EOS 450D and a Canon EOS 1100D, both sharing a 12.1 Mpixel sensor. 351 photographs, taken at various distances from the outcrop, were used to build an extremely detailed (dense) VOM of the fold in PhotoScan (Figure 3). These photos can be grouped in about three sets (as seen in Figure 24). Close ups photos of the sole studied fold cover a photographed area of about 0.33x0.22 m each (i.e. 167 pixel/mm^2). Photos from the second line (as seen in Figure 24) that are

perpendicular to the outcrop portray an area of about 2.32x1.55 (i.e. 3.4 pixel/mm^2), while it is tricky to define the resolution of photos that are at different angles with the outcrop (however we know that these have lower resolution). Finally, perpendicular photos from the third line have resolution of about 1.59 pixel/mm^2.

The first point cloud was made from 2.2x10^6 points with a resolution of about 5.5 points per cm^2 within the much photographed area (Figure 24), while the dense point cloud, made of 2.3x10^7 points, had a resolution of about 58 points per cm^2 within the same area. The resulting mesh was made of 2.2x10^7 triangles (having an average area of about 1.8 mm^2). The model was then scaled and re-oriented using the position of the targets measured with the laser level as described for the former case studies.

The VOM error (Rf vs. Rv) was found to range within about ±2 cm (Figure 25a). As observed in the Rocca di Cave and San Severino outcrops, error is insensitive to the X, Y, and Z coordinates (Figure 25b).

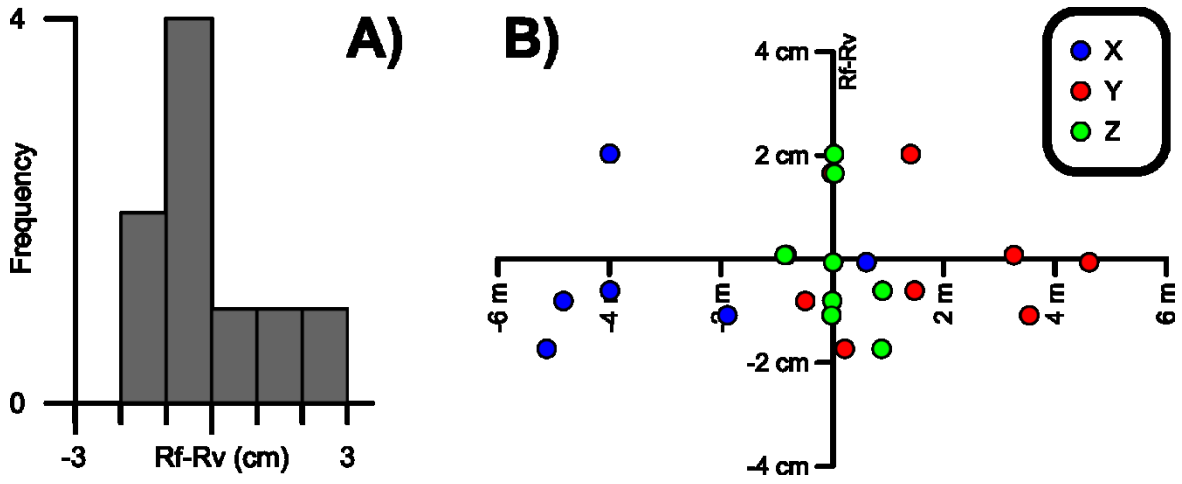

Figure 25. Difference between measured (Rf) and digitally computed (Rv) distances of targets from the origin in the Frontone outcrop. (A) Frequency distribution of Rf-Rv. (B) Scatterplot with Rf-Rv values along the Y-axis and X, Y, and Z coordinates of the target along the X-axis of the plot.

Later, the mesh was split into ten sub-meshes, thus deriving ten 4096x4096 pixels texture images, which were draped over the sub-meshes in PhotoScan.

In OpenPlot, 166 surface attitudes were measured (Figure 26a), in particular 65 were bedding surfaces and bed-parallel PSS, and 101 were among bed-perpendicular PSS, fractures and veins.

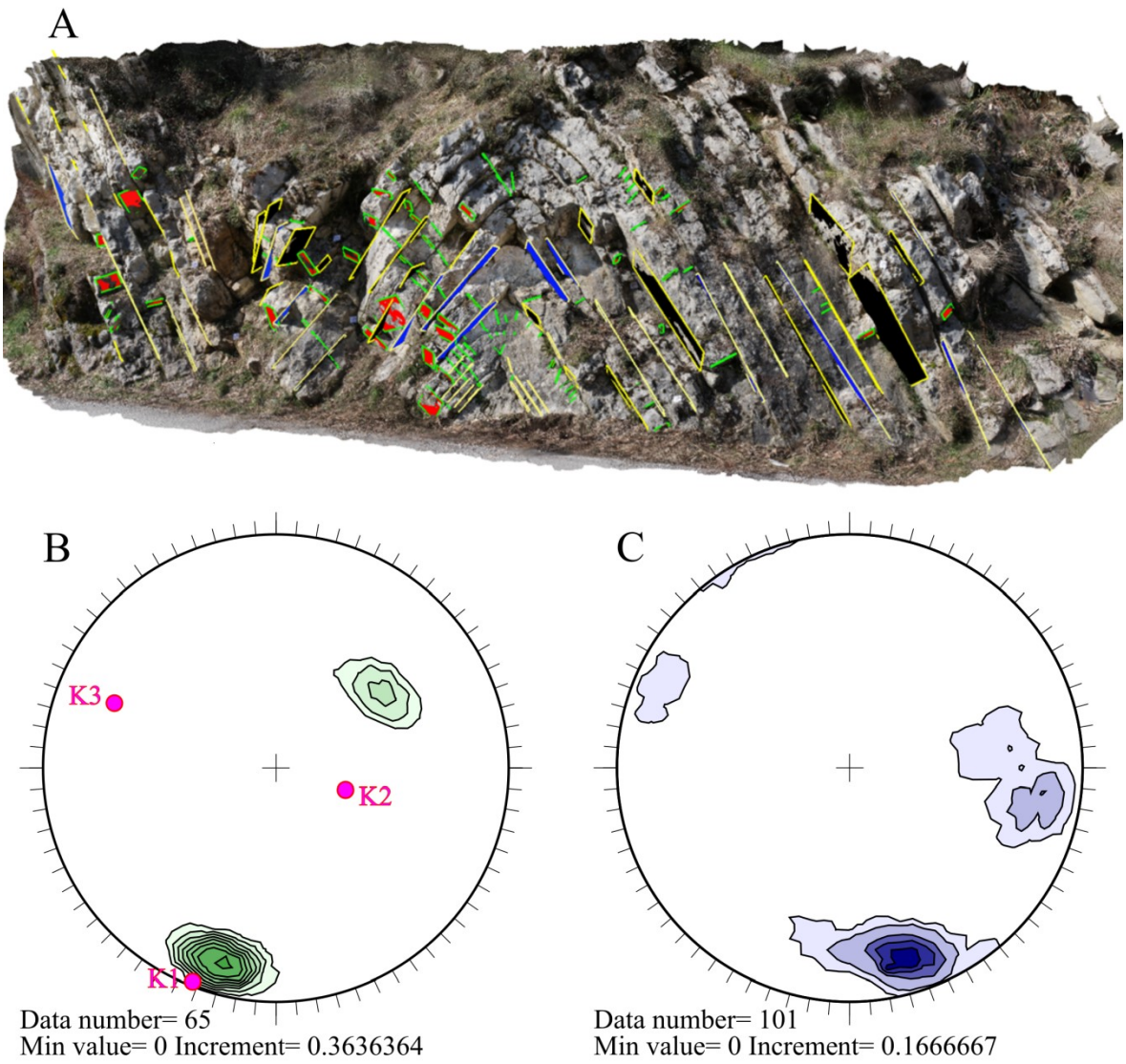

Figure 26. (A) View of the Frontone VOM in OpenPlot, with digitalized elements. (B) Contour plot of poles to bedding and bed-parallel PSS with results of tensorial analysis. (C) Contour plot of poles to non-bed-parallel PSS and fractures.

Bedding surfaces and bed-parallel PSS identify two maxima corresponding to planes dipping at 17/74 (Dip azimuth/Dip angle) and at 234/45 (Figure 26b). Non-bed-perpendicular PSS and fractures form two major maxima corresponding to planes dipping at 273/73 and 342/74, and a less representative one that corresponds to a plane dipping at 115/81 (Figure 26c).

From tensor analysis of bedding and bed-parallel PPS, three mutually orthogonal eigenvectors with their relative eigenvalues were derived (Figure 26b). In particular, the smallest eigenvalue corresponds to the direction of minimum concentration of poles and hence to the direction of the intersection between the two limbs of the fold (i.e. the statistical direction of the fold axis).

Confronting the two stereo plots of Figure 26, it is evident that the position of the smallest eigenvalue lies within the weak maxima observed in Figure 26c; this maxima hence corresponds to fractures that are perpendicular to fold axis and almost parallel to the outcrop wall.

The direction of the smallest eigenvector, 292/26 (Azimuth/Dip), was used to calculate the position of the markers in a coordinate system where one of the axes is parallel to the fold axis. This is achieved by rigid rotation of the point cloud around the origin as previously described. After updating these coordinates in PhotoScan, the orthographic view of the model was exported (Figure 27).

The size of the angle between the two limbs (i.e. the interlimb angle) is 72.2°, so the fold can be classified according to its degree of tightness/openness as an open fold (120°-70°) (Fossen, 2010).

Figure 27. Orthorectified view of the Frontone outcrop.

The fold, as observed in the orthographic view (Figure 27), can be classified with two distinct superposed profiles. In fact, in the inner part the fold is characterized by a typical chevron shape, with long planar limbs and a short, angular hinge zone, while the hinge zone of the outer part presents a round shape. The strata in the inner part also present a major thickening of the hinge with respect to the thickness of the fold limbs.

Using the exported image, it was also possible to classify the fold on the basis of isogons (Ramsay and Huber, 1987). In essence, isogons are lines connecting points with equal dipping angle at the two sides of a folded stratum. AutoCAD® software was used to construct isogons along two strata of the fold has shown in Figure 28.

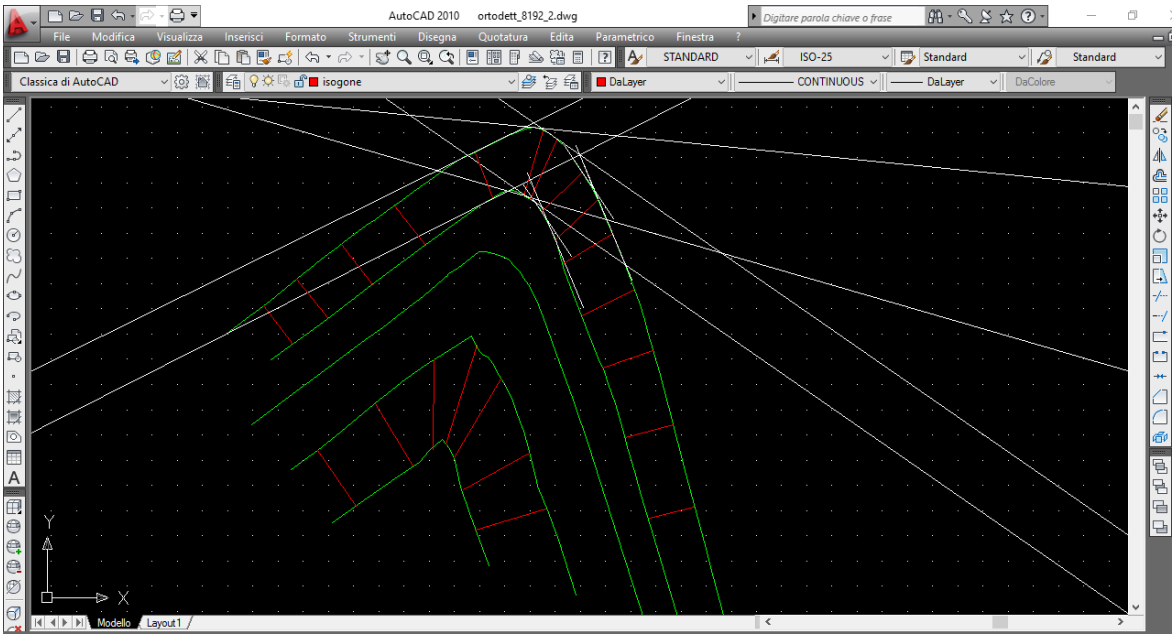

Figure 28. Isogons construction with AutoCAD® software.

Once isogons are constructed in vector graphics software it is then possible to classify the folds according to dip isogons using the diagram shown in Figure 29. In this diagram, folds must be first rotated in order to set vertical their axial plane so that the dip of the limbs (α) increases in each direction from the hinge (Figure 29a). For each isogon, the normalized orthogonal thickness (t'_α) is calculated as the thickness measured orthogonal to the layer (t_α) at one of the two corresponding points of equal dip on each arc (red dots in Figure 29a) divided by the thickness along the axial plane (t_0) (Fossen, 2010).

When the calculated t'_α for the two folded strata of the fold in question are plotted against α (Figure 29b), the fold can be classified in between Class

1C and Class 2 according to Ramsay (1987), which are characterized by slightly and moderate thinned limbs, respectively.

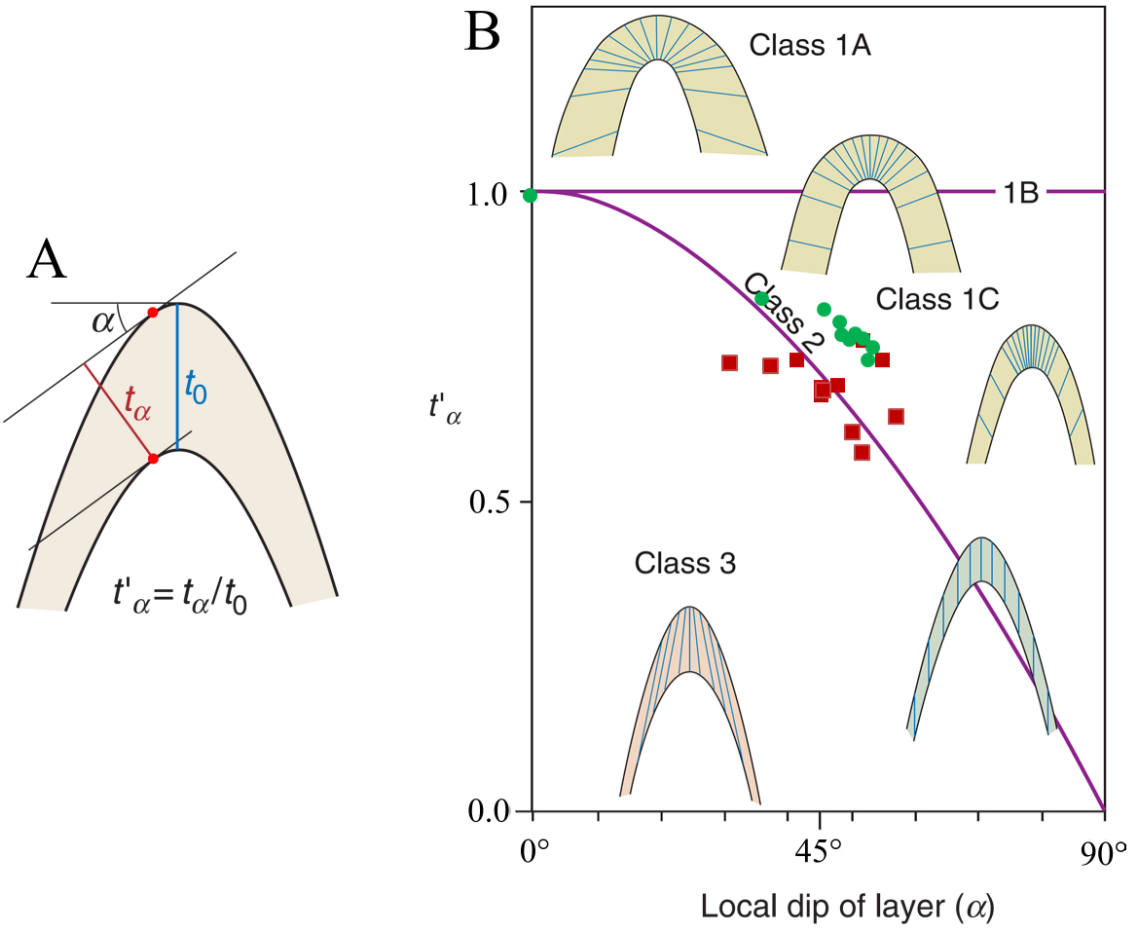

Figure 29. (A) Scheme showing how to obtain the values that are later imported in the diagram in B. (B) Diagram of fold classes according to Ramsay (1967) *for the two strata of Figure 28. From* Fossen (2010)*, modified.*

3.2 EVALUATING ROUGHNESS SCALING PROPERTIES OF FAULT SURFACES

3.2.1 Theory and Background

Faulting is the result of sliding between two pieces of rock that are in contact. This sliding over an already pre-existing surface is described by the Amontons' law:

$$|\tau| = S_0 + \mu_f \sigma_n$$

where τ is the shear stress acting along the plane and σ_n is the normal component; μ_f is the coefficient of friction and S_0 is a term similar to cohesion (e.g. Jaeger et al., 2009).

The Amonton's law differs from the Coulomb's failure criterion for intact rocks:

$$|\tau| = C_0 + \mu_i \sigma_n$$

where μ_i is the coefficient of internal friction, which is the slope of the failure envelope on a $\sigma_n - \tau$ plane and C_0 is the cohesion of the intact rock.

Those laws, even when expressed in terms of the effective normal stress:

$$\sigma'_n = \sigma_n - P_f$$

where P_f is the pore fluid pressure, do not explain the role of time-, temperature-, slip-, or slip rate-dependent processes in driving instability as observed during laboratory tests (Lockner and Beeler, 2002). In essence, the

experimental evidences relating friction to hold time, slip velocity and displacement are well described by rate and state friction laws, whose fundamental equation is given by:

$$\mu = \mu_0 + a \ln\left(\frac{V}{V_0}\right) + b \ln\left(\frac{V_0 \theta}{D_c}\right)$$

where μ is the frictional resistance (or friction), μ_0 is a constant appropriate for steady-state slip at a velocity V_0, V is the frictional slip rate, θ is a state variable, and a and b are empirical constants (Marone, 1998). D_c, which is known as the critical slip distance, is related to the dimensional properties of the fault asperities and controls the stability of sliding (Dieterich, 1979). It is hence evident that fault asperity dimension, and hence roughness, is one of the parameters involved in the mechanics of fault slip (Power et al., 1987) and, therefore, it may have implication on seismic hazard assessment. In addition, roughness may control the geometry of faults (Power et al., 1987) and may affect the development of their spatial architecture (Candela et al., 2012 and references therein), thus influencing, to some extent, the compartmentalization and the permeability of faults.

Many studies in earth sciences have been addressed by fractal analysis (i.e. studying natural geometries that exhibit a repeating pattern at various scales). When geometries are repeated and appear exactly the same at every scale, this is said to be a self-similar behaviour. When an object instead scales by different amounts in the x- and y-direction, this is said to be a self-affine behaviour. In essence, for a self-affine object, we can observe the same geometry after rescaling in x- and y-directions in a certain different way.

For a self-affine 2-D surface Z(X,Y) with coordinates (X,Y) the following relationship describes the scaling where

$$Z(X,Y) \sim X^{1/H_X} \sim Y^{1/H_Y}$$

where H_X and H_Y are the scaling exponents, also known as Hurst exponents or indexes of dependence, respectively in the x- and the y-direction. Since it is not possible to derive the scaling exponents of self-affine scaling transformations (e.g. Sapozhnikov and Foufoula-Georgiou, 1995), different methods have been developed during the years for their estimation (e.g. Candela et al., 2009). Among them, a Fourier power spectrum method has been preferred (e.g. Sagy et al., 2007; Candela et al., 2009, 2012; Bistacchi et al., 2011; Renard et al., 2012, 2013; Davidesko et al., 2014) having proved to be both robust and consistent. Using this method, the Fourier power spectrum P(k) (i.e. the square of the modulus of the Fourier transform, Schuster, 1898) of a 1D fault profile Z(X) is calculated as a function of the wavenumber k. After plotting the Fourier power spectrum as a function of k in a bi-logarithmic scale graph, a self-affine function exhibits a linear slope, which is itself a function of the Hurst exponent through $P(k) \propto k - 1 - 2H$. A spectrum representing the entire rough surface in a certain direction is given by stacking several power spectra and averaging to reduce noise associated with single profiles.

Early studies on fault roughness (e.g. Power and Tullis, 1991; Lee and Bruhn, 1996) suffer for the accuracy limitations of the instruments used to obtain fault profiles (Candela et al., 2009). With the development of new generation of laser scanners, increasingly accurate topographic data can now be collected, allowing fault surfaces to be better characterized in the 3D space (Renard et al., 2006; Sagy et al., 2007; Candela et al., 2009; Brodsky et al., 2011). In particular, recent work has shown that roughness decreases along the slip-parallel direction with increasing slip.

For instance, a recent study by Candela et al. (2012) has investigated the roughness of fault surfaces over nine decades of length scale using three different scanner devices (a laser scanner, a laser profilometer and a white light interferometer) (Figure 30). Their work has shown that fault roughness shows a single anisotropic self-affine behaviour over 50mm and 100 m scale.

Observation at smaller scales, such as at micro- and nano-scales, by means of atomic force microscopy (ATM), has shown that no anisotropy is observed below the micro scale and that roughness is not self-affine at all scales being smoother at the nanoscale (Siman-Tov et al., 2013).

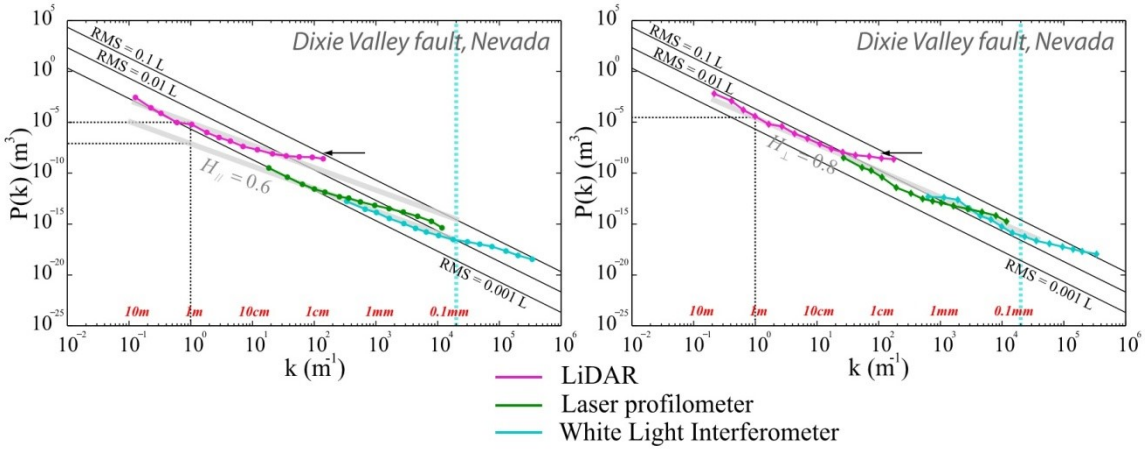

Figure 30. Fourier power spectra of Dixie Valley fault along two perpendicular directions, from Candela et al. (2012). In particular, black arrows indicate a "saturation effect" of the LiDAR due to noise. Please, refer to text for further explanations.

In this section, a series of fault roughness topographies have been acquired by means of photogrammetry in order to test and prove its potential even in this peculiar application. In particular, since standard laser scanners have a noise of about 1 cm in distance (e.g. Candela et al., 2012), these devices may be only used to study large scale anisotropies, and one must resort to other methods, such as laboratory laser profilometers, to resolve the roughness at smaller scales.

By contrast, the resolution of photogrammetry is strictly related to photograph resolution and a broader scale range than would be obtained using only a laser scanner, can be studied simply using this highly versatile method. In particular, as showed by Candela et al. (2012) and indicated by the black arrows in Figure 30, the laser scanner method reaches saturation in resolution below about 9 cm.

In this work, point clouds of natural fault surfaces were obtained using the photogrammetric method. Those point clouds were hence loaded into Matlab, where their self-affinity, estimated from Fourier power spectra, was tested following, and to a certain extent improving, the procedures described in Candela et al. (2009, 2012), Bistacchi et al. (2011), and Renard et al. (2013), among others. In particular, my Matlab code, and hence the analytical part of the workflow, is described in the next subchapter.

3.2.2 Fourier Power Spectrum (PFS) analysis method

Each fault point cloud is imported into Matlab as a 3-D [xyz] matrix (X), where the first two columns (x and y) define the 2D coordinate position over the fault plane and the last column (z), perpendicular to the plane xy, defines the fault heights (i.e. roughness). Since it is highly unlikely that these z values are, at this stage, perfectly perpendicular to the mean fault plane (Figure 31A), a best fit plane of the point cloud is obtained and then the point cloud is rotated through the `ROTATION.M` (Appendix 1) function in order to set z perpendicular to the best fit plane. In essence, through this function, the new z column is equivalent to the residual distances of the orthogonal distance regression `LSPLANE.M` (Least-squares plane from Mathworks repository) (see Appendix 1).

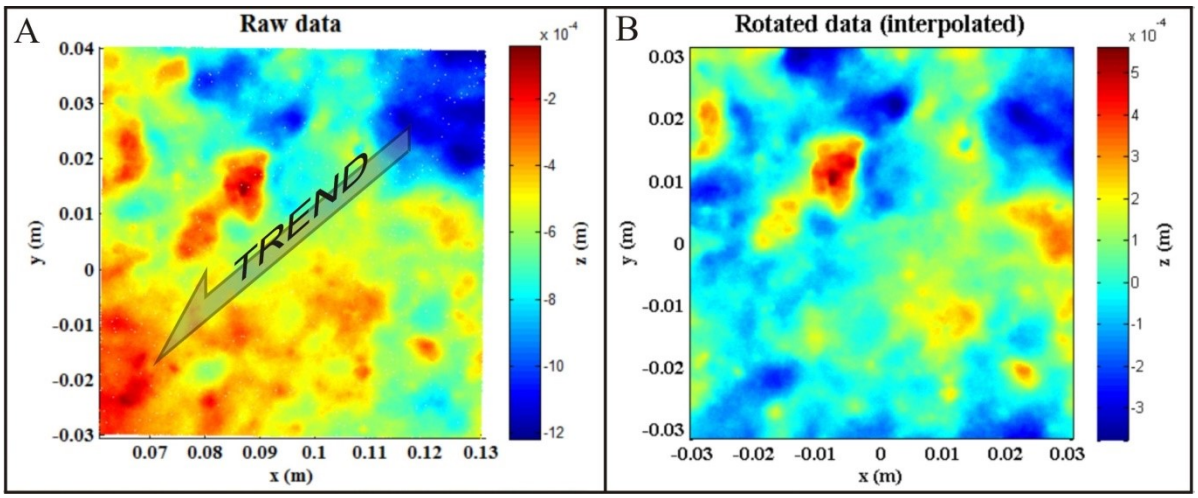

Figure 31. These are examples of (A) a point cloud of a smoothed fault affected by unnatural trend, and (B) the same fault after rotation and interpolation. Please note that z is times10^{-4}.

In particular, in `LSPLANE.M`, the best fit plane is calculated by single value decomposition that returns, among other things, the direction cosines of the normal to the best-fit plane ($\hat{z}_{new}$). The new coordinate system is centred with the centroid of the data (i.e. the mean position of all the points in all of the coordinate directions that by definition lies on the best-fit plane) (Figure 31B).

In ROTATION.M The new direction of $\hat{x}$ ($\hat{x}_{new}$) is defined by the cross product between $\hat{z}_{new}$ and $\hat{z}_{old}$, while $\hat{y}_{new}$ is the cross product between $\hat{z}_{new}$ and $\hat{x}_{new}$. A further arbitrary rotation around $\hat{z}_{new}$ defined by the variable "r_deg" is then needed to match $\hat{x}_{new}$ or $\hat{y}_{new}$ with the fault slip direction prior to extracting the 2D signal for the PFS analysis.

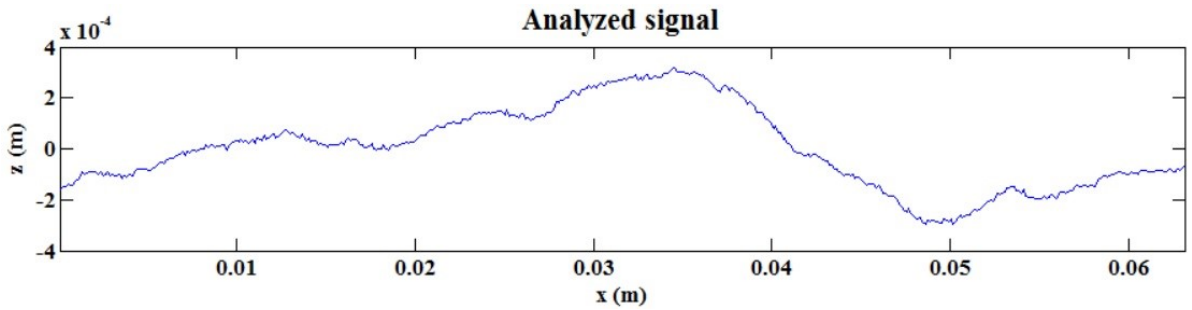

Figure 32. This is one of the profiles that were analyzed. In particular this is the along slip profile number 440 that passes through the sample of Figure 31 across x=0. Not in scale.

Once rotated, the new matrix (Xnew) has to be converted to a 2-D (xy) matrix and a 1-D (z) vector (Renard et al., 2006; Sagy et al., 2007; Candela et al., 2009) with the direction of $\hat{z}$ now perfectly perpendicular to the mean fault plane. Minor distortion, resulting from this rotation, was evaluated confronting the new z vector with the residual distances; discrepancies were found in the order of 10^{-15}.

The new xy matrix consists of irregularly spaced coordinates, while a regular sampling rate is needed for Fast Fourier Transform (FFT) algorithms to work. For this reason, through the INTERPOL.M (Appendix 2) function, a regularly spaced grid with spacing defined by the variable "samp" is built (Figure 31B) and the corresponding linearly interpolated z value stored in a mxn matrix (qz), where m and n are the number of resampled points along the x and y dimensions respectively. As suggested in Candela et al. (2012), "samp" is systematically chosen to be twice as large as the average irregular spacing of the original point clouds and it has to be manually defined in the script. In my

workflow, the overall 3D rotation and 2D interpolation has been preferred regardless of what done by previous authors, who had chosen to detrend and to interpolate each 1D profile independently; in my opinion, my approach helps to preserve long wavelengths and improve interpolation.

The FFT analysis through the surface, that, at this stage, is defined by the regularly spaced (as defined in "samp") interpolated grid qz, is finally achieved using a 1-D FFT approach (Renard et al., 2013). In essence, each row and then each column of the matrix qz is extracted (Figure 32) and analysed independently (Figure 33). This is achieved through the functions `positiveFFTx.M` (Appendix 3) and `positiveFFTy.M` (Appendix 4) along the x and y directions, respectively, and averaged to obtain a representative mean Fourier power spectrum for each direction. Please refer to comments in these scripts for further explanations.

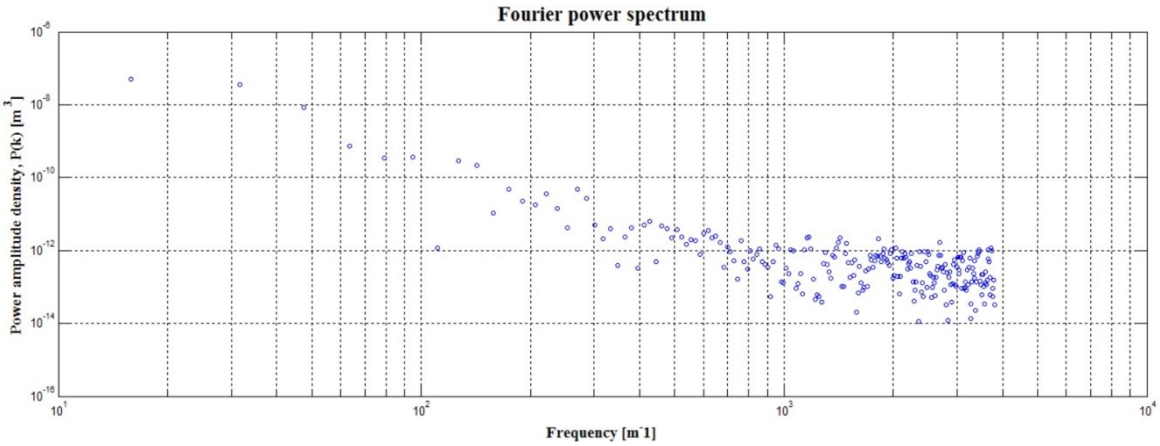

Figure 33. Fourier power spectrum of the signal in Figure 32.

3.2.3 Reproducibility of small scale features

Since the photogrammetric method, has not been applied to the study of 3D surface roughness, a preliminary effort was made in order to test if photogrammetry was capable of reproducing fault anisotropies with enough detail and accuracy. For these reason two independent testing paths were followed: (1) producing 3D models of rough objects of known size, and (2) testing if a 3D model of a photogrammetry-derived fault surface shares similar self-affinity properties of faults gathered with more established methods, and in particular with scale ranges generally covered by laser scanners and laser profilometers. The latter test has, of course, the dual role of validating the method and describing the workflow to evaluate roughness scaling properties.

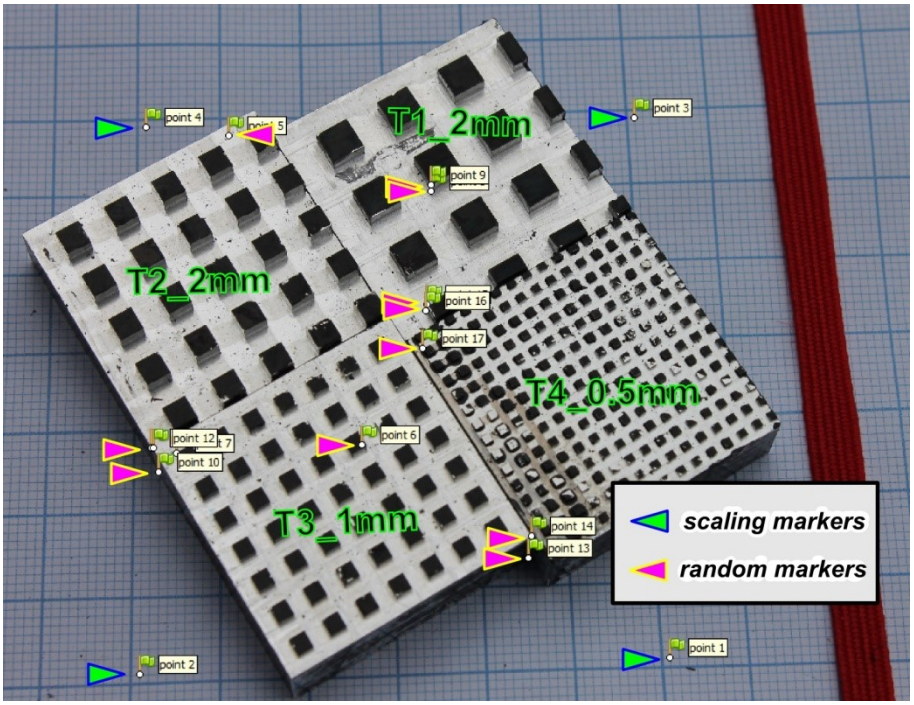

Figure 34. Control objects of known size characterized by asperities heights of about 2mm (with two different bases, T1 and T2), 1mm (T3) and 500µm (T4). Those objects were photographed over a graph paper in order to scale the model very quickly and precisely using scaling markers. Further markers (here called random markers) were used to improve model building.

Four objects (here referred as control objects), each characterized by regularly-spaced squared asperities of one certain size (Figure 34), were produced at the Department of Physics at Durham University. Those objects, with asperities from about two to half millimetres, are made of steel and present mirror surfaces. Since reflections are unnatural and prejudice the success of the digital models, those control objects were painted before photo acquisition.

Control objects were photographed under natural light condition at 360° around the objects and at different angulations (heights) to produce point clouds with almost constant density in any direction. The camera used was an entry level Canon EOS 1100D with EF-S 18 - 55mm lens and 12.2 Mpixels. It was necessary to use a tripod to hold the camera in order to use higher f/stops (which coincide to smaller apertures and longer acquisition time) that helps to sharpen the background increasing the depth of field. Low ISOs are also suggested to increase exposure time. Scaling was defined by photographing these control objects over a piece of graph paper (Figure 34) or a cutting mat where distances between markers set in the virtual environment were easily obtained through the grid. The same task could be done using further objects of known size.

Precise height dimensions of asperities were gauged using a digital electronic calliper with 0.001mm resolution (±0.005 accuracy). Those dimensional values, obtained by subtraction between highs and lows, were compared with those measured in the digital models after scaling. Discrepancies were found in the order of 10^{-2} mm (Table 1), which it seems such an amazing result, although minor unrealistic geometries where sometimes observed along the vertical and sharp walls of the asperities. These

model deformations are likely linked to the unnatural monotone colour of the control objects that, in turn, has complicated pixels matching.

	Measured roughness (mm)	dev.st	Calculated roughness (mm)	dev.st	Difference (µm)
Tester 1	2.025	0.026	2.097	0.031	72
Tester 2	2.109	0.062	2.115	0.030	6
Tester 3	1.042	0.033	1.059	0.044	17
Tester 4	0.450	0.021	0.418	0.048	32

Table 1. Comparison between roughness measured with a caliper and roughness measured in OpenPlot. Further explanations are in text.

3.2.4 Modeling a real fault surface

A set of carbonate fault samples (courtesy of the Rock Mechanics Laboratory in the Earth Sciences Department at Durham University) belonging to the Central Apennines Downfaulted Area (CADA, Ghisetti and Vezzani, 1999), were photographed proceeding similarly as described in the previous subchapter. The CADA is characterized by active normal faulting since the Late Pliocene/Early Pleistocene (Bosi and Messina, 1991), which is superimposed over the contractional edifice of the Apennine fold and thrust belt (Bigi et al., 1989) and is comprised of the Upper Jurassic-Lower Cretaceous platform carbonates of the Lazio-Abruzzi tectonic unit. All samples were collected from the main fault surfaces of these active normal faults that are characterized by a cataclastic matrix and both striated and polished (mirror-like) fault surfaces.

When a surface is imported in Matlab for the Fast Fourier analysis, the first step is to define a sampling rate through the variable "samp", into the `INTERPOL.M` (Appendix 2) function. Given a certain point cloud surface, "samp" is calculated as $2\sqrt{\frac{area}{n° \, of \, points}}$ and updated in `INTERPOL.M`.

As an example, the striated surface in Figure 35A is composed of 1,575,762 points over an about 0.0029m^2 surface. For this surface, samp is 0.000085m. This means that the mean distance between adjacent points was 43µm.

The succeeding step is the determination of the variable "r_deg" in `ROTATION.M` (Appendix 1), which defines the rotation angle around the $\hat{z}$ axis and helps to reorient $\hat{x}$ or $\hat{y}$ parallel to the slip direction. This task, together with the determination of the variable "bor" in `INTERPOL.M`

(Appendix 2) may need a few iterations. When interpolation is satisfactory, it is then time to start the FFT analysis through the functions `positiveFFTx.M` (Appendix 3) and `positiveFFTy.M` (Appendix 4).

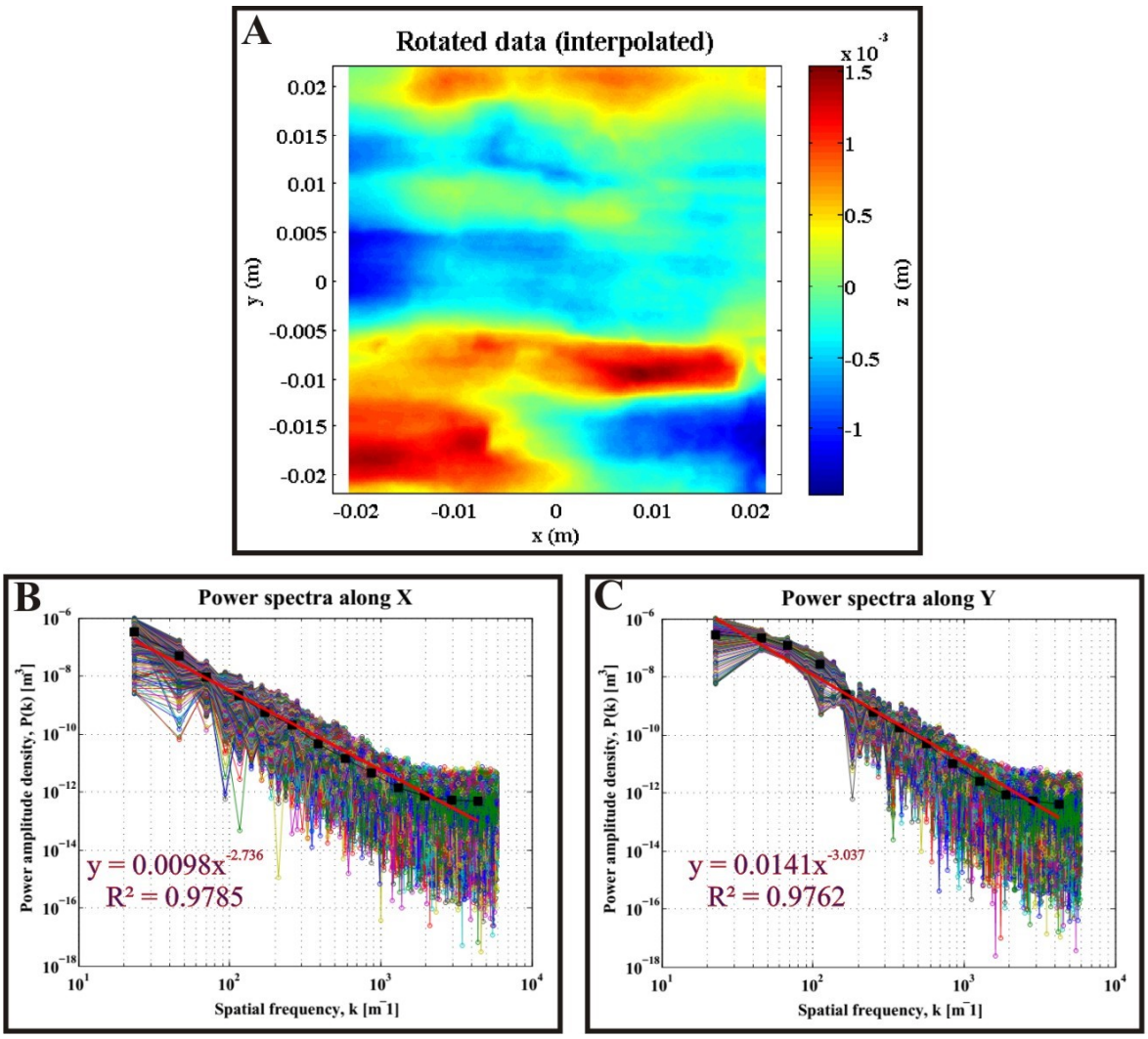

Figure 35. (A) Striated surface rotated and interpolated, and power spectra along X (B) (along slip) and along Y (C) (perpendicular to slip).

The function `positiveFFTx.M` returns the power spectra along X (Figure 35B); this is the superposition of each power spectrum of the signals extracted from rows (that in the case of Figure 35 means the along slip direction). The whole along X Fourier spectrum is computed averaging individual profiles with regularly spaced wave numbers (black dots in Figure 35B) and interpolated. The output of the interpolation are displayed in the

Matlab main window as the linear $y = p_1 \times x + p_2$ interpolation of Logs values. The p_1 and p_2 are then related to the power interpolation by a basic logarithm property as $P(k) = 10^{p_2} \times x^{p_1}$. This step is necessary in Matlab since when fitting a power law to the original data, for example using $f = fit(x, y, 'a \times x\text{^}b')$ ('power1' in Matlab), the fitting is not optimized and leads to inexact and unacceptable results. As an example compare Figure 36 with Figure 35C.

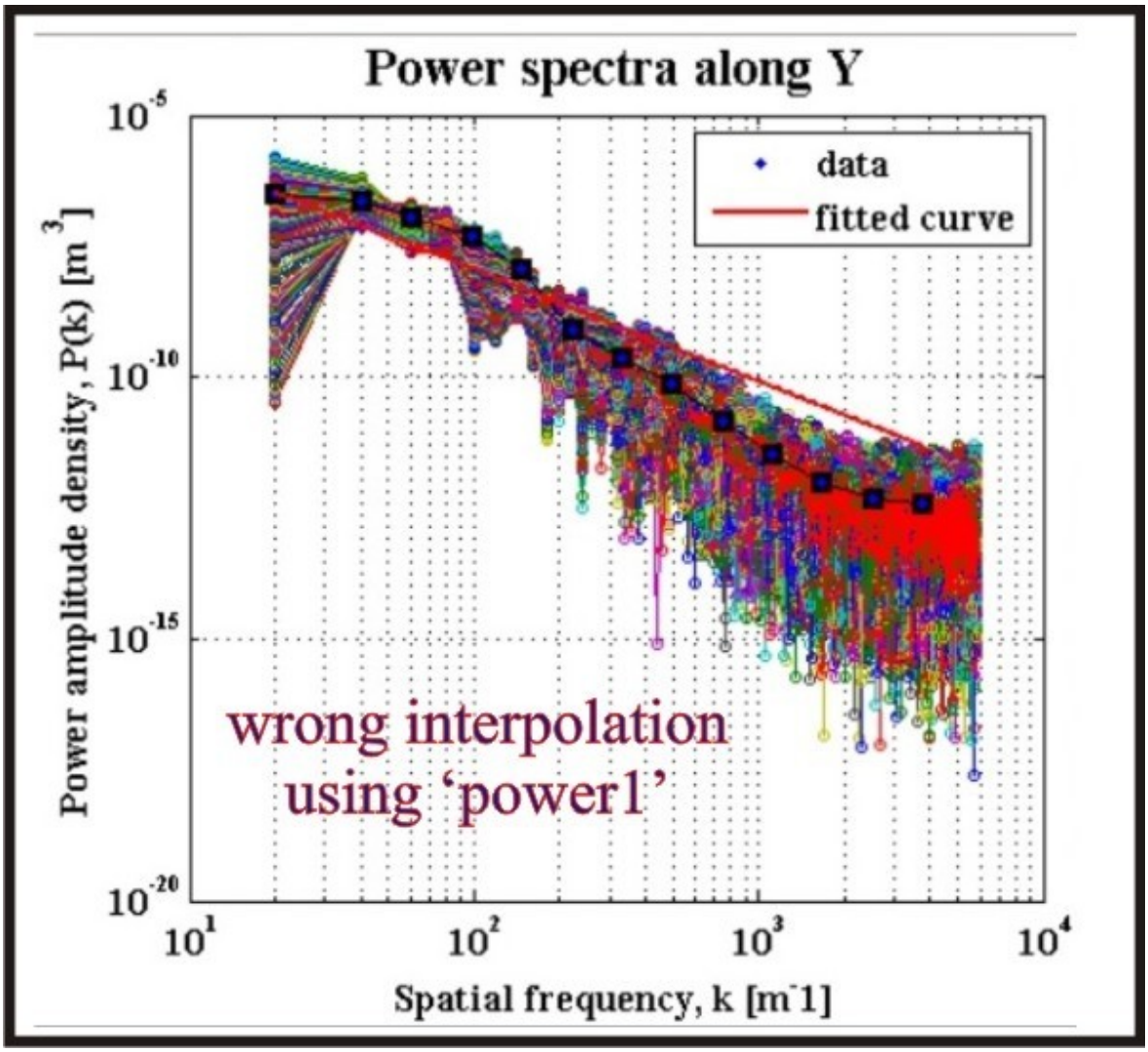

Figure 36. Example of an unacceptable interpolation using 'power1' fit in Matlab, to compare with Figure 35C. R^2 here is 0.7501.

A correct interpolation is the most important step of the workflow since the whole self-affinity is estimated through the relation $P(k) = ak^{-1-2H}$,

where H is the Hurst exponent and a the pre-factor. Hence H is equal to $\frac{p_1+1}{-2}$ and $a = 10^{p_2}$.

A total of 6 fault surfaces belonging to the CADA were analysed and the resulting averaged profiles plotted over the summary graph of Candela et al. (2012) (Figure 37). As shown in Figure 37, the results obtained with the photogrammetric method (this work), are consistent with those obtained by Candela et al. (2012) using laser scanners, laser profilometers and white light interferometers. The main discrepancy with Candela et al. (2012) is in the mean values of the Hurst exponents they report, that are 0.58±0.04 and 0.81±0.1 along and perpendicular to the slip direction, respectively, while my data suggest mean values of 0.87±0.083 and 0.95±0.076. Nevertheless, the almost perfect fitting of both the along and perpendicular to slip overall trends observed by Candela et al. (2012) highlights that, at least for these scale ranges, advanced users can use photogrammetry as a valid and compelling alternative to standard apparatuses.

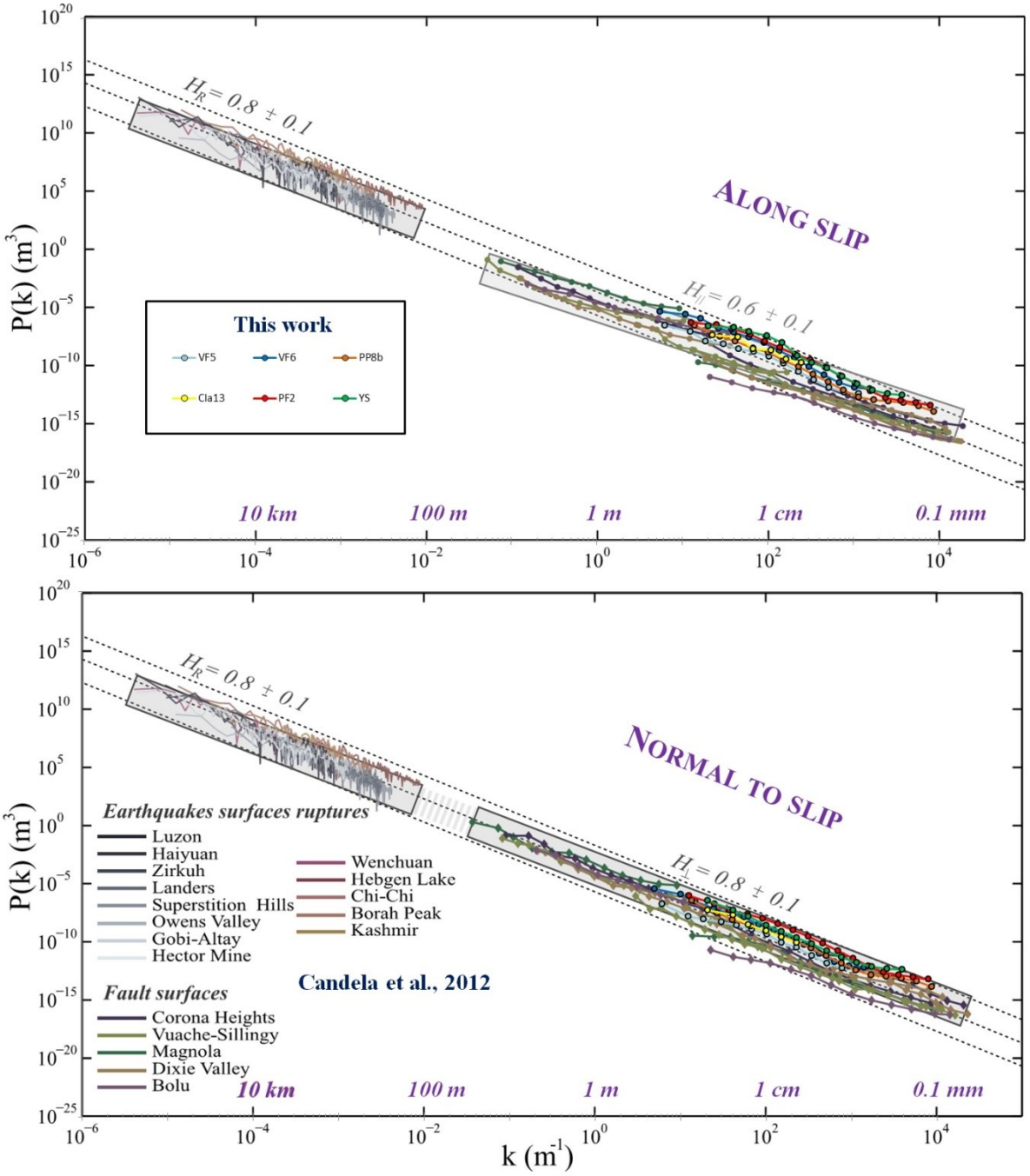

Figure 37. Comparison of results in this thesis with previous works. Candela et al., 2012 (modified).

3.3 STRUCTURAL STUDY OF A RESERVOIR-SCALE INACCESSIBLE OUTCROP: THE CONOCCHIA CLIFF

Spatial and dimensional properties of fractures have been studied for more than forty years (Bonnet et al., 2001 and references therein) with the aim of characterizing geological reservoirs or assessing seismic hazard, among many others. Fractures, which are generally described as narrow or planar discontinuities in displacement and mechanical properties (Fossen, 2010), are brittle structures that, by definition, occur in the upper crust where the internal strength of the rock is overcome by stresses of various origins (e.g. tectonic, overburden, internal pore pressure, thermal expansion or contraction). Fractures can form in opening mode (mode I), such as veins and joints (Pollard and Aydin, 1988), when the displacement occurs, from a flaw in the rock mass (Gross, 1993), along a direction which is perpendicular to the propagation front and to the discontinuity walls. On the contrary, shear-modes fractures, such as faults, are sliding or tearing features where displacement is in-plane with the fracture walls and parallel (mode II) or perpendicular (mode III) to the propagation front, respectively. Moreover, a so called closing mode (mode IV) or anticrack (Fletcher and Pollard, 1981) mode is often employed to define compression fractures such as pressure solution seams.

Important fracture scaling relations have been observed during the years (Leberl et al., 2010; Schultz et al., 2013), for example between joint aperture and length (Olson, 2003; Odonne et al., 2007; Guerriero et al., 2015), host beds thickness and both joint (Narr and Suppe, 1991; Gross, 1993; Gross et al., 1995; Wu and D. Pollard, 1995; Ji and Saruwatari, 1998; Bai and Pollard, 2000; Gillespie et al., 2001; Odonne et al., 2007; Rustichelli et al., 2013) and solution cleavage spacing (Durney and Kisch, 1994; Tavani et al., 2010). In addition, extensive scaling observations have been made on shear fractures, such as fault displacement with length (Cowie and Scholz, 1992; Dawers et al.,

1993; Kim and Sanderson, 2005; Schultz et al., 2008; Tondi et al., 2012) and displacement with fault thickness (Scholz, 2002; Tondi et al., 2006; Childs et al., 2009) among other geometrical properties. Gaining these observations is particularly important in order to make the correct assumptions when populating fracture reservoir models using methods such as DFN (discrete fracture network modelling) (Dershowitz and Einstein, 1988; Cacas et al., 1990; Watanabe and Takahashi, 1995), for the reason that they allow us to simulate the hydraulic properties of the reservoirs (Maffucci et al., 2015). Observations aimed at finding scaling relations, such as those mentioned above, are generally made at the micro/meso scale or, eventually, at the seismic scale and hence, for logistical reasons, from different geological contexts or even from different types of rock. Between these scales, indeed, there is a "gap" of observations that might be bridged by outcrops of tens to hundreds of meters. However, analogues of this size are frequently unapproachable by standard analysis methods (e.g. scan-line and scan area). In fact, in order to be statistically significant, transect lengths should be proportional to the length of the perpendicular fractures that are measured. In other words, since smaller fractures are more abundant than larger fractures, a longer transect is required to sample a representative number of larger fractures (see Bonnet et al., 2001). Accordingly, the sampling of fractures of several meters in length (up to few tens of meters), which are not resolvable through seismic methods, requires longer transects and, hence, extensive outcrops (hundreds of meters wide).

A traditional approach to solve the "gap" issue is represented, for example, by the use of orthorectified photo-panels that, however, has the big disadvantage of forcing into 2D any interpretation of the real 3D nature of the fracture array (Minisini et al., 2014). The most obvious bias to this approach entails that different sets of fractures, at certain angles with the outcrop wall,

are all consider as a single quasi-perpendicular set. A fully 3D approach to this issue has been, however, addressed since late ‘90s through the use of VOMs.

In particular, this work has involved the use of an unmanned aerial vehicle (UAV, (Firpo et al., 2011; Neitzel and Klonowski, 2011; Harwin and Lucieer, 2012; Torres et al., 2012)), here referred to as a drone, equipped with a mirrorless photo-camera. The use of a drone was necessary because the study outcrop, namely the Conocchia cliff (about 250 m-wide and 200 m-high), is inaccessible and exposed toward the Gulf of Positano (southward) (Figure 38) at an altitude over 1100 meters. This meant that there were no suitable places to shoot photographs directly from the field, more so to acquire data by means of field-based LiDAR stations.

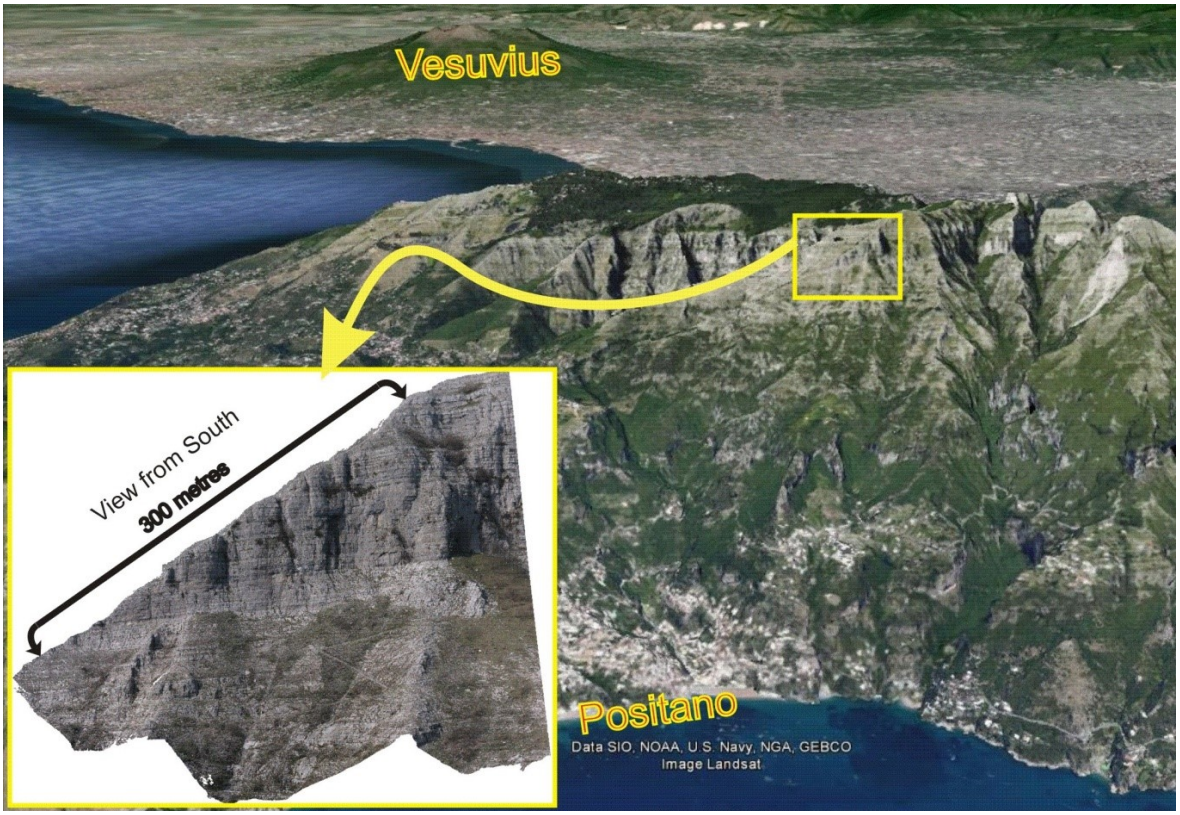

Figure 38. 3D Google Earth view from South of the Sorrento Peninsula with a particular of the Conocchia cliff (inset).

In this work, I present the workflow employed for the structural study of this outcrop, from photographs acquisition up to model managing and data extraction and analysis. The strength of the proposed workflow is that it shows how to gather orthorectified 2D photo-panes along with the 3D spatial orientation of meter and decameter long fractures from an inaccessible outcrop. These derived panels may be employed to solve the fracture scaling relations between the meso- and the seismic scale.

The study cliff (at latitude 40°38'39.5"N and longitude 14°29'44.3"E) is located within the Lattari Mountains in the Sorrento peninsula in the inner sector of the southern Apennine fold and thrust belt. The Lattari Mountains mostly expose rocks of the shallow-water Triassic-Cenozoic carbonate succession of the Apennine platform (Butler et al., 2004). This carbonate platform domain, together with the Apulian carbonate platform to the east and the Lagonegro basin interposed between them, developed on the southern portion of the Mesozoic Adria promontory, on the southern margin of the Neotethys ocean (Mostardini and Merlini, 1986; Iannace et al., 2011), that experienced a multiphase structural evolution related to the development of the Apennine fold and thrust belt. This, from Early Miocene, consists of forebulge and foredeep stages followed by the succeeding inclusion in the tectonic wedge (Mazzoli et al., 2008; Vitale and Ciarcia, 2013). Later, during Pliocene and Pleistocene, this portion of the belt was shaped by the extensional to strike-slip stage associated with the opening of the Tyrrhenian basin (e.g. Malinverno and Ryan, 1986; Casciello et al., 2006).

The Apulian platform hosts the biggest oil and gas reservoirs within Southern Italy (e.g. Tempa Rossa oil-field). However, despite belonging to a different paleo-domain, the Lattari Mountains are represented by very similar rocks to those observed within Southern Italy reservoirs (Mazzoli et al., 2008;

Guerriero et al., 2010, 2011, 2013), having originated in a comparable geologic context (Iannace et al., 2011).

In particular, the outcrop studied in this work is characterized by an alternation of shallow-water limestones and dolomites of Hauterivian-Barremian age pervaded with several, both stratabound and non-stratabound, vertical fractures up to few tens of meters in height, mostly related to the foreland-flexturing and along-foredeep stretching stages in the area (e.g. Tavani, Storti, et al., 2015). Structural studies carried on in this area reveal that, despite the multistage and ling-living deformational sequence of the area, the meso-scale fracture pattern is rather simple. This, in fact, mostly includes fractures and extensional faults developed during the first deformation stage associated with convergence, i.e. these extensional structures mostly developed due to the foreland-flexuring in the peripheral bulge area (e.g. Vitale and Ciarcia, 2013).

3.3.1 The Conocchia 3D VOM

Due to the inaccessibility of the outcrop, photographs were acquired by means of a drone (Figure 39), which was equipped with a mirrorless Sony Nex-7 photo-camera. Sensor sensitivity (i.e. ISO) was set at 800. Time of exposure was 1/4000 seconds with f/8 and the chosen focal length was 24mm (in 35mm format). These settings were kept constant with the purpose of optimizing post-acquisition processing in PhotoScan. 105 overlapping photos (50 Mpixels each) were taken consecutively from different points of view and at different angles with respect to the outcrop (Figure 39) with the intent of prevent data voids (i.e. uncovered areas) within the model. Figure 40 shows one of the 105 photographs with scales measured from the digital model and out-of-target scene masking.

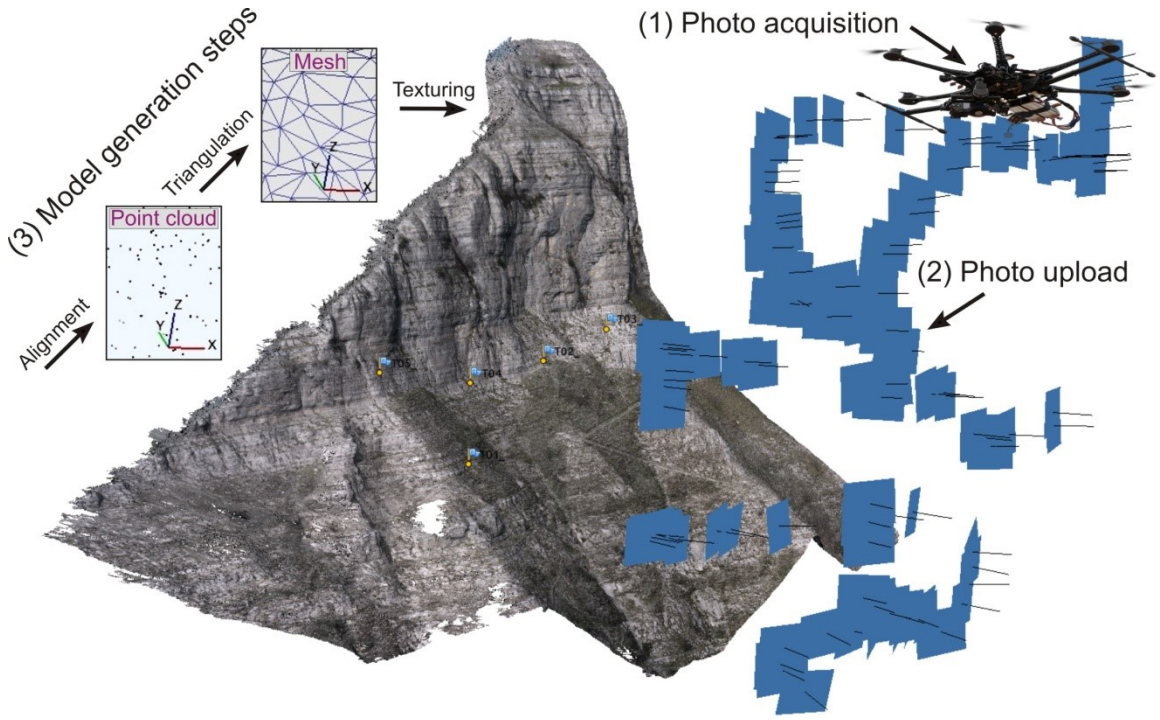

Figure 39. Workflow for the creation of a Virtual Outcrop Model. Photographs were acquired by means of an UAV (1) and later imported in Photoscan (2). The workflow of Photoscan (3) goes through the steps of photo alignment, depth maps reconstruction, building of the geometry and building of the texture.

Due to the extent of the outcrop, coupled with a limited flight range of the drone, a work plan was studied to limit both the number of flights and the time required to conclude the survey. The drone was launched from the base of the cliff in order to start each flight as close as possible to the outcrop wall and batteries were changed as quickly as possible in order to acquire photos with similar lighting condition.

A total-station was used to measure the accurate position of 5 points within the cliff (blue flags in Figure 39). After the generation of the model (Figure 39), these points were used to ensure the post processing scaling and re-orientation of the VOM (e.g. photo-control points in Chandler, 1999).

Figure 40. Low resolution example of one of the 105 photographs with scale and out-of-model masking.

The Conocchia model is a triangular mesh made of about 11.1×10^6 triangular faces and 5.6×10^6 vertices. To facilitate model management, the model was split into eight sub-models that were imported independently into OpenPlot. A model of the entire Conocchia cliff was also generated after point decimation to produce a low-resolution model of the Conocchia, which allows the viewer to visualize it as a whole.

One thousand and three georeferenced fractures and twenty bedding surfaces belonging to the Conocchia model were digitized using the polylines method in OpenPlot. Obviously, more fractures are present along the outcrop but smaller fractures were not analyzed due to texture resolution and because their digitization was beyond the scope of this work, which is the study of larger scale fractures (bigger than few meters).

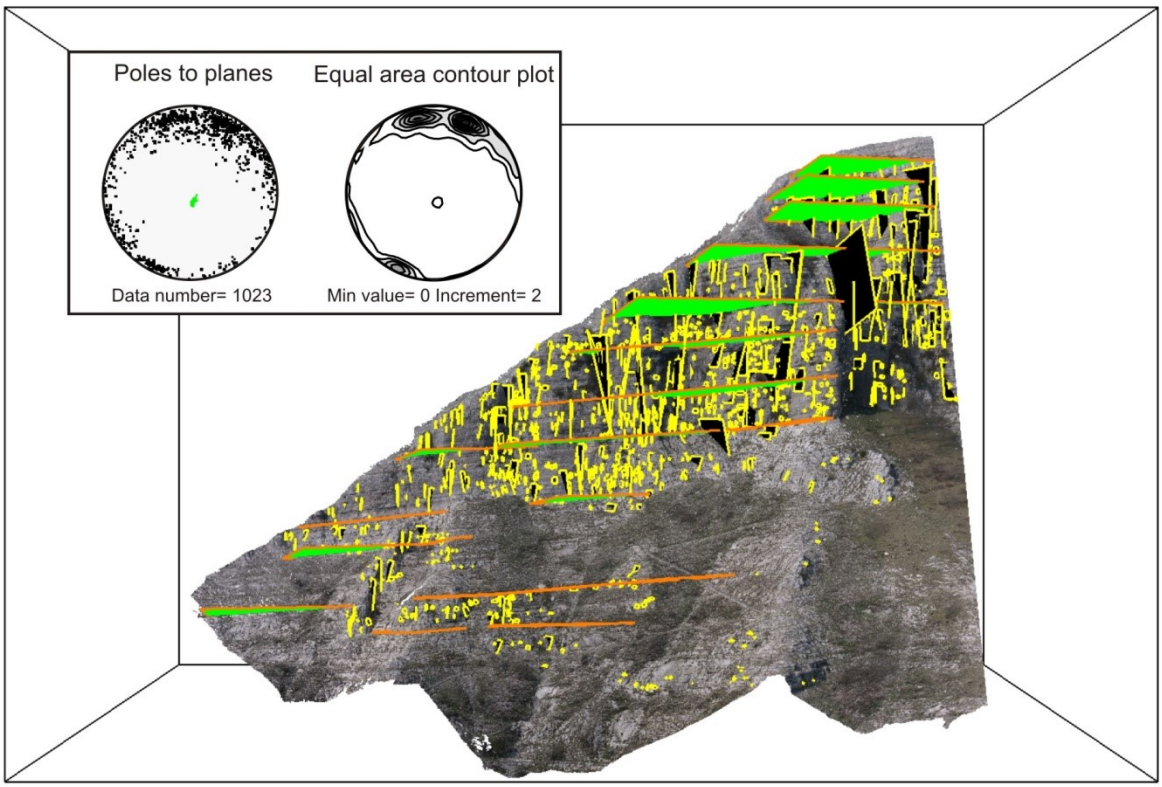

Figure 41. Perspective view from South of the Conocchia VOM with digitized fractures (black rectangles with yellow borders) and bedding surfaces (green rectangles with orange borders).

Figure 41 is a perspective capture from the 3D environment of OpenPlot; it shows the digitized fractures (black rectangles) and a few, visually prominent, digitized bedding surfaces (green rectangles).

In the upper part of the model (non-vegetated vertical cliff) it was possible to digitalize each layer with a single polyline (now best-fit plane), this is the proof of the magnificent lateral continuity of the chosen outcrop and also reveals that there is no macroscopic vertical shear across the fractures. On the contrary within the vegetated area it was not possible to follow each bed laterally but this is simply due to vegetation cover.

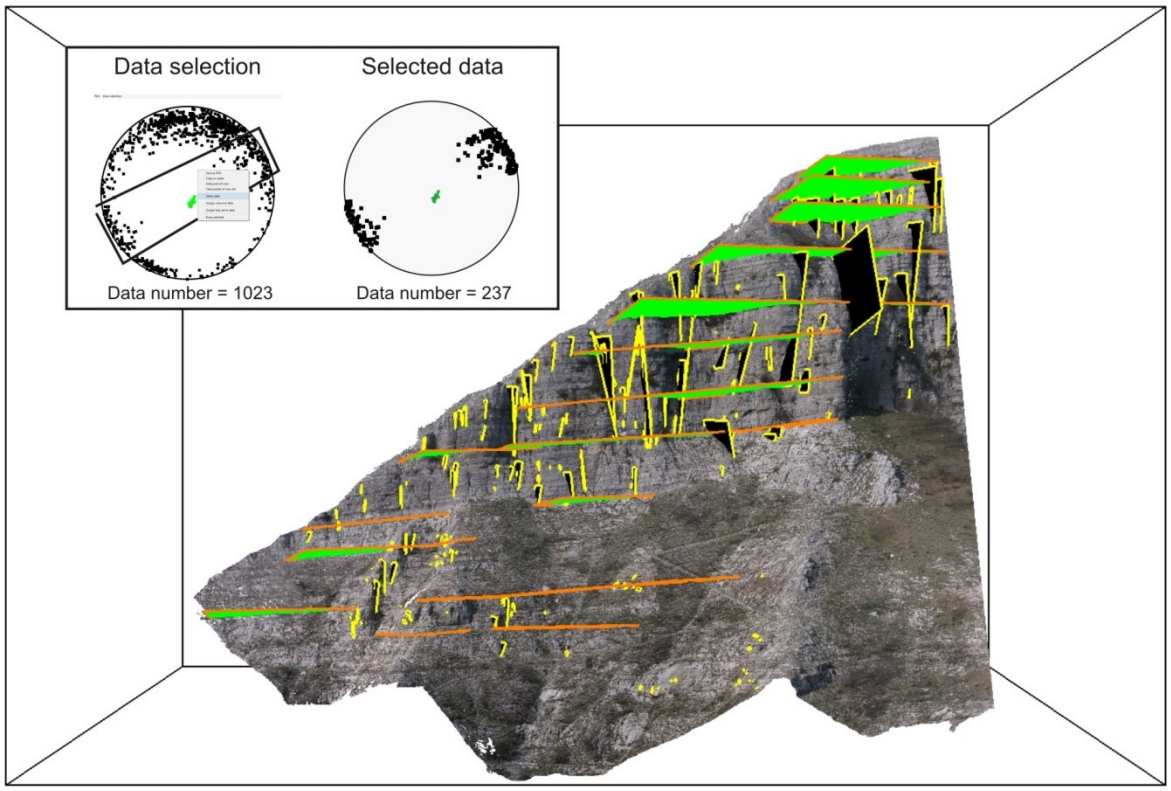

Figure 42. Perspective view from South of the Conocchia VOM after the selection of fractures from the stereonet.

As shown in the plots of Figure 41, poles to bedding (green dots) form a tight cluster around 156/81 (Azimuth/Plunge) which indicates that bedding at the Conocchia cliff is almost horizontal with a gentle plunge towards NW. Poles to fractures are distributed around three clusters (Figure 41, inset). The three sets correspond to fracture planes at high angle to bedding which are oriented almost ENE-WSW (set 1), ESE-WNW (set 2) and NW-SE (set 3).

In OpenPlot, it is possible to select a group of fractures directly from the stereonet (Figure 42, inset), simply by drawing a polygon containing the desired poles inside the stereonet. After selection, each selected group of poles (namely cluster) can be independently visualized in the 3D environment (Figure 42). This procedure allowed us to easily and quickly understanding the orientation of these clusters with respect to the outcrop thus recognizing those fractures properly oriented with respect to the cliff. In particular, fractures in

set 3 are oriented at high angle to the cliff and as a consequence the least affected by biases.

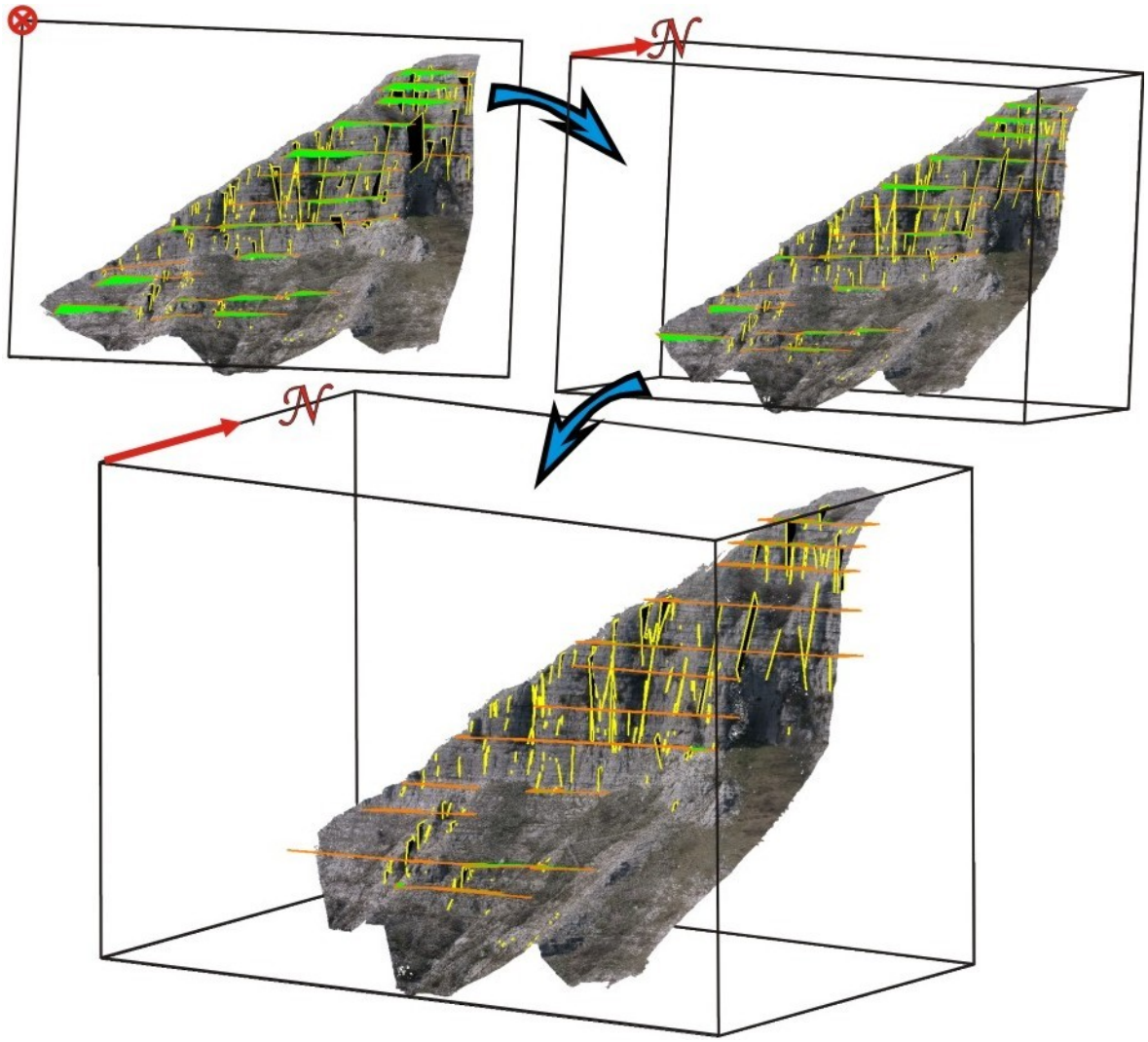

Figure 43. Rotation of the model in orthographic view toward the direction of intersection between set 3 and bedding.

Once a group of fractures is selected, it is also possible to project the selected features (set 3 and bedding in Figure 42) onto a plane which is perpendicular to both. This is equivalent to rotating the model toward the direction of intersection between fractures and bedding while looking in orthographic view (Figure 43). This direction was computed in OpenPlot through a tensorial analysis of the selected cluster (i.e. set 3) and bedding. In

particular, this direction corresponds to the eigenvector associated with the lowest eigenvalue (Figure 44, inset).

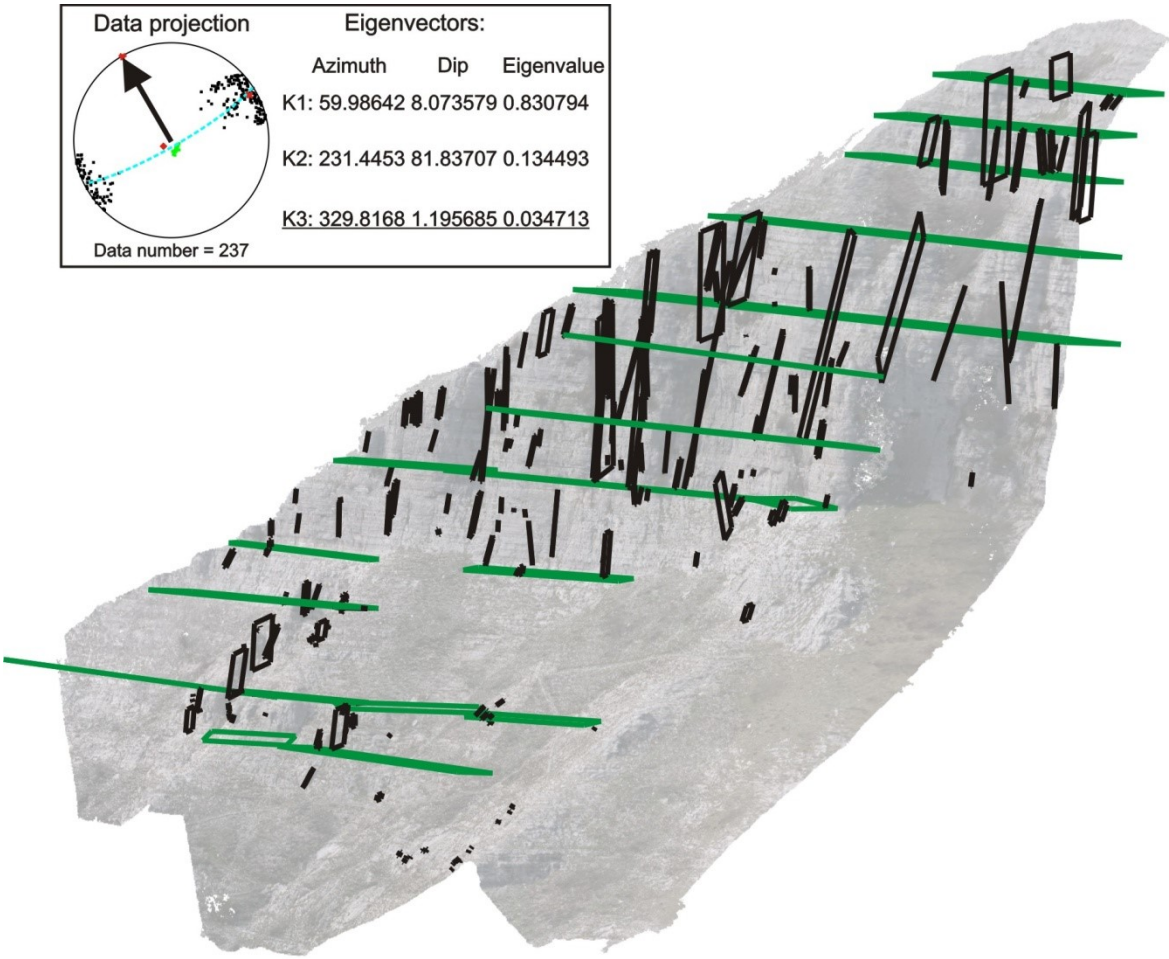

Figure 44. Projected features for Set 3 overlaid over the VOM. Result of the tensorial analysis (inset).

Directly in OpenPlot, the computed direction was assigned to the data and used for projection onto a perpendicular panel (Figure 44). The projected features are saved in *.svg format and hence ready to be opened by any vector drawing software.

Larger projected elements were manually re-digitized using Inkscape (Figure 45a), and a blue colour was assigned to fractures larger than 20 meters. From this perspective it was then possible to identify mechanical boundaries,

which are layers where major fractures arrest on, and hence to schematize mechanical units between them (Figure 45b).

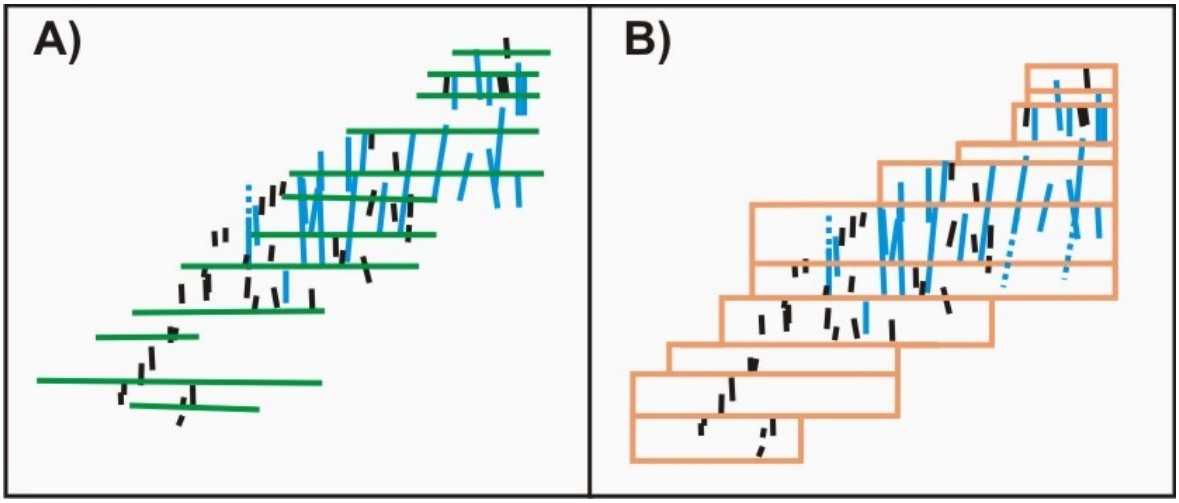

Figure 45. (A) Digitalization of larger projected elements with identification of fractures larger than 20 meters in blue.(B) Identification of the major mechanical boundaries.

From the scheme of Figure 45b it was also possible to construct a synthetic representation of the mechanical stratigraphy of the outcrop for fractures larger than 20 meters belonging to set 3 (Figure 46).

This procedure may be, hence, applied not only to study scaling relations of fractures, but also to mechanical stratigraphy studies if a stratigraphic log of the outcrop is available.

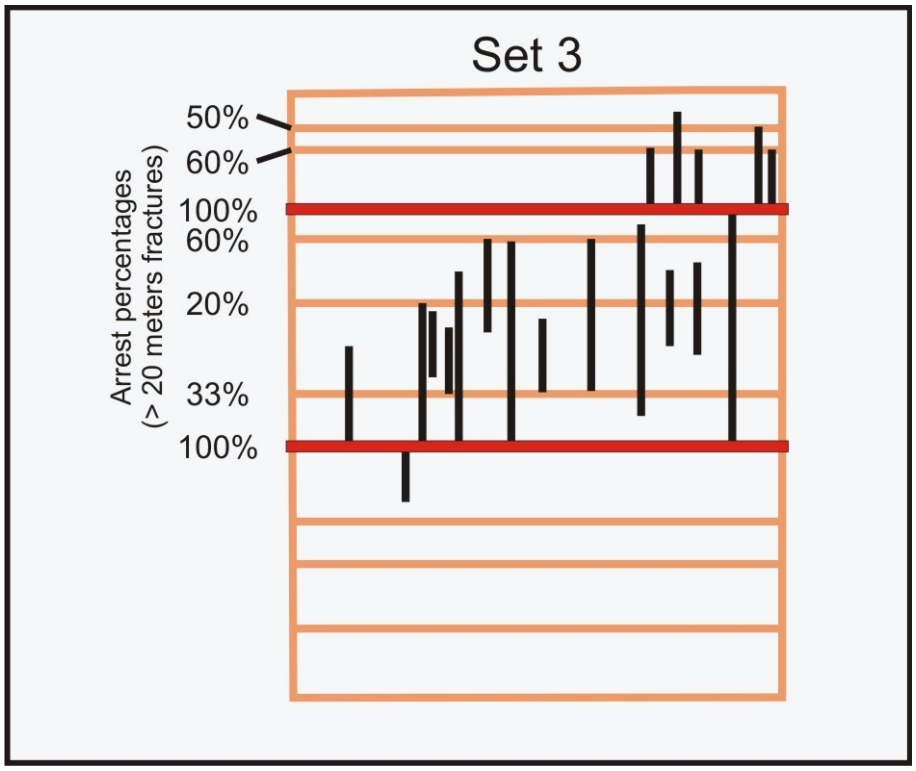

Figure 46. Synthetic representation of the mechanical stratigraphy of the outcrop for set 3 fractures larger than 20 meters.

3.4 REGIONAL SCALE DATA EXTRACTION FROM PHOTOGRAPHS

3.4.1 The Khaviz Anticline case study (Zagros, Iran)

Within the Zagros fold and thrust belt, the Khaviz anticline (Figure 47A), which is NW-SE oriented, is orthogonally cut by a 4 km-long valley constituting a natural cross-section of this anticline. Along this valley, the Miocene Asmari Fm. is continuously exposed along inaccessible vertical cliffs from the forelimb to the backlimb of the anticline (Wennberg et al., 2006), showing an impressive extensional array in the fold's crest (Figure 47C).

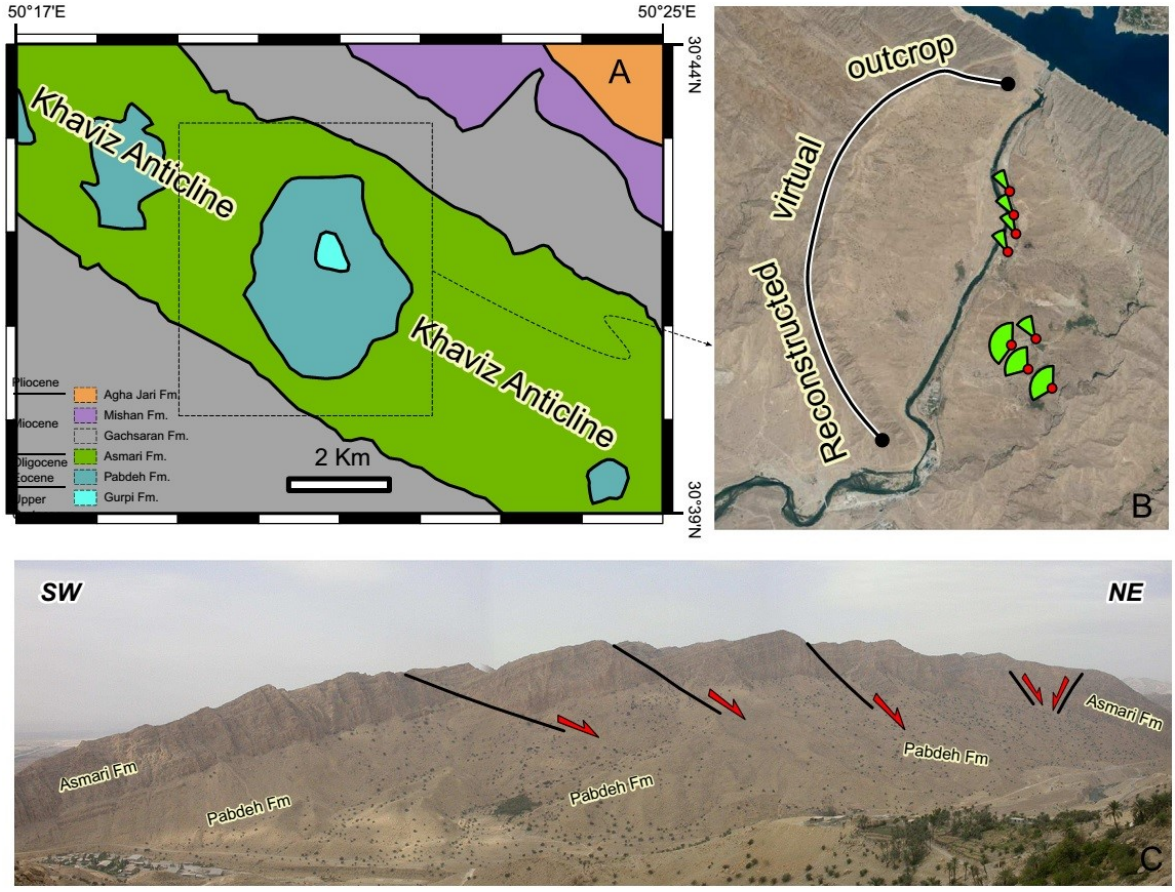

Figure 47. (A) Geological map of the Khaviz Anticline. (B) Google Earth image of the study area, showing the reconstructed cliff and the shooting location of photos used to build the 3D model. (C) Panoramic view of the cliff, with major faults shown. From Tavani, Granado, et al., 2014.

Panoramic photos of this exposure were taken in 2003 (courtesy of Dr. Stefano Tavani) from the positions shown in (Figure 47B). These photos (38 in total with a resolution of 3.8 Mpixels) were taken with a Single Lens Reflex Nikon E4500 camera, without taking into account the possibility of a future 3D reconstruction (Tavani et al., 2014). Furthermore, these photos were taken in two different days under different lighting conditions.

Basically, most of the basic requirements for helping the SFM algorithms were not met in this example, and in fact, at a first stage, the photo-alignment was affected by significant noise (i.e. error), represented by points located up to few hundreds of meters below the ground level (Figure 48A). Through the removal of those photos associated with these unrealistic points, a better point cloud, free of first-order errors, was generated (Figure 48B).

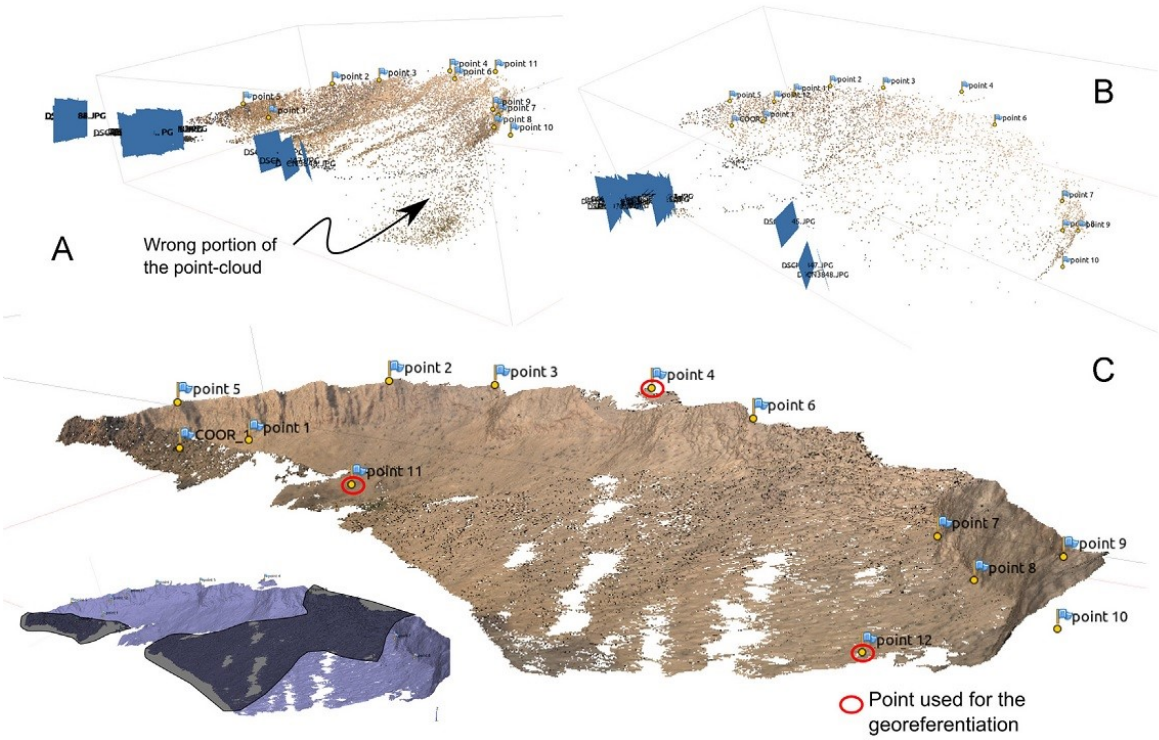

Figure 48. (A) Initial photo-alignment. (B) Improved photo-alignment and point cloud reconstruction. (C) Triangulation, showing markers used for georeferencing and problematic areas. From Tavani, Granado, et al., 2014.

Second-order errors were detected after triangulation of the point cloud, and consisted of small “bubbles”, horizontal peaks and isolated triangles. These errors may indicate a not yet accurate photo alignment or a wrong correlation of points between the different photos. By adding additional markers and removing further problematic photos (10 photos in total were removed) a more accurate point cloud was generated (Figure 48C). Noteworthy, errors still occurred in two areas, as indicated in the inset of Figure 48C, resulting from a portion of the outcrop covered only by three photos, taken in different days, and with different focal lengths.

The model was georeferenced using three non- collinear points located far away from one from each other (Figure 48C). The X and Y coordinates of these points were provided by high-quality image of the area available at Microsoft’s Bing maps, while the Z coordinate was derived using a 1:25.000 topographic map. Such approximate georeferencing may imply a certain degree of error (26 m according to the software estimates), which is however small when compared to the 4 km long model, and indicates a model distortion of less than 1%.

Major faults, together with selected bed surfaces among them, were then extracted from the textured mesh using OpenPlot (Figure 49).

This example has shown that, even in the less ideal conditions (i.e. few Megapixel camera, photos taken in different days, and different focal lengths, among others), it is possible to construct a reliable VOM and extract geological information from it. This task is particularly intriguing if we think about how many old photos from fieldwork we may have in our databases that we could use to reappraise the 3D view of outcrops on the computer screen or to extract/verify geological surface attributes. A further, even more fascinating,

development of this task may result from internet photo collections (Snavely et al., 2006, 2008) and in the possibility of extracting reliable geological data from places that have never been visited.

Figure 49. 3D Outcrop Model of the Khaviz Anticline, in Google Earth environment, together with the extrapolated bedding and fault surfaces. Model available at http://dx.doi.org/10.1016/j.cageo.2013.10.013.

4. DISCUSSIONS

4.1 CONSIDERATIONS BETWEEN PHOTOGRAMMETRY AND LIDAR

Structure from Motion algorithms have been so much developed that, by now, the photogrammetric method can be considered not only as a supplementary tool for LiDAR surveys, but instead as a valid and multipurpose alternative.

In this thesis, although I have not addressed a direct comparison between photogrammetry and LiDAR produced VOMs, I proved that photogrammetry can be employed in geology in several situations and at different scales. Nevertheless, any efforts that would be made to determine which method is more accurate cannot be solved with a sole case study, as a few authors has tried to do, since too many time to time variables are involved with as many sources of error. From this point of view, the general trend of considering LiDAR data superior in term of accuracy, and then to use them to check image matching results, can be an erroneous preconception (Gruen, 2012). Yet, what is the level of accuracy that is needed dealing with VOMs? Of course this depends on the observation scale and goals, and I think that, in all the case studies here presented, I have demonstrated that accurate VOMs can be produced by mean of photogrammetry. In particular, the average error for the models I constructed is between several tens of microns (for the fault surface models) and few meters (for the Khaviz case study), that overall represent an about 2% of error for each model. This suggests that error is scale-independent, since it mainly depends on the resolution of the photographs, while the error threshold depends on goals.

Due to preconceptions or misleading assumptions, probably driven by the still poor efficiency of SfM algorithms at the beginning of this century, photogrammetry has been only recently accepted by the geological community,

while other scientific fields (e.g. architecture, cultural heritage, archeology, topography, forensic sciences, etc.) are a few years ahead.

As I have already said in the introduction, the choice of photogrammetry over LiDAR should be based on the specific outcrop conditions and goals, taking in mind that LiDAR is subjected to less case by case variability (that is to a less amount of variables).

Figure 50 synthesizes the main pros and cons that should be evaluated prior to field investigations. In particular, photogrammetry benefits of a major versatility (e.g. reaching remote areas or using a drone), but accuracy of results cannot be estimated a priori. As shown, photogrammetry needs very little time during the acquisition phase, but can require a long period of, depending on goals and hardware, post processing. Nonetheless, in some respects, time spent in the field may have a higher value in terms of costs and efforts. A shorter acquisition time may be crucial in several situations, for example when the outcrop is situated beside a road.

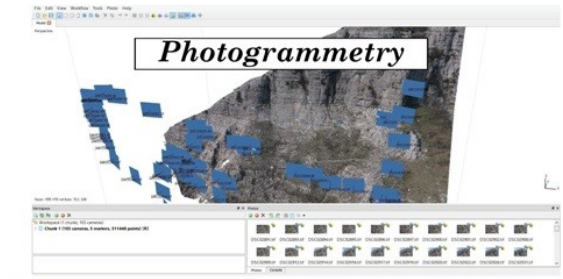

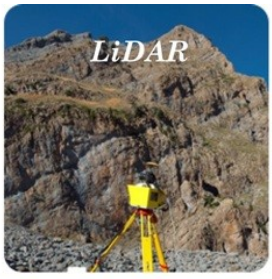

Remote areas can be easily reached	*Bulky and heavy (remote areas are challenges)*
Acquisition time within a few minutes	*Acquisition time within few hours (depending on outcrop size and resolution required)*
Needs much post-acquisition processing (hours-days)	*Needs less time for post-acquisition processing (mostly georeferencing)*
Theoretically improvable endlessly	*Not improvable after acquisition*
Point clouds can be easily triangulated and textured	*Texturing of the polygonal meshes is intricate so working on point clouds is preferred*
Lower costs (Any digital camera works)	*High cost of field equipment*

Figure 50. Schematic representation of pros and cons of photogrammetry and LiDAR.

The issue of texturing, which is an extremely easy task for photogrammetry, is not of minor importance, as has been proved for Rocca di Cave, San Severino Marche and Frontone outcrops.

4.2 CONSIDERATIONS ON VOMS

A Virtual Outcrop Model is not just a supplementary tool to field geology, but it gives the opportunity for taking extensive measurements (i.e. extended area coverage and larger number of measurements), at different scales and even from inaccessible outcrops as for the Conocchia cliff or partly for the San Severino Marche outcrop. Furthermore, data extracted from a georeferenced VOM are themselves georeferenced, so that VOMs allow multiple datasets, that is different types of data, acquired at different times and scales, and using different equipment, to be merged in a single multi-scale model (Jones et al., 2011 and references therein). The advent and availability of VOMs to everybody, will allow in the future, if this is not happening already, the switching from descriptive geology, as it commonly done by conventional studies, to a more quantitative one, which is also multiscale and georeferenced.

An important point to emphasize when dealing with VOMs, as highlighted by Jones et al. (2011) for the LiDAR technique, is that outcrop topography and not geology is reproduced; this is true also for photogrammetry, therefore, even if in most cases surface topography reflects geology, geologists cannot be replaced by technicians for the interpretations of these datasets (Jones et al., 2011). More controversial is the extent to which digital datasets (i.e. data extracted from virtual outcrops) should be supported by field data collected by geologists, i.e. can geologists study virtual outcrops without even visiting the site? My feeling is that gathering a conceptual model,

for example of the fracture pattern and its evolution, during fieldwork is inevitable to discern the fracture nature (i.e. opening mode, filling, slickenlines, etc) by their orientation and also to study abutting and cross-cutting relationships. These features can only be appreciated within the field. Nevertheless a 3D model built by means of photographs always needs some control points to be re-oriented and re-scaled; therefore it is strongly suggested to perform at least a preliminary but qualitative structural analysis of the outcrop during this stage of the workflow when possible. A straightforward usefulness of virtual outcrops is that with a few photographs and some field data it is possible to work quietly sitting on your office chair irrespective of weather conditions, safety concerns and time/money available for fieldwork. Furthermore, the use of 3D models after any campaign can avoid or limit the need for further fieldwork; it is common, in fact, to need to review field data and notes after a field trip. Not of minor importance is the use of virtual outcrops as teaching tools (McCaffrey et al., 2005) for both undergraduates and for the oil industries.

As for any measurement, field measurements are not error free but, on the contrary, particularly prone to it (Jessell et al., 2010). Measurements of any natural surface (e.g. fault, bedding, fracture, contact, etc.) made in the field can be subjected to error in the order of (or greater than) the error produced through a digital model. The issue is that “everything is relative”, therefore nobody knows if field measurements can represent the “real surfaces” better than by means of photogrammetry or LiDAR techniques. This pretentious assertion has never been tested or quantified because the choice of the data used as reference to estimate error and uncertainty is purely subjective.

Even in presence of a perfectly smooth plane, placing a compass in a precisely horizontal position is a quite improbable event (Ragan, 2009).

Therefore in the case of natural irregularities or rough surfaces the error inevitably increases (Groshong, 2006). Error in strike measurement also depends on structure attitude itself with higher error (error > 5°) in low/medium dipping surfaces (Woodcock, 1976). A greater error can occur to a non-expert operator or if the surface to measure is of limited extent (surface area smaller than the size of the compass), weathered or in an inconvenient position. Furthermore, since the strike is measured as an angle from the magnetic north (azimuth), measurements can be affected by magnetic interferences of various origins (e.g. magnetic minerals within the rock, geologist's instruments/accessories, high voltage, etc.). The error can be limited through a statistical approach that is by giving several measures of the same surface and then making the average, however this method would prove to be extremely inopportune and of poor benefit. Instead, a statistical approach is the only possible solution in the case of virtual outcrop. In fact through many computer programs (such as OpenPlot) it is possible to digitalize polylines of geological relevance directly over the textured mesh or the point cloud and a best fit plane is then calculated. In practice, if the geological surface is better represented as a plane and the model is accurate enough, a much more reliable measure (which is also georeferenced) can be obtained, indeed providing a more realistic characterization of discontinuity orientation (e.g. Sturzenegger and Stead, 2009).

One of the most problematic aspects in geology, is the difficulty in sharing the data and the observations made in the field. Furthermore, measurements of geological structures are often not sufficiently representative of the structures themselves, since they are influenced by the operator that, in his experience, takes measurements and decides sampling (e.g. what and how many fractures to measure). With the use of VOMs, these issues can be overlooked since it is possible to associate each measurement to the structures

and share the data. By doing so, a real debate can be opened among geologists, seeing as a direct comparison of various interpretations can be made for each structure. Moreover, a real dialogue can be developed among experts in different topics (e.g. between structural geologists and sedimentologists, earth scientists and engineers, field investigators and reservoir modellers, among many others).

5. CONCLUSIONS

In this work several case studies have been addressed and solved by means of close-range multi view stereo-photogrammetry. Thanks to hardware and software recent improvements, this technique is nowadays able to produce accurate (depending on goals) virtual outcrop models (VOMs). In particular, this technique has properties such as versatility and ease of use that make it more suitable than LiDAR technology in several situations. For instance, the ease with which texturing takes place and the possibility of change the model resolution by changing the distance or the focal length, probably represent the main advantages. In particular, I was able to make models from few centimetres up to hundreds of metres, in order to evaluate the roughness of faults (i.e. asperities at the microscale) as well as the spatial distribution of several metres long fractures. For all these models I tried to evaluate the error; this was found to be about 2-3% in all the models made, pointing out that the error is scale-independent, and related to photos resolution. Moreover, model accuracy can be improved in several ways, which I previously discussed, during post-acquisition processing.

In this work I showed how VOMs can be very effective in solving several issues that are generally encountered during field-work (e.g. inappropriate points of view, inaccessibility of the outcrop, and limited observation scales). Considering the results obtained at different scales, it would be of interest to develop a single multi-scale model, where geological observation made at the different scales can be evaluated as a whole. This, in particular, can have several implications in reservoir characterization or slope stability analysis.

ACKNOWLEDGEMENTS

First, I would like to thank my PhD supervisor, Dr. Stefano Tavani, for continuous support, patience and teaching, but most importantly, for his friendship.

My sincere thanks also go to Dr. Nicola De Paola and Prof. Ken McCaffrey who provided me wider knowledge concerning several aspects of structural geology and remote sensing techniques. Their contribution and mentoring during the time I spent at the Earth Science Department at Durham University (UK), where I was provided full access to research facilities, was crucial for my scientific growth and for my PhD dissertation.

I would also thank Prof. Josep Anton Muñoz, Prof. Pau Arbués and Dr. Pablo Granado, who contributed to my professional growth in different occasions, such as during my short stays at Geomodels Research Institute of the University of Barcelona (Spain) and during a few field works.

Several people, not yet cited, have contributed in different cases. Among them, I wish to thank Dr. Donatella Zappalá (Durham University) for discussions about FFT and my friend Dr. Valentina Magni (Durham University) for introducing me to MatLab and to knitting (shame on me). For their help in several situations during the writing of this thesis and most importantly for their friendship I would also thank Antonio Fulvio Scannapieco (University of Naples), Anna Maria Dichiarante (Durham University), Andrea De Francesco (University of Naples), and Dr. Antonio Agrusta (Imperial College London).

I would also like to thank all my colleagues and all friends that I have not explicitly mentioned. Nevertheless, among them, Leonardo and Lucrezia certainly deserve to be mentioned for their constant presence over the years.

I thank my family for all the support I receive and for never hindering my decisions. A special thank goes to my girlfriend Monia, who firmly believes in me and bears patiently my moody character.

Part of the work was supported by Shell Italia E&P, which I gratefully thank.

APPENDICES

Appendix 1

```
% This Matlab© function rotates a point cloud [xyz] in order to obtain a
% new matrix of point (Xnew) where the z column is normal to the least-
% squares plane i.e. parallel to the direction of the smallest
% eigenvector.

function [Xnew, x0, a, d, normd, R] = rotation(X)
[x0, a, d, normd] = lsplane(X);
Vx = [1 0 0];
Vy = [0 1 0];
Vz = [0 0 1];

if a(3)<0
    a=-a;
end

Vnz = [a(1) a(2) a(3)];
Vnx = cross(Vz,Vnz)/norm(cross(Vz,Vnz));
Vny = cross(Vnz,Vnx)/norm(cross(Vnz,Vnx));
R = [Vnx; Vny; Vnz];

r_deg = 30;

R = [cosd(r_deg) sind(r_deg) 0; -sind(r_deg) cosd(r_deg) 0; 0 0 1]*R;
% The rotation matrix undergoes a further rotation r_deg around z' axis.
% This value is currently set manually in order either to align x' and
% y' axes to x and y axes or to match x' or y' with the slip direction.
% This is necessary because z' is clearly stated by LSPLANE.M whereas x'
% has been defined as the cross product between the rotated plane and the
% original one and y' as the cross product between z' and x'.
% This further rotation could be avoided if the Wahba's problem was
% solved. Namely, it seeks to find a rotation matrix between two
% coordinate systems from a set of vector observations. The solution is
% found by exploiting the Single Value Decomposition Method (for further
% info see Markley F.L. Attitude Determination using Vector Observations
% and the Singular Value Decomposition - 1988). In my case, since only z'
% is clearly defined, there are undefined possible solutions for x' and
% y', and so an univocal solution is defined by this rotation.

m = size(X, 1);

    for i=1:m
        Xnew(:,i) = R*(X(i,:)-x0')';
    end

Xnew = Xnew';
end

function [x0, a, d, normd] = lsplane(X)
% ---------------------------------------------------------------------
% LSPLANE.M   Least-squares plane (orthogonal distance
%             regression).
%
% Version 1.0
% Last amended   I M Smith 27 May 2002.
```

```
% Created        I M Smith 08 Mar 2002
% -------------------------------------------------------------------------
% Input
% X         Array [x y z] where x = vector of x-coordinates,
%           y = vector of y-coordinates and z = vector of
%           z-coordinates.
%           Dimension: m x 3.
%
% Output
% x0        Centroid of the data = point on the best-fit plane.
%           Dimension: 3 x 1.
%
% a         Direction cosines of the normal to the best-fit
%           plane.
%           Dimension: 3 x 1.
%
% <Optional...
% d         Residuals.
%           Dimension: m x 1.
%
% normd     Norm of residual errors.
%           Dimension: 1 x 1.
% ...>
%
% [x0, a <, d, normd >] = lsplane(X)
% -------------------------------------------------------------------------

% check number of data points
  m = size(X, 1);
  if m < 3
    error('At least 3 data points required: ' )
  end
%
% calculate centroid
  x0 = mean(X)';
%
% form matrix A of translated points
  A = [(X(:, 1) - x0(1)) (X(:, 2) - x0(2)) (X(:, 3) - x0(3))];
%
% calculate the SVD of A
  [U, S, V] = svd(A, 0);
  size(U)
  size(S)
  size(V)
%
% find the smallest singular value in S and extract from V the
% corresponding right singular vector
  [s, i] = min(diag(S));
  a = V(:, i);
%
% calculate residual distances, if required
  if nargout > 2
    d = U(:, i)*s;
    normd = norm(d);
  end
% -------------------------------------------------------------------------
% End of LSPLANE.M.
  end
```

Appendix 2

```
% This function creates a regularly spaced interpolated grid of the z
% values. Please define an appropriate value for spacing in "samp" (this
% will affect the sampling rate of the FFT). Please define a value
% different from 0 in "bor" to exclude matrix edges.
% Xq is the resampled vector along x;
% Yq is the resampled vector along y;
% XX and YY define the resampled grid;
% F is the interpolant function;
% qz is the corresponding interpolated z values.
function [F, XX, YY, Xq, Yq, qz, samp]=interpol(xyn, zn)
% Two vectors are created from the matrix 'xy' with regular sampling rate.
samp = 0.0003855; % please define here a proper value for sampling rate
Xq = min(xyn(:,1)):samp:max(xyn(:,1));
Yq = min(xyn(:,2)):samp:max(xyn(:,2));
%% Wrong interpolations result at the edges of the matrix if rotated x
% and y axes do not meet with the unrotated x and y. Increase the value in
% "bor" if artifacts are observed in figure 1 or eventually define a
% different rotation angle in "r_deg" if plausible.
bor = 800; % please set a proper value to cut matrix edges
[Xqmin, Xqmax] = size(Xq);
Xqmin = Xqmin + bor;
Xqmax = Xqmax - bor;
[Yqmin, Yqmax] = size(Yq);
Yqmin = Yqmin + bor;
Yqmax = Yqmax - bor;
Xq = Xq(Xqmin:Xqmax);
Yq = Yq(Yqmin:Yqmax);
clear bor Xqmin Xqmax Yqmin Yqmax;
%% Produce a full grid from the regularly spaced vectors then interpol
[XX, YY] = meshgrid(Xq,Yq);
F = scatteredInterpolant(xyn(:,1),xyn(:,2),zn);
qz = F(XX,YY);
%% to plot interpolated data in 2D
figure(10), pcolor(XX,YY,qz),shading flat;
set (10, 'Color',[1 1 1],'name','Rotated data (interpolated)');
set(gca,'fontweight','bold','fontsize',12,'fontname','Times New Roman');
    title('Rotated data (interpolated)', 'FontWeight','bold',...
        'FontSize',16,'FontName','Times New Roman')
    xlabel('x (m)', 'FontWeight','bold','FontSize',12,...
        'FontName','Times New Roman')
    ylabel('y (m)', 'FontWeight','bold','FontSize',12,...
        'FontName','Times New Roman')
set (get(colorbar('EastOutside'),'ylabel'),'string','z (m)',...
    'FontWeight','bold','FontSize',12,'FontName','Times New Roman');
axis equal;
% xlim([min(Xq) max(Xq)]);
% ylim([min(Yq) max(Yq)]);
%% enable to export the new x,y,z point cloud
%xxx = XX(:);
%yyy = YY(:);
%zzz = qz(:);
%newpoints = [xxx, yyy, zzz];
%dlmwrite('exported.txt', newpoints, 'delimiter', ',', 'newline' , 'pc');
```

Appendix 3

```
% This function performs the FFT analysis through the direction defined by
% x (at each loop a now row in qz is analyzed). At the end of the loop,
% all power spectra are plotted in figure 2 together with the average
power
% spectrum obtained by averaging in a geometric progression (with the
% exception of the first 3 values which are simply the mean at the
% respective points). Red line is the power law fitted curve. Output of
the
% fit are showed in the main Matlab window.
% x is the signal that is to be transformed.
function [Xy, freqx, absXsqall, absmeanx, progmeanx, xprogmean]...
    =positiveFFTx(qz,samp)
Fs=1/samp;  %sampling rate, sampling frequency.
Nx=length(qz(1,:));  %sample lenght.
kx=0:Nx-1;  %create a vector from 0 to N-1.
Tx=Nx/Fs;   %get the frequency interval.
freqx=kx/Tx;    %create the frequency range.
winx=hann(Nx);  %generate a Hann window of length N samples, returns the
                % N-point symmetric Hann window in a column vector.
%% FFT Loop
for indx=1:length(qz(:,1))
% x = qz(indx,:);   %extract the signal to analyze.
x = qz(indx,:); %extract the signal to analyze.
xw = winx(:).*x(:); %use the Hann window to weight or window the data.
%takes the FFT of the signal, and adjusts the amplitude accordingly.
Xy=fft(xw)/Nx;  %Take the magnitude of fft of x and scale the fft so that
                %it is not a function of the length of x.
cutOff = ceil(Nx/2);    %only want the first half of the FFT, since it is
                        %redundant, calculate the number of unique points.
%Take only the first half of the spectrum (FFT is symmetric, throw away
%second half).
Xy = Xy(1:cutOff);      %first half of the spectrum
freqx = freqx(1:cutOff);    %this is an evenly spaced frequency vector
                            %with cutOff points.
% Since we dropped half the FFT, we multiply Xy by 2 to keep the same
% energy.
% The DC component and Nyquist component, if it exists, are unique and
% should not be multiplied by 2.
absX=abs(Xy);
if rem(Nx, 2) % odd N excludes Nyquist point
  absX(2:end) = absX(2:end)*2;
else
  absX(2:end -1) = absX(2:end -1)*2;
end
absX=absX*2;   %Apply HANN Window Amplitude Correction Factor (ACF)
absXsq=((absX.^2)); %furier power spectral density sensu Schuster (1898)
% absXsq=((absX.^2)./(Nx*samp));   %normalized
if indx==1
    absXsqall=zeros(length(absXsq),length(qz(1,:)));%preallocating matrix
    absXsqall(:,1)=absXsq(:);                       %to save memory
else
    absXsqall(:,indx)=absXsq(:);
end
end
indx %visualize number of iterations
%% This section has been devolopped to average the data in a geometric
% progression and hence to plot the results of power interpolation.
clear logfreqx absXsqall2 progmean strep xi yi t
absmeanx=mean(absXsqall,2); %mean of the furier power spectral density of
```

```
                            %all profiles.
for ii=5:length(freqx)
logfreqx((ii-4))=log10(freqx(ii));
absXsqall2((ii-4),:)=absXsqall(ii,:);
end
for conta2=1:3  %Cuts away the first value (null in freqx and exclude the
                %succeding 3 columns from progression.
progmeanx(conta2,1)=freqx(conta2 + 1);
progmeanx(conta2,2)=absmeanx(conta2 + 1);
end
strep=(log10(progmeanx(conta2,1))-log10(progmeanx((conta2 -1),1)));
for t=min(logfreqx(:)):strep:max(logfreqx(:))
    conta2 = conta2 + 1;
    conta = 0;
    sommx = 0;
    for xi = 1:length(absXsqall2(:,1))
        if (logfreqx(xi))>=t & (logfreqx(xi))<(t+(strep)) &...
                                        (t+(strep))< max(logfreqx(:))
            for yi = 1:length(absXsqall2(1,:))
                conta=conta+1;
                sommx=sommx+absXsqall2(xi,yi);
            end
        end
    end
    sommx=sommx/conta;
    progmeanx(conta2,1)=10^(t+(strep/2));
    progmeanx(conta2,2)=sommx;
end
%% To cut NaN values from geometric progression results
clear xprogmean
conta=0;
conta1=0;
TF=isnan(progmeanx(:,2));
for ii=1:length(progmeanx(:,1))
    if isnan(progmeanx(ii,2))
        conta1=conta1+1;
    else
        conta=conta+1;
        conta1=conta1+1;
        xprogmean(conta,1)=progmeanx(conta1,1);
        xprogmean(conta,2)=progmeanx(conta1,2);
    end
end
%% Fit data
[fitobject,gof,output]=fit(log10(xprogmean(1:end,1)),...
            log10(xprogmean(1:end,2)),'poly1')
cfit(fitobject);
coefx=coeffvalues(fitobject)
Hx=(coefx(1)+1)/(-2)
y1=(10^(coefx(2)))*((min(xprogmean(1:end,1)))^coefx(1));
y2=(10^(coefx(2)))*((max(xprogmean(1:end,1)))^coefx(1));
matx= [(min(xprogmean(1:end,1))) y1;...
      (max(xprogmean(1:end,1))) y2];
%% Fitting of y=ax^b doesn't work!!!
% [fitobject,gof,output]=fit(xprogmean(1:end,1),...
%                       xprogmean(1:end,2),'power1')
% cfit(fitobject);
% gof;
% output;
% coefx=coeffvalues(fitobject)
% Hx=(coefx(2)+1)/(-2)
%% Plot the FPS (P(k)).
```

```
figure(2),plot(freqx,absXsqall,'-o','MarkerSize',3);
set (2, 'Color',[1 1 1],'name','Power spectra along X');
set(gca,'fontweight','bold','fontsize',12,'fontname','Times New Roman');
set(gca,'xscal','log')
set(gca,'yscal','log')
hold on
plot(xprogmean(1:end,1),xprogmean(1:end,2),'ks-','MarkerFaceColor','k');
%plot(freqx,absmeanx,'ks-','MarkerFaceColor','k');%mean of each freqx
% p=plot(fitobject,xprogmean(1:end,1),yprogmean(1:end,2));
% set(p,'LineWidth',2)
plot(matx(:,1),matx(:,2),'r-', 'Linewidth', 2);
grid
title('Power spectra along X', 'FontWeight','bold',...
        'FontSize',16,'FontName','Times New Roman')
xlabel('Spatial frequency, k [m^-1]', 'FontWeight','bold',...
        'FontSize',12,'FontName','Times New Roman')
ylabel('Power amplitude density, P(k) [m^3]', 'FontWeight','bold',...
        'FontSize',12,'FontName','Times New Roman')
hold off;
```

Appendix 4

```
% This function performs the FFT analysis through the direction defined by
% y (at each loop a now column in qz is analyzed). At the end of the loop,
% all power spectra are plotted in figure 3 together with the average
power
% spectrum obtained by averaging in a geometric progression (with the
% exception of the first 3 values which are simply the mean at the
% respective points). Red line is the power law fitted curve. Output of
the
% fit are showed in the main Matlab window.
% y is the signal that is to be transformed.
function [Yx, freqy, absYsqall, absmeany, progmeany, yprogmean]...
    =positiveFFTy(qz,samp)
Fs=1/samp;  %sampling rate, sampling frequency.
Ny=length(qz(:,1));  %sample lenght.
ky=0:Ny-1;  %create a vector from 0 to N-1.
Ty=Ny/Fs;   %get the frequency interval.
freqy=ky/Ty;    %create the frequency range.
winy=hann(Ny);  %generate a Hann window of length N samples, returns the
                % N-point symmetric Hann window in a column vector.
%% FFT Loop
for indy=1:length(qz(1,:))
y = qz(:,indy); %extract the signal to analyze.
yw = winy(:).*y(:); %use the Hann window to weight or window the data.
%takes the FFT of the signal, and adjusts the amplitude accordingly.
Yx=fft(yw)/Ny;  %Take the magnitude of FFT of y and scale the FFT so that
                %it is not a function of the length of y.
cutOff = ceil(Ny/2);    %only want the first half of the FFT, since it is
                        %redundant, calculate the number of unique points.
%Take only the first half of the spectrum (FFT is symmetric, throw away
%second half).
Yx = Yx(1:cutOff);      %first half of the spectrum
freqy = freqy(1:cutOff);    %this is an evenly spaced frequency vector
                            %with cutOff points.
% Since we dropped half the FFT, we multiply Yx by 2 to keep the same
% energy.
% The DC component and Nyquist component, if it exists, are unique and
% should not be multiplied by 2.
absY=abs(Yx);
if rem(Ny, 2) % odd N excludes Nyquist point
  absY(2:end) = absY(2:end)*2;
else
  absY(2:end -1) = absY(2:end -1)*2;
end
absY=absY*2;    %Apply HANN Window Amplitude Correction Factor (ACF)
absYsq=((absY.^2)); %furier power spectral density sensu Schuster, 1898
% absYsq=((absY.^2)./(Ny*samp));    %normalized
if indy==1
    absYsqall=zeros(length(absYsq),length(qz(:,1))); %preallocating matrix
    absYsqall(:,1)=absYsq(:);                        %to save memory.
else
    absYsqall(:,indy)=absYsq(:);
end
end
indy %visualize number of iterations
%% This section has been devolopped to average the data in a geometric
% progression and hence to plot the results of power interpolation.
clear logfreqy absYsqall2 progmean strep xi yi t
absmeany=mean(absYsqall,2); %mean of the furier power spectral density of
                            %all profiles.
```

```
for ii=5:length(freqy)
logfreqy((ii-4))=log10(freqy(ii));
absYsqall2((ii-4),:)=absYsqall(ii,:);
end
for conta2=1:3  %Cuts away the first value (null in freqy and exclude the
                %succeding 3 columns from progression.
progmeany(conta2,1)=freqy(conta2 + 1);
progmeany(conta2,2)=absmeany(conta2 + 1);
end
strep=(log10(progmeany(conta2,1))-log10(progmeany((conta2 -1),1)));
for t=min(logfreqy(:)):strep:max(logfreqy(:))
    conta2 = conta2 + 1;
    conta = 0;
    sommy = 0;
    for xi = 1:length(absYsqall2(:,1))
        if (logfreqy(xi))>=t & (logfreqy(xi))<(t+(strep)) &...
                                        (t+(strep))< max(logfreqy(:))
            for yi = 1:length(absYsqall2(1,:))
                conta=conta+1;
                sommy=sommy+absYsqall2(xi,yi);
            end
        end
    end
    sommy=sommy/conta;
    progmeany(conta2,1)=10^(t+(strep/2));
    progmeany(conta2,2)=sommy;
end
%% To cut NaN values from geometric progression results
clear yprogmean
conta=0;
conta1=0;
TF=isnan(progmeany(:,2));
for ii=1:length(progmeany(:,1))
    if isnan(progmeany(ii,2))
        conta1=conta1+1;
    else
        conta=conta+1;
        conta1=conta1+1;
        yprogmean(conta,1)=progmeany(conta1,1);
        yprogmean(conta,2)=progmeany(conta1,2);
    end
end
%% Fit data
[fitobject,gof,output]=fit(log10(yprogmean(1:end,1)),...
            log10(yprogmean(1:end,2)),'poly1')
cfit(fitobject);
coefy=coeffvalues(fitobject)
Hy=(coefy(1)+1)/(-2)
y1=(10^(coefy(2)))*((min(yprogmean(1:end,1)))^coefy(1));
y2=(10^(coefy(2)))*((max(yprogmean(1:end,1)))^coefy(1));
maty= [(min(yprogmean(1:end,1))) y1;...
      (max(yprogmean(1:end,1))) y2];
%% Fitting of y=ax^b doesn't work!!!
% [fitobject,gof,output]=fit(yprogmean(1:end,1),...
%                       yprogmean(1:end,2),'power1')
% cfit(fitobject);
% gof;
% output;
% coefy=coeffvalues(fitobject)
% Hy=(coefy(2)+1)/(-2)
%% Plot the FPS (P(k)).
figure(3),plot(freqy,absYsqall,'-o','MarkerSize',3);
```

```
set (3, 'Color',[1 1 1],'name','Power spectra along Y');
set(gca,'fontweight','bold','fontsize',12,'fontname','Times New Roman');
set(gca,'xscal','log')
set(gca,'yscal','log')
hold on
plot(yprogmean(1:end,1),yprogmean(1:end,2),'ks-','MarkerFaceColor','k');
%plot(freqy,absmeany,'ks-','MarkerFaceColor','k');%mean of each freqy
% p=plot(fitobject,yprogmean(1:end,1),yprogmean(1:end,2));
% set(p,'LineWidth',2)
plot(maty(:,1),maty(:,2),'r-', 'LineWidth', 2);
grid
 title('Power spectra along Y', 'FontWeight','bold',...
        'FontSize',16,'FontName','Times New Roman')
 xlabel('Spatial frequency, k [m^-1]', 'FontWeight','bold',...
        'FontSize',12,'FontName','Times New Roman')
 ylabel('Power amplitude density, P(k) [m^3]', 'FontWeight','bold',...
        'FontSize',12,'FontName','Times New Roman')
hold off
```

REFERENCES

Alvarez, W., T. Engelder, and P. A. Geiser, 1978, Classification of solution cleavage in pelagic limestones: Geology, v. 6, no. 5, p. 263–266, doi:10.1130/0091-7613(1978)6.

Arbués, P., D. García-Sellés, P. Granado, M. López-Blanco, and J. A. Muñoz, 2012, A Method for Producing Photorealistic Digital Outcrop Models, *in* 74th EAGE Conference & Exhibition.

Bai, T., and D. D. Pollard, 2000, Fracture spacing in layered rocks: a new explanation based on the stress transition: Journal of Structural Geology, v. 22, no. 1, p. 43–57, doi:10.1016/S0191-8141(99)00137-6.

Barchi, M., F. Brozzetti, and G. Lavecchia, 1991, Analisi strutturale e geometrica dei bacini della media Valle del Tevere e della Valle Umbra: Bollettino della Societa Geologica Italiana, v. 110, no. 1, p. 65–76.

Bellian, J. a., C. Kerans, and D. C. Jennette, 2005, Digital Outcrop Models: Applications of Terrestrial Scanning Lidar Technology in Stratigraphic Modeling: Journal of Sedimentary Research, v. 75, no. 2, p. 166–176, doi:10.2110/jsr.2005.013.

Bemis, S. P., S. Micklethwaite, D. Turner, M. R. James, S. Akciz, S. T. Thiele, and H. A. Bangash, 2014, Ground-based and UAV-Based photogrammetry: A multi-scale, high-resolution mapping tool for structural geology and paleoseismology: Journal of Structural Geology, v. 69, p. 163–178, doi:10.1016/j.jsg.2014.10.007.

Bigi, G., D. Cosentino, M. Parlotto, R. Sartori, and P. Scandone, 1989, Structural model of Italy 1:500,000. Progetto Finalizzato Geodinamica: Quaderni della Ricerca Scientifica CNR, no. 114.

Bistacchi, A., W. A. Griffith, S. A. F. Smith, G. Di Toro, R. R. Jones, and S. Nielsen, 2011, Fault Roughness at Seismogenic Depths from LIDAR and Photogrammetric Analysis: Pure and Applied Geophysics, v. 168, no. 12, p. 2345–2363, doi:10.1007/s00024-011-0301-7.

Bonnet, E., O. Bour, N. E. Odling, P. Davy, I. Main, P. A. Cowie, and B. Berkowitz, 2001, Scaling of fracture systems in geological media: Reviews of Geophysics, v. 39, no. 3, p. 347–383.

Bosi, C., and P. Messina, 1991, Ipotesi di correlazione fra successioni morfo-litostratigrafiche plio-pleistoceniche nell'Appennino Laziale-Abruzzese: Studi Geologici Camerti, v. 2, p. 257–263.

Brodsky, E. E., J. J. Gilchrist, A. Sagy, and C. Collettini, 2011, Faults smooth gradually as a function of slip: Earth and Planetary Science Letters, v. 302, no. 1-2, p. 185–193, doi:10.1016/j.epsl.2010.12.010.

Buckley, S. J., H. D. Enge, C. Carlsson, and J. A. Howell, 2010, Terrestrial laser scanning for use in virtual outcrop geology: The Photogrammetric Record, v. 25, no. 131, p. 225–239, doi:10.1111/j.1477-9730.2010.00585.x.

Buckley, S. J., J. A. Howell, H. D. Enge, and T. H. Kurz, 2008, Terrestrial laser scanning in geology: data acquisition, processing and accuracy considerations: Journal of the Geological Society, v. 165, no. 3, p. 625–638, doi:10.1144/0016-76492007-100.

Butler, R. W. H. et al., 2004, Applying thick-skinned tectonic models to the Apennine thrust belt of Italy—Limitations and implications, *in* K. R. McClay, ed., Thrust tectonics and hydrocarbon systems: AAPG Memoir 82: AAPG Special Volumes, p. 647–667.

Cacas, M. C., E. Ledoux, G. de Marsily, B. Tillie, A. Barbreau, E. Durand, B. Feuga, and P. Peaudecerf, 1990, Modeling fracture flow with a stochastic discrete fracture network: calibration and validation: 1. The flow model: Water Resources Research, v. 26, no. 3, p. 479–489, doi:10.1029/WR026i003p00479.

Candela, T., F. Renard, M. Bouchon, A. Brouste, D. Marsan, J. Schmittbuhl, and C. Voisin, 2009, Characterization of Fault Roughness at Various Scales: Implications of Three-Dimensional High Resolution Topography Measurements: Pure and Applied Geophysics, v. 166, no. 10-11, p. 1817–1851, doi:10.1007/s00024-009-0521-2.

Candela, T., F. Renard, Y. Klinger, K. Mair, J. Schmittbuhl, and E. E. Brodsky, 2012, Roughness of fault surfaces over nine decades of length scales: Journal of Geophysical Research, v. 117, no. B8, p. B08409, doi:10.1029/2011JB009041.

Casciello, E., M. Cesarano, and G. Pappone, 2006, Extensional detachment faulting on the Tyrrhenian margin of the southern Apennines contractional belt (Italy): Journal of the Geological Society, v. 163, no. 4, p. 617–629, doi:10.1144/0016-764905-054.

Chandler, J., 1999, Effective application of automated digital photogrammetry for geomorphological research: Earth Surface Processes and Landforms, v. 24, no. 1, p. 51–63, doi:10.1002/(SICI)1096-9837(199901)24:1<51::AID-ESP948>3.0.CO;2-H.

Childs, C., T. Manzocchi, J. J. Walsh, C. G. Bonson, A. Nicol, and M. P. J. Schöpfer, 2009, A geometric model of fault zone and fault rock thickness variations: Journal of Structural Geology, v. 31, no. 2, p. 117–127, doi:10.1016/j.jsg.2008.08.009.

Chilovi, C., A. J. De Feyter, G. Minelli, and M. R. Barchi, 2002, Neogene strike-slip reactivation of Jurassic normal faults in the M. Nerone-M.

Catria Anticline (Umbro-Marchean Apennines, Italy): Bollettino della Società geologica italiana, v. 121, no. 1, p. 199–207.

Clegg, P., I. Trinks, and K. J. W. McCaffrey, 2005, Towards the virtual outcrop: Geoscientist, v. 15, no. 1, p. 8–9.

Cowie, P. A., and C. H. Scholz, 1992, Displacement-length scaling relationship for faults: data synthesis and discussion: Journal of Structural Geology, v. 14, no. 10, p. 1149–1156, doi:10.1016/0191-8141(92)90066-6.

Davidesko, G., A. Sagy, and Y. H. Hatzor, 2014, Evolution of slip surface roughness through shear: Geophysical Research Letters, v. 41, no. 5, p. 1492–1498, doi:10.1002/2013GL058913.

Dawers, N. H., M. H. Anders, and C. H. Scholz, 1993, Growth of normal faults: Displacement-length scaling: Geology, v. 21, no. 12, p. 1107, doi:10.1130/0091-7613(1993)021<1107:GONFDL>2.3.CO;2.

Dershowitz, W. S., and H. H. Einstein, 1988, Characterizing rock joint geometry with joint system models: Rock Mechanics and Rock Engineering, v. 21, no. 1, p. 21–51, doi:10.1007/BF01019674.

Dieterich, J. H., 1979, Modeling of Tock Friction 1. Experimental Results and Constitutive Equations: Journal of Geophysical Research, v. 84, no. B5, p. 2161–2168, doi:10.1029/JB084iB05p02161.

Durney, D. W., and H. J. Kisch, 1994, A field classification and intensity sclae for first-generation cleavages: Journal of Australian Geology and Geophysics, v. 15, no. 3, p. 257–295.

Elter, P., G. Giglia, M. Tongiorgi, and L. Trevisan, 1975, Tensional and compressional areas in recent (Tortonian to present) evolution of Northern Apennines: TRANSACTIONS-AMERICAN GEOPHYSICAL UNION, v. 56, no. 3, p. 166–166.

Favalli, M., A. Fornaciai, I. Isola, S. Tarquini, and L. Nannipieri, 2012, Multiview 3D reconstruction in geosciences: Computers & Geosciences, v. 44, p. 168–176, doi:10.1016/j.cageo.2011.09.012.

Fernández, O., S. Jones, N. Armstrong, G. Johnson, A. Ravaglia, and J. A. Muñoz, 2009, Automated tools within workflows for 3D structural construction from surface and subsurface data: GeoInformatica, v. 13, no. 3, p. 291–304, doi:10.1007/s10707-008-0059-y.

Fernández, O., J. A. Muñoz, P. Arbués, O. Falivene, and M. Marzo, 2004, Three-dimensional reconstruction of geological surfaces: An example of growth strata and turbidite systems from the Ainsa basin (Pyrenees, Spain): AAPG Bulletin, v. 88, no. 8, p. 1049–1068.

Firpo, G., R. Salvini, M. Francioni, and P. G. Ranjith, 2011, Use of Digital

Terrestrial Photogrammetry in rocky slope stability analysis by Distinct Elements Numerical Methods: International Journal of Rock Mechanics and Mining Sciences, v. 48, no. 7, p. 1045–1054, doi:10.1016/j.ijrmms.2011.07.007.

Fletcher, R. C., and D. D. Pollard, 1981, Anticrack model for pressure solution surfaces: Geology, v. 9, no. 9, p. 419–424, doi:10.1130/0091-7613(1981)9.

Fossen, H., 2010, Structural geology: New York, Cambridge University Press, 463 p.

Furukawa, Y., B. Curless, S. M. Seitz, and R. Szeliski, 2010, Towards Internet-scale multi-view stereo, *in* 2010 IEEE Computer Society Conference on Computer Vision and Pattern Recognition: IEEE, p. 1434–1441, doi:10.1109/CVPR.2010.5539802.

Furukawa, Y., and J. Ponce, 2010, Accurate, dense, and robust multiview stereopsis: IEEE Transactions on Pattern Analysis and Machine Intelligence, v. 32, no. 8, p. 1362–1376, doi:10.1109/TPAMI.2009.161.

García-Sellés, D., O. Falivene, P. Arbués, O. Gratacos, S. Tavani, and J. A. Muñoz, 2011, Supervised identification and reconstruction of near-planar geological surfaces from terrestrial laser scanning: Computers & Geosciences, v. 37, no. 10, p. 1584–1594, doi:10.1016/j.cageo.2011.03.007.

Geiser, P. A., 1988, Mechanisms of thrust propagation: some examples and implications for the analysis of overthrust terranes: Journal of Structural Geology, v. 10, no. 8, p. 829–845, doi:10.1016/0191-8141(88)90098-3.

Ghisetti, F., and L. Vezzani, 1999, Depth and modes of Pliocene-Pleistocene crustal extension of the Apennines (Italy): Terra Nova, v. 11, no. 2-3, p. 67–72, doi:10.1046/j.1365-3121.1999.00227.x.

Gillespie, P. A., J. J. Walsh, J. Watterson, C. G. Bonson, and T. Manzocchi, 2001, Scaling relationships of joint and vein arrays from The Burren, Co. Clare, Ireland: Journal of Structural Geology, v. 23, no. 2-3, p. 183–201, doi:http://dx.doi.org/10.1016/S0191-8141(00)00090-0.

Groshong, R. H. J., 2006, 3-D Structural Geology: A Practical Guide to Quantitative Surface and Subsurface Map Interpretation. Second Edition: Berlin, Heidelberg, Springer, 400 p.

Gross, M. R., 1993, The origin and spacing of cross joints: examples from the Monterey Formation, Santa Barbara Coastline, California: Journal of Structural Geology, v. 15, no. 6, p. 737–751, doi:10.1016/0191-8141(93)90059-J.

Gross, M. R., M. P. Fischer, T. Engelder, and R. J. Greenfield, 1995, Factors controlling joint spacing in interbedded sedimentary rocks: integrating

numerical models with field observations from the Monterey Formation, USA: Geological Society, London, Special Publications, v. 92, no. 1, p. 215–233, doi:10.1144/GSL.SP.1995.092.01.12.

Gruen, A., 2012, Development and Status of Image Matching in Photogrammetry: The Photogrammetric Record, v. 27, no. 137, p. 36–57, doi:10.1111/j.1477-9730.2011.00671.x.

Gruen, A., F. Remondino, and L. Zhang, 2004, Photogrammetric Reconstruction of the Great Buddha of Bamiyan, Afghanistan: The Photogrammetric Record, v. 19, no. 107, p. 177–199, doi:10.1111/j.0031-868X.2004.00278.x.

Guerriero, V., F. Dati, M. Giorgioni, A. Iannace, S. Mazzoli, and S. Vitale, 2015, The role of stratabound fractures for fluid migration pathways and storage in well-bedded carbonates: Italian Journal of Geosciences, v. 134, no. 2, doi:10.3301/IJG.2014.27.

Guerriero, V., A. Iannace, S. Mazzoli, M. Parente, S. Vitale, and M. Giorgioni, 2010, Quantifying uncertainties in multi-scale studies of fractured reservoir analogues: Implemented statistical analysis of scan line data from carbonate rocks: Journal of Structural Geology, v. 32, no. 9, p. 1271–1278, doi:10.1016/j.jsg.2009.04.016.

Guerriero, V., S. Mazzoli, A. Iannace, S. Vitale, A. Carravetta, and C. Strauss, 2013, A permeability model for naturally fractured carbonate reservoirs: Marine and Petroleum Geology, v. 40, p. 115–134, doi:10.1016/j.marpetgeo.2012.11.002.

Guerriero, V., S. Vitale, S. Ciarcia, and S. Mazzoli, 2011, Improved statistical multi-scale analysis of fractured reservoir analogues: Tectonophysics, v. 504, no. 1-4, p. 14–24, doi:10.1016/j.tecto.2011.01.003.

Harwin, S., and A. Lucieer, 2012, Assessing the Accuracy of Georeferenced Point Clouds Produced via Multi-View Stereopsis from Unmanned Aerial Vehicle (UAV) Imagery: Remote Sensing, v. 4, no. 12, p. 1573–1599, doi:10.3390/rs4061573.

Hodgetts, D., 2013, Laser scanning and digital outcrop geology in the petroleum industry: A review: Marine and Petroleum Geology, v. 46, p. 335–354, doi:10.1016/j.marpetgeo.2013.02.014.

Hodgetts, D., N. J. Drinkwater, J. Hodgson, J. Kavanagh, S. S. Flint, K. J. Keogh, and J. A. Howell, 2004, Three-dimensional geological models from outcrop data using digital data collection techniques: an example from the Tanqua Karoo depocentre, South Africa, *in* A. Curtis, and R. Wood, eds., Geological Prior Information: Informing Science and Engineering: Geological Society, London, Special Publications, 239, p. 57–75, doi:10.1144/GSL.SP.2004.239.01.05.

Iannace, A., M. Capuano, and L. Galluccio, 2011, “Dolomites and dolomites” in Mesozoic platform carbonates of the Southern Apennines: Geometric distribution, petrography and geochemistry: Palaeogeography, Palaeoclimatology, Palaeoecology, v. 310, no. 3-4, p. 324–339, doi:10.1016/j.palaeo.2011.07.025.

Jaeger, J. C., N. G. W. Cook, and R. Zimmerman, 2009, Fundamentals of Rock Mechanics: Blackwell, 488 p.

James, M. R., and S. Robson, 2014, Mitigating systematic error in topographic models derived from UAV and ground-based image networks: Earth Surface Processes and Landforms, v. 39, no. 10, p. 1413–1420, doi:10.1002/esp.3609.

James, M. R., and S. Robson, 2012, Straightforward reconstruction of 3D surfaces and topography with a camera: Accuracy and geoscience application: Journal of Geophysical Research, v. 117, no. F3, p. F03017, doi:10.1029/2011JF002289.

Jessell, M. W., L. Ailleres, and E. A. de Kemp, 2010, Towards an integrated inversion of geoscientific data: What price of geology? Tectonophysics, v. 490, no. 3-4, p. 294–306, doi:10.1016/j.tecto.2010.05.020.

Ji, S., and K. Saruwatari, 1998, A revised model for the relationship between joint spacing and layer thickness: Journal of Structural Geology, v. 20, no. 11, p. 1495–1508, doi:10.1016/S0191-8141(98)00042-X.

Jones, R. R., J. K. Pringle, K. J. W. McCaffrey, J. Imber, R. H. Wightman, J. Guo, and J. J. Long, 2011, Extending digital outcrop geology into the subsurface, *in* O. J. Martinsen, A. J. Pulham, P. Haughton, and M. D. Sullivan, eds., CSP010 Outcrops Revitalized: Tools, Techniques and Applications: SEPM (Society for Sedimentary Geology), p. 31–50.

Jones, R. R., T. F. Wawrzyniec, N. S. Holliman, K. J. W. McCaffrey, J. Imber, and R. E. Holdsworth, 2008, Describing the dimensionality of geospatial data in the earth sciences—Recommendations for nomenclature: Geosphere, v. 4, no. 2, p. 354, doi:10.1130/GES00158.1.

Kim, Y.-S., and D. J. Sanderson, 2005, The relationship between displacement and length of faults: a review: Earth-Science Reviews, v. 68, no. 3-4, p. 317–334, doi:10.1016/j.earscirev.2004.06.003.

Leberl, F., A. Irschara, T. Pock, P. Meixner, M. Gruber, S. Scholz, and A. Wiechert, 2010, Point Clouds: Lidar versus 3D Vision: Photogrammetric engineering and remote sensing, v. 76, no. 10, p. 1123–1134.

Lee, J., and R. Bruhn, 1996, Structural anisotropy of normal fault surfaces: Journal of Structural Geology.

Lockner, D. A., and N. N. M. Beeler, 2002, 32 Rock failure and earthquakes:

International Handbook of Earthquake and Engineering Seismology, v. 81, no. Part A, p. 505–537.

Lowe, D. G., 2004, Distinctive Image Features from Scale-Invariant Keypoints: International Journal of Computer Vision, v. 60, no. 2, p. 91–110, doi:10.1023/B:VISI.0000029664.99615.94.

Maffucci, R., S. Bigi, S. Corrado, A. Chiodi, L. Di Paolo, G. Giordano, and C. Invernizzi, 2015, Quality assessment of reservoirs by means of outcrop data and "discrete fracture network" models: The case history of Rosario de La Frontera (NW Argentina) geothermal system: Tectonophysics, v. 647-648, p. 112–131, doi:10.1016/j.tecto.2015.02.016.

Malinverno, A., and W. B. F. Ryan, 1986, Extension in the Tyrrhenian Sea and shortening in the Apennines as result of arc migration driven by sinking of the lithosphere: Tectonics, v. 5, no. 2, p. 227–245, doi:10.1029/TC005i002p00227.

Marone, C., 1998, The effect of loading rate on static friction and the rate of fault healing during the earthquake cycle: Nature, p. 69–72.

Marshak, S., P. A. Geiser, W. Alvarez, and T. Engelder, 1982, Mesoscopic fault array of the northern Umbrian Apennine fold belt, Italy: Geometry of conjugate shear by pressure-solution slip: Geological Society of America Bulletin, v. 93, no. 10, p. 1013–1022, doi:10.1130/0016-7606(1982)93.

Massoli, D., H. A. Koyi, and M. R. Barchi, 2006, Structural evolution of a fold and thrust belt generated by multiple décollements: analogue models and natural examples from the Northern Apennines (Italy): Journal of Structural Geology, v. 28, no. 2, p. 185–199, doi:10.1016/j.jsg.2005.11.002.

Mazzoli, S., M. D'Errico, L. Aldega, S. Corrado, C. Invernizzi, P. Shiner, and M. Zattin, 2008, Tectonic burial and "young" (<10 Ma) exhumation in the southern Apennines fold-and-thrust belt (Italy): Geology, v. 36, no. 3, p. 243, doi:10.1130/G24344A.1.

McCaffrey, K. J. W., R. R. Jones, R. E. Holdsworth, R. W. Wilson, P. Clegg, J. Imber, N. Holliman, and I. Trinks, 2005, Unlocking the spatial dimension: digital technologies and the future of geoscience fieldwork: Journal of the Geological Society, v. 162, no. 6, p. 927–938, doi:10.1144/0016-764905-017.

Minisini, D., M. Wang, S. Bergman, and C. Aiken, 2014, Geological data extraction from lidar 3-D photorealistic models: A case study in an organic-rich mudstone, Eagle Ford Formation, Texas: Geosphere, p. GES00937.1–, doi:10.1130/GES00937.1.

Moreels, P., and P. Perona, 2006, Evaluation of Features Detectors and

Descriptors based on 3D Objects: International Journal of Computer Vision, v. 73, no. 3, p. 263–284, doi:10.1007/s11263-006-9967-1.

Mostardini, F., and S. Merlini, 1986, Appennino centro meridionale: sezioni geologiche e proposta di modello strutturale: Memorie della Società Geologica Italiana, v. 35, p. 177–202.

Narr, W., and J. Suppe, 1991, Joint spacing in sedimentary rocks: Journal of Structural Geology, v. 13, no. 9, p. 1037–1048, doi:10.1016/0191-8141(91)90055-N.

Neitzel, F., and J. Klonowski, 2011, Mobile 3D mapping with a low-cost UAV system: International Archives of the Photogrammetry, Remote Sensing and Spatial Information Sciences, v. 38, p. 1–6.

Odonne, F., C. Lézin, G. Massonnat, and G. Escadeillas, 2007, The relationship between joint aperture, spacing distribution, vertical dimension and carbonate stratification: An example from the Kimmeridgian limestones of Pointe-du-Chay (France): Journal of Structural Geology, v. 29, no. 5, p. 746–758, doi:10.1016/j.jsg.2006.12.005.

Olson, J. E., 2003, Sublinear scaling of fracture aperture versus length: An exception or the rule? Journal of Geophysical Research, v. 108, no. B9, p. 2413, doi:10.1029/2001JB000419.

Pollard, D. D., and A. Aydin, 1988, Progress in understanding jointing over the past century: Geological Society of America Bulletin, v. 100, no. 8, p. 1181–1204, doi:10.1130/0016-7606(1988)100<1181:PIUJOT>2.3.CO;2.

Power, W. L., and T. E. Tullis, 1991, Euclidean and fractal models for the description of rock surface roughness: Journal of Geophysical Research, v. 96, no. B1, p. 415, doi:10.1029/90JB02107.

Power, W. L., T. E. Tullis, S. R. Brown, G. N. Boitnott, and C. H. Scholz, 1987, Roughness of natural fault surfaces: Geophysical Research Letters, v. 14, no. 1, p. 29–32, doi:10.1029/GL014i001p00029.

Pringle, J. K., J. D. Clark, A. R. Westerman, D. A. Stanbrook, A. R. Gardiner, and B. E. F. Morgan, 2001, Virtual outcrops: 3-D reservoir analogues, *in* L. Ailleres, and T. Rawling, eds., Animations in Geology. Journal of the Virtual Explorer, 4: p. 51–55, doi:10.3809/jvirtex.2001.00036.

Ragan, D. M., 2009, Structural Geology: An Introduction to Geometrical Techniques, Fourth Edition: New York, Cambridge University Press, 602 p.

Ramsay, J. G., 1967, Folding and Fracturing of Rock: New York, McGraw-Hill, Incorporated, 568 p.

Ramsay, J. G., and M. I. Huber, 1987, The techniques of modern structural geology: Folds and fractures: Academic press.

Renard, F., T. Candela, and E. Bouchaud, 2013, Constant dimensionality of fault roughness from the scale of micro-fractures to the scale of continents: Geophysical Research Letters, v. 40, no. 1, p. 83–87, doi:10.1029/2012GL054143.

Renard, F., K. Mair, and O. Gundersen, 2012, Surface roughness evolution on experimentally simulated faults: Journal of Structural Geology, v. 45, p. 101–112, doi:10.1016/j.jsg.2012.03.009.

Renard, F., C. Voisin, D. Marsan, and J. Schmittbuhl, 2006, High resolution 3D laser scanner measurements of a strike-slip fault quantify its morphological anisotropy at all scales: Geophysical Research Letters, v. 33, no. 4, p. L04305, doi:10.1029/2005GL025038.

Rustichelli, A., F. Agosta, E. Tondi, and V. Spina, 2013, Spacing and distribution of bed-perpendicular joints throughout layered, shallow-marine carbonates (Granada Basin, southern Spain): Tectonophysics, v. 582, p. 188–204, doi:10.1016/j.tecto.2012.10.007.

Sagy, A., E. E. Brodsky, and G. J. Axen, 2007, Evolution of fault-surface roughness with slip: Geology, v. 35, no. 3, p. 283, doi:10.1130/G23235A.1.

Sapozhnikov, V., and E. Foufoula-Georgiou, 1995, Study of self-similar and self-affine objects using logarithmic correlation integral: Journal of Physics A: Mathematical and General, v. 28, no. 3, p. 559–571, doi:10.1088/0305-4470/28/3/012.

Scholz, C. H., 2002, The Mechanics of Earthquakes and Faulting (Second edition): Cambridge University Press, 471 p.

Schultz, R. A., C. Klimczak, H. Fossen, J. E. Olson, U. Exner, D. M. Reeves, and R. Soliva, 2013, Statistical tests of scaling relationships for geologic structures: Journal of Structural Geology, v. 48, p. 85–94, doi:10.1016/j.jsg.2012.12.005.

Schultz, R. A., R. Soliva, H. Fossen, C. H. Okubo, and D. M. Reeves, 2008, Dependence of displacement–length scaling relations for fractures and deformation bands on the volumetric changes across them: Journal of Structural Geology, v. 30, no. 11, p. 1405–1411, doi:10.1016/j.jsg.2008.08.001.

Schuster, A., 1898, On the investigation of hidden periodicities with application to a supposed 26 day period of meteorological phenomena: Journal of Geophysical Research, v. 3, no. 1, p. 13, doi:10.1029/TM003i001p00013.

Siman-Tov, S., E. Aharonov, A. Sagy, and S. Emmanuel, 2013, Nanograins form carbonate fault mirrors: Geology, v. 41, no. 6, p. 703–706, doi:10.1130/G34087.1.

Snavely, N., S. M. Seitz, and R. Szeliski, 2008, Modeling the world from Internet photo collections: International Journal of Computer Vision, v. 80, no. 2, p. 189–210, doi:10.1007/s11263-007-0107-3.

Snavely, N., S. M. Seitz, and R. Szeliski, 2006, Photo tourism: p. 835, doi:10.1145/1141911.1141964.

Sturzenegger, M., and D. Stead, 2009, Quantifying discontinuity orientation and persistence on high mountain rock slopes and large landslides using terrestrial remote sensing techniques: Natural Hazards and Earth System Science, v. 9, no. 2.

Tavani, S., P. Arbues, M. Snidero, N. Carrera, and J. A. Muñoz, 2011, Open Plot Project: an open-source toolkit for 3-D structural data analysis: Solid Earth, v. 2, no. 1, p. 53–63, doi:10.5194/se-2-53-2011.

Tavani, S., P. Granado, A. Corradetti, M. Girundo, A. Iannace, P. Arbués, J. A. Muñoz, and S. Mazzoli, 2014, Building a virtual outcrop, extracting geological information from it, and sharing the results in Google Earth via OpenPlot and Photoscan: An example from the Khaviz Anticline (Iran): Computers & Geosciences, v. 63, p. 44–53, doi:10.1016/j.cageo.2013.10.013.

Tavani, S., F. Storti, J. Bausà, and J. A. Muñoz, 2012, Late thrusting extensional collapse at the mountain front of the northern Apennines (Italy): Tectonics, v. 31, no. 4, p. 1–17, doi:10.1029/2011TC003059.

Tavani, S., F. Storti, O. Lacombe, A. Corradetti, J. A. Muñoz, and S. Mazzoli, 2015, A review of deformation pattern templates in foreland basin systems and fold-and-thrust belts: Implications for the state of stress in the frontal regions of thrust wedges: Earth-Science Reviews, v. 141, p. 82–104, doi:10.1016/j.earscirev.2014.11.013.

Tavani, S., F. Storti, and J. A. Muñoz, 2010, Scaling relationships between stratabound pressure solution cleavage spacing and layer thickness in a folded carbonate multilayer of the Northern Apennines (Italy): Journal of Structural Geology, v. 32, no. 3, p. 278–287, doi:10.1016/j.jsg.2009.12.004.

Tavani, S., G. Vignaroli, and M. Parente, 2015, Transverse versus longitudinal extension in the foredeep-peripheral bulge system: Role of Cretaceous structural inheritances during early Miocene extensional faulting in inner central Apennines belt: Tectonics, v. 34, no. 7, p. 1412–1430, doi:10.1002/2015TC003836.

Tondi, E., M. Antonellini, A. Aydin, L. Marchegiani, and G. Cello, 2006, The role of deformation bands, stylolites and sheared stylolites in fault development in carbonate grainstones of Majella Mountain, Italy: Journal of Structural Geology, v. 28, no. 3, p. 376–391, doi:10.1016/j.jsg.2005.12.001.

Tondi, E., A. Cilona, F. Agosta, A. Aydin, A. Rustichelli, P. Renda, and G. Giunta, 2012, Growth processes, dimensional parameters and scaling relationships of two conjugate sets of compactive shear bands in porous carbonate grainstones, Favignana Island, Italy: Journal of Structural Geology, v. 37, p. 53–64, doi:10.1016/j.jsg.2012.02.003.

Torres, J. C., G. Arroyo, C. Romo, and J. De Haro, 2012, 3D Digitization using Structure from Motion, *in* I. Navazo, and G. Patow, eds., CEIG - Spanish Computer Graphics Conference: The Eurographics Association 2012.

Trinks, I., P. Clegg, K. J. W. McCaffrey, R. Jones, R. Hobbs, B. Holdsworth, N. Holliman, J. Imber, S. Waggott, and R. Wilson, 2005, Mapping and analysing virtual outcrops: Visual Geosciences, v. 10, no. 1, p. 13–19, doi:10.1007/s10069-005-0026-9.

Ullman, S., 1979, The interpretation of structure from motion: Proceedings of the Royal Society of London. Series B Biological Sciences, v. 203, no. 1153, p. 405–426, doi:10.1098/rspb.1979.0006.

Vaughan, R. L., S. A. Khan, L. J. Weber, O. Suwaina, A. Al-Mansoori, A. Ghani, C. J. Strohmenger, M. A. Herrmann, and D. Hulstrand, 2004, Integrated Characterization of UAE Outcrops: From Rocks to Fluid Flow Simulation, *in* Abu Dhabi International Conference and Exhibition: Society of Petroleum Engineers, doi:10.2118/88730-MS.

Verhoeven, G., 2011, Taking computer vision aloft - archaeological three-dimensional reconstructions from aerial photographs with photoscan: Archaeological Prospection, v. 18, no. 1, p. 67–73, doi:10.1002/arp.399.

Verwer, K., 2008, Spatial models of carbonate platform anatomy: Amsterdam, The Netherlands, Vrrije Universiteit, 244 p.

Vitale, S., and S. Ciarcia, 2013, Tectono-stratigraphic and kinematic evolution of the southern Apennines/Calabria–Peloritani Terrane system (Italy): Tectonophysics, v. 583, p. 164–182, doi:10.1016/j.tecto.2012.11.004.

Watanabe, K., and H. Takahashi, 1995, Fractal geometry characterization of geothermal reservoir fracture networks: Journal of Geophysical Research, v. 100, no. B1, p. 521, doi:10.1029/94JB02167.

Wennberg, O. P., T. Svånå, M. Azizzadeh, A. M. M. Aqrawi, P. Brockbank, K. B. Lyslo, and S. Ogilvie, 2006, Fracture intensity vs. mechanical stratigraphy in platform top carbonates: the Aquitanian of the Asmari

Formation, Khaviz Anticline, Zagros, SW Iran: Petroleum Geoscience, v. 12, no. 3, p. 235–246, doi:10.1144/1354-079305-675.

Whitaker, A. E., and T. Engelder, 2005, Characterizing stress fields in the upper crust using joint orientation distributions: Journal of Structural Geology, v. 27, no. 10, p. 1778–1787, doi:10.1016/j.jsg.2005.05.016.

Woodcock, N. H., 1976, The Accuracy of Structural Field Measurements: The Journal of Geology, v. 84, no. 3, p. 350–355.

Wu, H., and D. D. Pollard, 1995, An experimental study of the relationship between joint spacing and layer thickness: Journal of Structural Geology, v. 17, no. 6, p. 887–905, doi:10.1016/0191-8141(94)00099-L.

Xu, X., C. L. V. Aiken, J. P. Bhattacharya, R. M. Corbeanu, K. C. Nielsen, G. A. McMechan, and M. G. Abdelsalam, 2000, Creating virtual 3-D outcrop: The Leading Edge, v. 19, no. 2, p. 197–202, doi:10.1190/1.1438576.

Xu, X., C. L. V. Aiken, and K. C. Nielsen, 1999, Real time and the virtual outcrop improve geological field mapping: Eos, Transactions American Geophysical Union, v. 80, no. 29, p. 317, doi:10.1029/99EO00232.